



Kent Academic Repository

Moss, Rob M. (2009) *Structural studies of metal doped phosphate glasses and computational developments in diffraction analysis*. Doctor of Philosophy (PhD) thesis, University of Kent.

Downloaded from

<https://kar.kent.ac.uk/38807/> The University of Kent's Academic Repository KAR

The version of record is available from

This document version

Author's Accepted Manuscript

DOI for this version

Licence for this version

UNSPECIFIED

Additional information

Versions of research works

Versions of Record

If this version is the version of record, it is the same as the published version available on the publisher's web site. Cite as the published version.

Author Accepted Manuscripts

If this document is identified as the Author Accepted Manuscript it is the version after peer review but before type setting, copy editing or publisher branding. Cite as Surname, Initial. (Year) 'Title of article'. To be published in *Title of Journal*, Volume and issue numbers [peer-reviewed accepted version]. Available at: DOI or URL (Accessed: date).

Enquiries

If you have questions about this document contact ResearchSupport@kent.ac.uk. Please include the URL of the record in KAR. If you believe that your, or a third party's rights have been compromised through this document please see our [Take Down policy](https://www.kent.ac.uk/guides/kar-the-kent-academic-repository#policies) (available from <https://www.kent.ac.uk/guides/kar-the-kent-academic-repository#policies>).

**Structural studies of metal doped phosphate
glasses and computational developments in
diffraction analysis**

Robert M. Moss

September 2009

A THESIS SUBMITTED TO THE UNIVERSITY OF KENT IN THE SUBJECT OF
PHYSICS FOR THE DEGREE OF DOCTOR OF PHILOSOPHY

University of
Kent

For Planet Rock

<http://www.planetrock.com>

“When all is said and done, more is said than done.”

Lou Holtz

Abstract

The thesis focuses on the analysis and determination of the structure of various metal doped phosphate glasses, which are of interest for their potential biomedical properties. The structures have been determined principally by X-ray and neutron diffraction but are also supported by complimentary X-ray absorption spectroscopy measurements and computational modelling. Such studies contribute to about half of the work presented in this thesis.

Among the glasses of interest are silver-doped calcium sodium phosphates, which exhibit antimicrobial properties when the Ag^+ ions are released over time in an aqueous environment. The advanced probe technique of neutron diffraction with isotropic substitution (NDIS) has been applied to elucidate the structural role of silver in these glasses. The results revealed that silver occupies a highly distorted octahedral environment analogous to that in crystalline Ag_2SO_4 .

Another glass study herein is associated with zinc titanium calcium sodium phosphate, which is biomedically interesting since the release of Zn^{2+} ions is shown to enhance cell attachment and proliferation. Structural analysis of multi-component glasses such as these tends to be difficult, but diffraction techniques and X-ray absorption spectroscopy have been used together to reveal the cation first neighbour coordination environments.

The other significant element of the work presented here has been the development of data analysis techniques, with the emphasis on the creation of a program, which allows co-fitting of X-ray and neutron diffraction data of amorphous (and potentially crystalline) data. The code is written in *MATLAB* and makes use of the Nelder-Mead simplex method to minimise a set of “best guess” structural parameters supplied by the user. Extrema bound constraints are implemented by means of a sinusoidal parameter transform. Ultimately, the code is to be compiled and made available to users *via* the ISIS Pulsed Neutron Facility, UK.

Acknowledgements

I would like to thank all those who have contributed to this thesis both directly and indirectly, especially **Bob Newport** and **Alex Hannon** who have been excellent supervisors.

I am deeply thankful to **Dave Pickup** who is a patient teacher and a great friend. I would also like to thank **Kate Wetherall** for helping me out with some of the structural specifics (including teaching me RMC) and for always pointing out where I'm going wrong. I am supremely grateful for the lengthy debates I have had with **Richard Haworth** and **Dong Qiu** which have helped me along on my PhD journey.

A big thank you to **Jonathan Knowles**, **Ifty Ahmed**, **Sabeel Valappil** and **Ensanya Abou Neel**, who provided the samples analysed in this study. Further thanks go to **Mark Smith**, **Julian Jones** and anyone else involved in the sol-gel partnership meetings for listening to my problems and for their helpful discussions.

I would also like to thank the whole *MATLAB* user community for their limitless ideas and in particular **John D'Errico** for his *MATLAB* routine *fminsearchcon*, which forms the basis of *NXFit* and without which the implementation of bound constraints would have been beyond my programming ability.

The following people (in no particular order) have contributed by helping out on experiments or by encouraging me to engage my brain (whether they know it or not): **Gavin Mountjoy**, **Alan Chadwick**, **Helen Twyman**, **Vicky Fitzgerald**, **Jodie Smith**, **Richard Martin**, **Mike Henson**, **Paul Bingham** and **Emma Barney**.

On a personal level I would like to thank all of my family for their support; principally my dearest fiancée **Kate** and my parents **Jan** and **Steve**.

Funding for this project was provided by EPSRC through the School of Physical Sciences (University of Kent) DTA and the STFC (CMPC06103).

Contents

Abstract	i
Acknowledgements.....	ii
Contents	iii
Published Work	vi
Glossary of Abbreviations.....	ix
List of Tables.....	x
List of Figures.....	xii
Chapter 1 – Introduction	1
1.1 A short history of phosphate glasses.....	1
1.2 The fundamental glass formers.....	2
1.3 Network modifiers	5
1.4 Network intermediates	5
1.5 Other structural theories	5
1.6 Ranges of order in an amorphous solid.....	6
1.7 The structure of phosphate glasses.....	7
1.8 Biomaterials.....	12
1.9 Summary.....	14
1.10 References.....	15
Chapter 2 – Theory	18
2.1 Introduction.....	18
2.2 The scattering cross-section.....	18
2.3 Scattering in general.....	19
2.4 Scattering by a group of atoms	20
2.5 Scattering by an isotropic sample	21
2.6 Radial distribution functions.....	22
2.7 Experimental real space correlation functions.....	24
2.8 Application to neutron diffraction.....	25
2.9 The modification function	27
2.10 Special case – NDIS.....	29
2.11 Application to X-ray diffraction	30
2.12 X-ray absorption spectroscopy	32

2.13 References.....	36
Chapter 3 – Experimental.....	37
3.1 Introduction.....	37
3.2 Production of neutrons at the ISIS pulsed neutron source	37
3.3 Processing experimental neutron diffraction data.....	39
3.4 Production of X-rays at the Synchrotron Radiation Source	44
3.5 Processing of experimental X-ray diffraction data	46
3.6 Analysis of diffraction data	52
3.7 Processing of experimental X-ray absorption spectroscopy data	55
3.8 Analysis of EXAFS data	59
3.9 References	62
Chapter 4 – Computational Developments: <i>NXFit</i>	64
4.1 Introduction.....	64
4.2 Technical	65
4.3 Preparing to run <i>NXFit</i>	68
4.4 Running <i>NXFit</i>	71
4.5 Future improvements.....	74
4.6 References	78
Chapter 5 – Calcium Sodium Phosphate: Total Diffraction & RMC.....	79
5.1 Introduction.....	79
5.2 Experimental.....	79
5.3 Results	80
5.4 Discussion.....	86
5.5 Conclusions.....	89
5.6 References	90
Chapter 6 – Silver Calcium Sodium Phosphate I: NDIS	91
6.1 Introduction.....	91
6.2 Characterisation of the local silver environment	92
6.3 Experimental.....	93
6.4 Results	95
6.5 Discussion.....	98
6.6 Conclusions.....	101
6.7 References	102
Chapter 7 – Silver Calcium Sodium Phosphate II: Total Diffraction & RMC	103

7.1 Introduction.....	103
7.2 Experimental.....	103
7.3 Results	104
7.4 Discussion.....	110
7.5 Conclusions.....	114
7.6 References	115
Chapter 8 – Zinc Titanium Calcium Sodium Phosphate: Total Diffraction & XAS..	116
8.1 Introduction.....	116
8.2 Experimental.....	117
8.3 Results	118
8.4 Discussion.....	123
8.5 Conclusions.....	128
8.6 References	129
Chapter 9 – Summary	131
9.1 Further Work.....	131
9.2 Conclusions.....	132
Appendix A – <i>MATLAB</i> Code: <i>NXFit_v4</i>	135

Published Work

Here follows a list of conference posters, presentations and published papers that have resulted from the work conducted as part of this project.

Poster presentations

Structural characteristics of antibacterial bioresorbable phosphate glass. *Society of Glass Technology Annual Conference*, Derby, 2007.

Oral Presentations

The effect of Zn and Ti on the structure of bioresorbable calcium-sodium phosphate based glass. *International Conference on the Physics of Non-Crystalline Solids (PNCS XII)*, Foz do Iguaçu, Brazil, 2009.

Structural characteristics of antibacterial bioresorbable phosphate glass. *Disordered Crystals Meeting*, The Cosener's House, Didcott, 2008.

X-ray and neutron diffraction in symbiosis: getting the most out of experimental data. *Society of Glass Technology Annual Conference*, Cambridge, 2008. Paul Award winner for best presentation in the New Researchers Forum.

Publications

The effect of zinc and titanium on the structure of calcium-sodium phosphate based glass. R. M. Moss, E. A. Abou Neel, D. M. Pickup, H. L. Twyman, R. A. Martin, M. D. Henson, E. R. Barney, A. C. Hannon, J. C. Knowles and R. J. Newport, *Journal of Non-Crystalline Solids* (2009), submitted.

Bioactive glass sol-gel foam scaffolds: Evolution of nanoporosity during processing and in situ monitoring of apatite layer formation using small- and wide-angle X-ray scattering. V. FitzGerald, R. A. Martin, J. R. Jones, D. Qiu, K. M. Wetherall, R. M. Moss and R. J. Newport, *Journal of Biomedical Materials Research Part A* **91A** (2009), p. 76.

An atomic scale comparison of the reaction of Bioglass[®] in two types of simulated body fluid. V. FitzGerald, D. M. Pickup, D. Greenspan, K. M. Wetherall, R. M. Moss, J. R. Jones and R. J. Newport, *Physics and Chemistry of Glasses-European Journal of Glass Science and Technology Part B* **50** (2009), p. 137.

Structural characterization by X-ray methods of novel antimicrobial gallium-doped phosphate-based glasses. D. M. Pickup, R. M. Moss, D. Qiu, R. J. Newport, S. P. Valappil, J. C. Knowles and M. E. Smith, *Journal of Chemical Physics* **130** (2009).

Preparation, structural characterisation and antibacterial properties of Ga-doped sol-gel phosphate-based glass. D. M. Pickup, S. P. Valappil, R. M. Moss, H. L. Twyman, P. Guerry, M. E. Smith, M. Wilson, J. C. Knowles and R. J. Newport, *Journal of Materials Science* **44** (2009), p. 1858.

Structural characteristics of antibacterial bioresorbable phosphate glass. R. M. Moss, D. M. Pickup, I. Ahmed, J. C. Knowles, M. E. Smith and R. J. Newport, *Advanced Functional Materials* **18** (2008), p. 634.

An X-ray absorption spectroscopy study of the local environment of iron in degradable iron-phosphate glasses. D. Qiu, R. M. Moss, D. M. Pickup, I. Ahmed, J. C. Knowles and R. J. Newport, *Journal of Non-Crystalline Solids* **354** (2008), p. 5542.

Sulfur and iron speciation in recently recovered timbers of the Mary Rose revealed via X-ray absorption spectroscopy. K. M. Wetherall, R. M. Moss, A. M. Jones, A. D. Smith, T. Skinner, D. M. Pickup, S. W. Goatham, A. V. Chadwick and R. J. Newport, *Journal of Archaeological Science* **35** (2008), p. 1317.

Ti K-edge XANES study of the local environment of titanium in bioresorbable TiO₂-CaO-Na₂O-P₂O₅ glasses. D. M. Pickup, E. A. Abou Neel, R. M. Moss, K. M. Wetherall, P. Guerry, M. E. Smith, J. C. Knowles and R. J. Newport, *Journal of Materials Science-Materials in Medicine* **19** (2008), p. 1681.

New sol-gel synthesis of a $(\text{CaO})_{0.3}(\text{Na}_2\text{O})_{0.2}(\text{P}_2\text{O}_5)_{0.5}$ bioresorbable glass and its structural characterisation. D. M. Pickup, P. Guerry, R. M. Moss, J. C. Knowles, M. E. Smith and R. J. Newport, *Journal of Materials Chemistry* **17** (2007), p. 4777.

A neutron and X-ray diffraction study of bioglass with reverse Monte Carlo modelling. V. FitzGerald, D. M. Pickup, D. Greenspan, G. Sarkar, J. J. Fitzgerald, K. M. Wetherall, R. M. Moss, J. R. Jones and R. J. Newport, *Advanced Functional Materials* **17** (2007), p. 3746.

X-ray absorption spectroscopy and high-energy XRD study of the local environment of copper in antibacterial copper-releasing degradable phosphate glasses. D. M. Pickup, I. Ahmed, V. FitzGerald, R. M. Moss, K. M. Wetherall, J. C. Knowles, M. E. Smith and R. J. Newport, *Journal of Non-Crystalline Solids* **352** (2006), p. 3080.

Glossary of Abbreviations

BO	Bridging Oxygen
CRN	Continuous Random Network
EPSR	Empirical Potential Structure Refinement
EXAFS	Extended X-ray Absorption Fine Structure
FI	Fit Index
FT	Fourier Transform
GEM	General Materials Diffractometer
GUI	Graphical User Interface
ICP	Inductively Coupled Plasma
ID	Insertion Device
MCR	<i>MATLAB</i> Compiler Runtime
MD	Molecular Dynamics
MRN	Modified Random Network
NBO	Non-Bridging Oxygen
NDIS	Neutron Diffraction with Isotopic Substitution
NMR	Nuclear Magnetic Resonance
OES	Optical Emission Spectroscopy
PVP	Polyvinylpyrrolidone
RMC	Reverse Monte Carlo
SRS	Synchrotron Radiation Source
TOF	Time-of-Flight
XANES	X-ray Absorption Near-Edge Structure
XAS	X-ray Absorption Spectroscopy

List of Tables

Table 1.1: Phosphate classification based on the ratio of oxygen to phosphorus atoms in a sample.....	7
Table 5.1: Minimum interatomic separation for each atom pair in the RMC model. .	81
Table 5.2: Structural parameters derived from the RMC model. N_{ij} values shown in parentheses are the coordination numbers given in the opposite sense (<i>i.e.</i> N_{ji}).....	84
Table 5.3: Optimised structural parameters output by <i>NXFit</i> upon co-fitting X-ray and neutron diffraction data of $(P_2O_5)_{50}(CaO)_{30}(Na_2O)_{20}$	85
Table 5.4: P-NBO and P-BO structural parameters derived from fitting $T^N(r)$	87
Table 6.1: Sample characterisation of melt-quench prepared $^{107/109}Ag$ doped phosphate glasses.	94
Table 6.2: Ag- j correlations determined by fitting $T_{Ag-j}(r)$. Atom pairs separated by ... are considered to be in the second coordination sphere.....	96
Table 6.3: Structural parameters obtained by fitting $T(r)$. The Ag- j correlations were fixed with the values shown in Table 6.2.....	97
Table 6.4: P-NBO and P-BO bond length variation for different Q^n speciation and cations modifiers in crystalline and amorphous samples. Parameters taken from ^a [5], ^b [12] and ^c [13].	100
Table 7.1: Compositions and measured densities for $(P_2O_5)_{50}(CaO)_{30}(Na_2O)_{20-x}(Ag_2O)_x$ samples.....	103
Table 7.2: Structural parameters derived from the RMC models. N_{ij} values shown in parentheses are the coordination numbers given in the opposite sense (<i>i.e.</i> N_{ji}).....	106
Table 7.3: Optimised structural parameters output by <i>NXFit</i> upon co-fitting X-ray and neutron diffraction data of $(P_2O_5)_{50}(CaO)_{30}(Na_2O)_{20-x}(Ag_2O)_x$	109
Table 7.4: P-NBO and P-BO structural parameters derived from fitting $T^N(r)$	113
Table 8.1: Sample characterisation for glasses of general composition $(P_2O_5)_{50}(CaO)_{30-x}(Na_2O)_{20}(TiO_2)_5(ZnO)_x$	117
Table 8.2: Structural parameters obtained by fitting the Zn K-edge EXAFS spectra. The second nearest neighbour parameters could not be determined for sample T5Z1 owing to the exceptionally low concentration of zinc atoms. The numbers given in parentheses are the uncertainty in the final decimal place.....	120

Table 8.3: Optimised structural parameters output by <i>NXFit</i> upon co-fitting X-ray and neutron diffraction data. Parameters have been rounded to a suitable number of decimal places.	123
Table 8.4: Optimised parameters determined by fitting the P-NBO and P-BO contributions to the first peak in $T^N(r)$	125
Table 8.5: Cation valence neutralised in each MO_x polyhedra.	126
Table 8.6: Results for the conversion of N_{M-O} to N_{O-M} for each type of metal (M) in sample T5Z5.	127

List of Figures

Figure 1.1: 2D comparison between a crystalline (left) and amorphous (right) structure [12].	3
Figure 1.2: The bonding angles between two SiO_4^{4-} structural units [14].	4
Figure 1.3: Q^n groups for phosphate tetrahedra from Brow [26].	8
Figure 1.4: Lengths and magnitudes of the P-O correlations as a function of the molar ratio, $y = 1.94 (Q^1)$, $1.56 (Q^1/Q^2)$, $1.00 (Q^2)$, $0.61 (Q^2/Q^3)$ and vitreous $\text{P}_2\text{O}_5 (Q^3)$. From Hoppe <i>et al.</i> [29].	9
Figure 1.5: P-O bond length distribution for metaphosphate glasses with different modifying cations. From Hoppe <i>et al.</i> [29].	10
Figure 1.6: A small section of the structural model produced by Wetherall <i>et al.</i> [33] showing phosphorus (pink) and oxygen (red) atoms forming tetrahedral chains and calcium (green) atoms coordinating with the NBOs.	12
Figure 2.1: Geometrical representation of a diffraction experiment. Note that $dS = r^2 d\Omega$ and k represents the direction of the incident beam of probes [1].	19
Figure 2.2: Scattering of a probe by sample through and angle 2θ .	20
Figure 2.3: Variation in $P_{ij}^N(r)$ using step (bottom), Hanning (middle) and Lorch (top) modification functions.	28
Figure 2.4: Graphical representation of $M(Q)$ over the range $0 \leq Q \leq 20 \text{ \AA}^{-1}$, with Hanning (blue), Lorch (red) and step function (green).	29
Figure 2.5: XAS spectrum indicating the XANES and EXAFS regions.	32
Figure 2.6: Absorption cross-section as a function of photon energy for isolated tin atom. The L_3 , L_2 and L_1 edges are at 3.93, 4.16 and 4.46 keV respectively. The K-edge is at 29.20 keV.	34
Figure 3.1: Simulated, post-moderated neutron flux.	38
Figure 3.2: 3D representation of GEM showing the large detector array and the sample loading position in the top of the sample tank.	39
Figure 3.3: Neutron differential scattering cross-section (black) from GEM detector bank 5 and $I_S(Q)$ (red).	43
Figure 3.4: Unscaled $d\sigma/d\Omega$ for GEM detector banks 0 through 7 (top to bottom).	44
Figure 3.5: Comparison of a bending magnet and wiggler wavelength spectrum [9].	45

Figure 3.6: Schematic diagram of experimental set-up at SRS station 9.1 in theta-two theta geometry.	46
Figure 3.7: $I_{Comp}(Q)$ (green), $I_{Self}(Q)$ (blue). The experimental diffraction data (black), $I_v(Q)I_{abs}(Q)$, has been scaled, by adjusting S , to oscillate about the sum $I_{Comp}(Q)+I_{Self}(Q)$ (red). In this case A has been set to unity.	51
Figure 3.8: $i(Q)/f_e^2(Q)$ a) showing the drop-off at high Q and b) after polynomial correction.....	52
Figure 3.9: Schematic diagram of the XAS experimental set-up in transmission mode.	56
Figure 3.10: Efficiency of a 10 cm long gas ionisation chamber as a function of energy for different gasses at normal pressure [18].....	56
Figure 4.1: Graphical representation of the sinusoidal parameter transform. Here three distinct values of $z(i)$ are highlighted, each giving the same real parameter, $y(i)$	68
Figure 4.2: Example input data file.	69
Figure 4.3: Example neutron sample composition file.	69
Figure 4.4: Example X-ray sample composition file.....	70
Figure 4.5: Example input parameter file.	70
Figure 4.6: Example bound constrains file.	71
Figure 4.7: Initial view of the main <i>NXFit</i> GUI.	71
Figure 4.8: <i>NXFit</i> GUI with all fields filled out. Plots on the right show the experimental data (blue) and the simulated fit (red) and is updated in real-time.....	73
Figure 4.9: The individual partial correlations functions (green) are shown along with the fit (red), the data (blue) and the residual (black dashed).....	74
Figure 4.10: An example of $T(r)$ for X-ray (black) and neutron (red) data.	77
Figure 5.1: X-ray (top) and neutron (bottom) $i(Q)$ (black) and RMC model (red) for $(P_2O_5)_{50}(CaO)_{30}(Na_2O)_{20}$	82
Figure 5.2: $g_{PP}(r)$ (black) and $C_{PP}(r)$ (red) showing a clear plateau in $C_{PP}(r)$ at 3.30 Å, which defines the upper boundary of the first P-P coordination shell.....	83
Figure 5.3: $T(r)$ produced by X-ray (top) and neutron (bottom) diffraction for $(P_2O_5)_{50}(CaO)_{30}(Na_2O)_{20}$	84
Figure 5.4: Fit (red dashed) to X-ray (top) and neutron (bottom) $T(r)$ (black) produced by refining the input parameters. Correlations from left to right: P-O (green), Na-O (cyan), Ca-O (magenta), O··O (yellow), P··P (navy), O··O (burgundy) and P··Ca (olive).	86

Figure 5.5: $T^N(r)$ highlighting the split in the P-O peak. The contributions are from P-NBO (left) and P-BO (right).	87
Figure 6.1: Number of viable culture forming units (CFU) present as a function of time for various silver concentrations [1].	92
Figure 6.2: $i^X(Q)$ for ^{107}Ag (top) and ^{109}Ag (bottom) NDIS samples.	94
Figure 6.3: Neutron diffraction $i^N(Q)$ measured for the ^{107}Ag (upper) and ^{109}Ag (lower) doped phosphate glasses. The ^{107}Ag $i^N(Q)$ is off-set for clarity.	95
Figure 6.4: $T_{\text{Ag-}j}(r)$ for the experimentally measured (solid) and the simulated (dashed) functions.	96
Figure 6.5: $T(r)$, with the Ag- j correlations removed (solid) for ^{107}Ag (upper) and ^{109}Ag (lower) doped samples. The real space simulation (dashed) is shown for each sample.	97
Figure 6.6: Ag K-edge XANES for samples of composition $(\text{P}_2\text{O}_5)_{50}(\text{CaO})_{30}(\text{Na}_2\text{O})_{20-x}(\text{Ag}_2\text{O})_x$. The spectrum for Ag_2SO_4 is also shown (dashed) for comparison. Spectra for $x = 5$ and 10 mol% are from [14] and [1] respectively.	99
Figure 7.1: a) X-ray (top) and neutron (bottom) $i(Q)$ (black) with RMC model (red) for sample with $x = 10$ mol% and b) likewise for sample with $x = 20$ mol% Ag_2O	105
Figure 7.2: $g_{\text{NBOCa}}(r)$ for samples with $x = 0$ (bottom), 10 (middle) and 20 (top) mol% Ag_2O . An off-set has been applied for clarity.	107
Figure 7.3: $g_{\text{AgNBO}}(r)$ (black) and $C_{\text{AgNBO}}(r)$ (red) for a) $x = 10$ mol% and b) $x = 20$ mol% Ag_2O . The positions of the three NDIS derived Ag-O correlations are also shown (blue).	108
Figure 7.4: Fits to the experimental data for X-ray (left) and neutron (right) diffraction for samples with $x = 5$ (a,d), 15 (b,e) and 20 (c,f) mol% Ag_2O	110
Figure 7.5: $B(Q)$ for sample with $x = 0$ (bottom) and 20 (top) mol% Ag_2O	111
Figure 7.6: $T^N(r)$ for samples $x = 5$ (bottom), 15 (middle) and 20 (top) mol% Ag_2O highlighting the split in the P-O peak. The contributions are from P-NBO (left) and P-BO (right).	112
Figure 8.1: Zn K-edge XANES spectra. The spectra for ZnO (4-fold), $\text{Zn}(\text{NO}_3)_2$ (6-fold) and $\text{CaZn}_2(\text{PO}_4)_2$ (mixed) are also shown for comparison.	119
Figure 8.2: EXAFS spectrum for sample T5Z5 (solid) and simulation (dashed).	120
Figure 8.3: X-ray ($i^X(Q)$) and neutron ($i^N(Q)$) interference functions for samples T5Z1, T5Z3 and T5Z5 (bottom to top).	121

Figure 8.4: Fit (red dashed) to X-ray (top) and neutron (bottom) $T(r)$ (black) produced by refining the input parameters. Correlations from left to right: P-O (green), Ti-O (blue), Zn-O (cyan), Na-O (magenta), Ca-O (yellow), O··O (olive) and O··O (navy).
 122

Figure 8.5: $T^N(r)$ for samples T5Z1, T5Z3 and T5Z5 (bottom to top) with corresponding fits relating to the P-NBO (left) and P-BO (right) contributions. The data, fits and partials have been off-set for clarity. 124

Chapter 1 – Introduction

This thesis concerns the analysis of the structure of phosphate based glasses, with attention being paid not only to the experimental results, but also to developments in the data analysis process. The materials studied here all result from ongoing research in the field of biomaterials.

This chapter highlights the main concepts in glass formation that underpin the current understanding of glass structure. An outline is given about the history of phosphate glasses after which a more general description is presented on glass network theory and the origin of the structural disorder observed in glassy systems. The discussion then focuses on the structural properties of phosphate glasses. In order to place these materials in a wider context, a short summary is given on biomaterials and how phosphate glasses may be able to replace some of the current biomaterials in various applications.

1.1 A short history of phosphate glasses

Phosphate glasses with relatively high refractive indices (compared to silicate optical glasses) were developed about 100 years ago by Schott and co-workers for optical applications. Interest followed in alkaline earth phosphates due to their high transparency to UV light compared to silicate glasses but low chemical durability discouraged further development into these glasses. A description of these early phosphate glasses can be found in Kreidl and Weyl [1].

In the 1950s interest in amorphous phosphates was renewed due to their versatility in industrial applications, including hard water processing and as clay and pigment manufacturing dispersants [2]. By studying these materials, Van Wazer [2] was able to establish much of what is currently understood about phosphate glasses. Kordes *et al.* [3, 4] noted some anomalous trends when they reviewed alkaline earth phosphates. The anomaly was related to an apparent compositional dependence on the coordination number of the metal cations.

The development of solid state lasers in the 1960s began a new period of development of phosphate glasses. Some rare earth doped phosphates exhibit a large stimulated emission cross-section with low thermo-optical coefficients (compared to their silicate counterparts) and are of particular use in high powered laser applications [5, 6].

More recently, phosphate glasses have been developed for a variety of specialty applications, including hermetic seals [7], organic/inorganic composites [8], nuclear waste hosts [9] and solid state electrolytes [10, 11]. The phosphate glasses studied here were developed as a consequence of ongoing research in the field of biomaterials.

1.2 The fundamental glass formers

The simple oxides of SiO_2 , P_2O_5 , B_2O_3 and GeO_2 are the fundamental glass formers. These are vitrified by heating until a melt is formed which is then super cooled to avoid crystallisation.

In order to describe the structure of these fundamental oxide glasses Zachariasen [12] introduced the continuous random network (CRN) theory. Zachariasen hypothesised that the atoms in a glass are linked together by forces that are essentially the same as those in a corresponding crystals and that if the free energy of the glass is to be comparable to that of the crystal then it is necessary that the oxygen polyhedra in the glass and crystal are similar. For example, in the case of SiO_2 , the basic building block is the SiO_4^{4-} tetrahedron and these units are evident in both the crystalline and vitrified forms.

Zachariasen postulated that these structural units link together to form extended 3D networks where the atoms vibrate about equilibrium positions. The left hand side of Figure 1.1 is a 2D representation showing how the units would fit together in a crystalline sample. The atoms have well defined positions and exhibit complete periodicity, which means that a diffraction experiment yields a complete, quantitative description of the structure in terms of a unit cell. This involves relatively few independent parameters: those to do with the lattice (a , b , c , α , β , γ), those to do with the atomic positions (x_i , y_i , z_i) and a thermal displacement parameter.

The right hand side of Figure 1.1 shows the same 2D building blocks, but this time the structural units are linked together to form a non-periodic structure that lacks long range translational order. This is the definition of an amorphous material [13] of which glass is one type. In order to completely define the structure of an amorphous material it would be necessary to specify positional coordinates and thermal parameters for every atom, which is impossible for any real sample. The lack of a simple structural formalism, such as the unit cell, means that the most that can be obtained from a diffraction experiment on an isotropic amorphous material is a 1D correlation function and it is impossible to uniquely determine the structure in this instance.

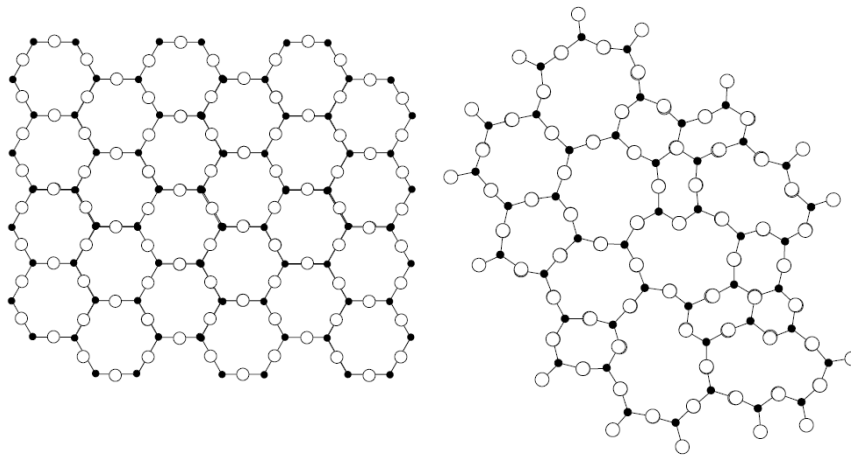


Figure 1.1: 2D comparison between a crystalline (left) and amorphous (right) structure [12].

The origin of the disorder is illustrated in Figure 1.2 using SiO_2 as an example. The intra-tetrahedral Si-O and O-O distances remain fairly constant while the angles α_1 , α_2 and β can vary, leading to significant disparity in the inter-tetrahedral Si-Si distance.

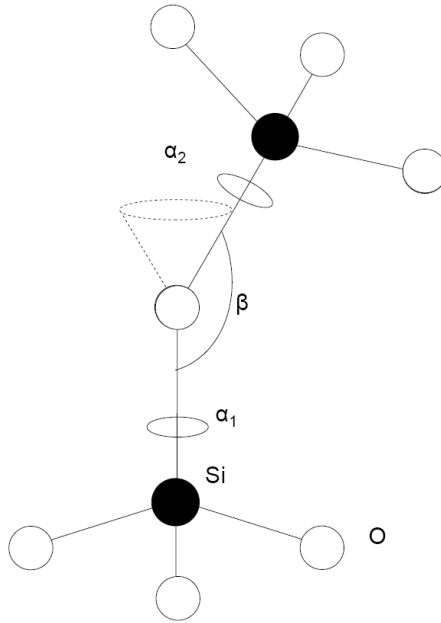


Figure 1.2: The bonding angles between two SiO_4^{4-} structural units [14].

Zachariasen proposed a set of criteria for the formation of a distortion free CRN:

1. An oxygen atom should not be linked to more than two network forming cations.
2. The coordination number of oxygen around the network forming cations should be small (of the order of 3 or 4).
3. Oxygen polyhedra should share corners only and not edges nor faces.
4. In a 3D network, at least three corners of each polyhedron should be shared.

Violation of one of these criteria does not mean that a glass cannot be formed, just that it is energetically less favourable to one where all the criteria are met [14].

In addition to SiO_2 , P_2O_5 , B_2O_3 and GeO_2 there are a number of other oxides that are capable of forming glasses under certain conditions: Bi_2O_3 , As_2O_3 , Sb_2O_3 , TeO_2 , Al_2O_3 , Ga_2O_3 and V_2O_5 . These additional oxides do not readily form glasses by themselves unless rapidly quenched or created by vapour deposition [15]. It should be noted that it is not only oxides that are capable of forming glasses. Notable examples of alternatives are chalcogenide (*e.g.* CrSe_3), metallic (*e.g.* Fe_8B_2) and fluoride (*e.g.* ZnF_2 , ZrF_4 and BeF_2) glasses.

1.3 Network modifiers

Thus far the discussion has been limited to simple single oxide glasses, which have limited applications. Another class of oxides is defined which can be added to the oxide glasses to change their physical properties and produce more useful materials. These are termed modifying oxides or network modifiers and include most oxides not in the list of formers above. For example, silicate glasses doped with rare earth oxides (*e.g.* Er_2O_3) lend themselves to applications in optical amplification [16]. It should be noted that the network modifiers cannot form glasses by themselves.

The network modifiers alter the structure of the glass, which can no longer be thought of in terms of the CRN. Instead a new theory was developed called the modified random network (MRN) model [17, 18], which accounts for the alterations to the basic network. Using SiO_2 as an example, where each SiO_4^{4-} tetrahedron is connected to four others *via* Si-O-Si bonds, addition of a modifier such as CaO causes the [O]/[Si] fraction to increase. The consequence of this is the formation of negatively charged, unconnected oxygen atoms (*i.e.* $-\text{Si-O}^-$), corresponding to disruptions in the silica network connectivity. The modifying Ca^{2+} ions can coordinate with the disconnected oxygen atoms and adapt their local environment to satisfy their own bonding requirements.

1.4 Network intermediates

TiO_2 is an example of an oxide that appears to act as both former and modifier depending on the nature and composition of the other glass components. It is not capable of forming a glass on its own, but is thought to aid connectivity in the presence of another former. The actual role of intermediates is still unclear and stimulates a great deal of discussion in the glass science community.

1.5 Other structural theories

In addition to the Zacharisen CRN and the MRN theories there are a number of different models that pertain to the structure of glasses. A notable example is the crystallite model, which has found favour in the past [19] and occasionally in the present [20]. According to the crystallite model [21], a glass can be envisaged as an assembly of very small crystals of the same structure as the corresponding crystalline

counterpart. Hence, some useful information about the glass structure can be extracted by comparison with the analogous crystalline polymorphs. It is now generally accepted that discrete crystallites do not exist in simple glasses (*e.g.* SiO₂ [22]). Instead the crystallite theory has been adapted and is presented in terms of two regions. One is a highly ordered region while the second is significantly less ordered. The structure can then be thought of as clumps of the ordered region linked together by the less ordered connecting material, which corresponds to fluctuations in the degree of intermediate range order [14]. Galeener and Wright [23] argue that the crystallite model does not agree with neutron diffraction or Raman spectroscopy.

1.6 Ranges of order in an amorphous solid

The disorder can be defined in terms of various ranges of order over which the structure can be described [14]:

Short range order

Typically over the range of 0-4 Å, the short range order describes the basic structural unit or coordination polyhedra of the material (*e.g.* SiO₄⁴⁻ tetrahedra in silica glass). Amorphous materials tend to be relatively ordered in this regime, which is easily probed with diffraction experiments.

Medium range order

The medium range order (4-20 Å) is the range which describes the interconnection or relative orientation of adjacent units in the structure.

Long range order

Due to the lack of clearly definable order on a scale greater than 20 Å, it is not possible to interpret and/or define trends of properties over this range using standard diffraction experiments. Phase separation and fluctuations in density are observed on this scale and computational modelling is more favourable in this regime although small angle scattering and optical scattering may provide information depending on the size of the fluctuations.

1.7 The structure of phosphate glasses

Reviews on the structure of phosphate glasses are given by Van Wazer [2], Abe [24], Martin [25] and Brow [26], while Knowles [27] and Abou Neel *et al.* [28] give an account of phosphate glasses with respect to biomedical applications. Hoppe *et al.* [29] offer a review on the structural specifics of phosphate glasses determined by diffraction experiments. This section offers a broad overview of the structure of phosphate glasses. References are given where additional information may be required and the aforementioned authors provide extensive detail.

All phosphate glasses are formed from tetrahedral PO_4^{3-} units. In vitreous P_2O_5 each unit is connected to three others *via* bridging oxygen (BO) atoms. The fourth oxygen atom must balance the valence for the unit and is therefore unable to form connections to other tetrahedral units since phosphorus has a valence of +5. This is known as a non-bridging oxygen (NBO). The tetrahedral units are best described in the Q^n notation, where n is the number of BOs per unit, such that vitreous P_2O_5 is completely Q^3 . As described above, modifying oxides can be added to disrupt the network having the effect of creating NBOs. Phosphates fall into one of four classifications depending on the ratio of number of oxygen to number of phosphorus atoms ($[\text{O}]/[\text{P}]$) [26, 27] as shown in Table 1.1.

$[\text{O}]/[\text{P}]$ fraction	Classification	Q^n
4	Orthophosphate	Q^0
3.5	Pyrophosphate	Q^1
3	Metaphosphate	Q^2
2.5	Ultraposphate	Q^3

Table 1.1: Phosphate classification based on the ratio of oxygen to phosphorus atoms in a sample.

The addition of a modifying oxide to P_2O_5 to the point where the fraction $[\text{O}]/[\text{P}] = 3$ produces a metaphosphate glass, which contains only Q^2 phosphate units. In this case the tetrahedral units have a tendency to form long chains and rings and the loose NBOs can coordinate with the modifying ions since they have a net negative charge. It is possible to add more modifiers until materials that contain predominantly Q^1 (end groups and $\text{P}_2\text{O}_7^{4-}$ dimers) and Q^0 (isolated PO_4^{3-} tetrahedra) species are produced. Phosphate materials with $[\text{O}]/[\text{P}]$ not equal to those shown in the Table 1.1 are

composed of a mixture of Q^n groups. The Q^n groups are shown pictorially in Figure 1.3.

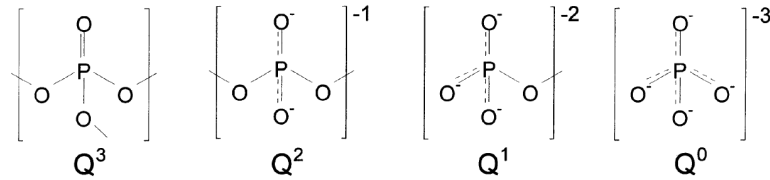


Figure 1.3: Q^n groups for phosphate tetrahedra from Brow [26].

The P-NBO and P-BO distances vary depending on which Q^n group is present. Hoppe *et al.* [29] present Figure 1.4, where the positions and magnitudes of the P-NBO and P-BO (referred to as P- O_T and P- O_B respectively by Hoppe *et al.*) correlations are shown as a function of the molar ratio, $y = [M_{2\nu}O]/[P_2O_5]$, where M is the modifying cation (*e.g.* Ca^{2+} , Na^+ , Zn^{2+} , *etc.*) and ν is the valence of the cation.

Closer inspection of the metaphosphate composition ($y = 1.0$) reveals equal proportions of P-NBO and P-BO corresponding to two NBOs and two BOs per tetrahedral unit. In vitreous P_2O_5 the PO_4^{3-} units have one short P-NBO (double bonded oxygen) and three long P-BO distances. The pyrophosphate ($y = 1.94$) sample shows the opposite ratio of P-O bonds with three P-NBO and one P-BO. It should be noted that as y (and $[O]/[P]$) increases the P-NBO distance becomes longer. This can be understood in terms of the “extra bond” (due to phosphorus having a valence of +5), which becomes delocalised as the network becomes less connected (see Figure 1.3) causing the NBOs to be less strongly bound to the central phosphorus atom.

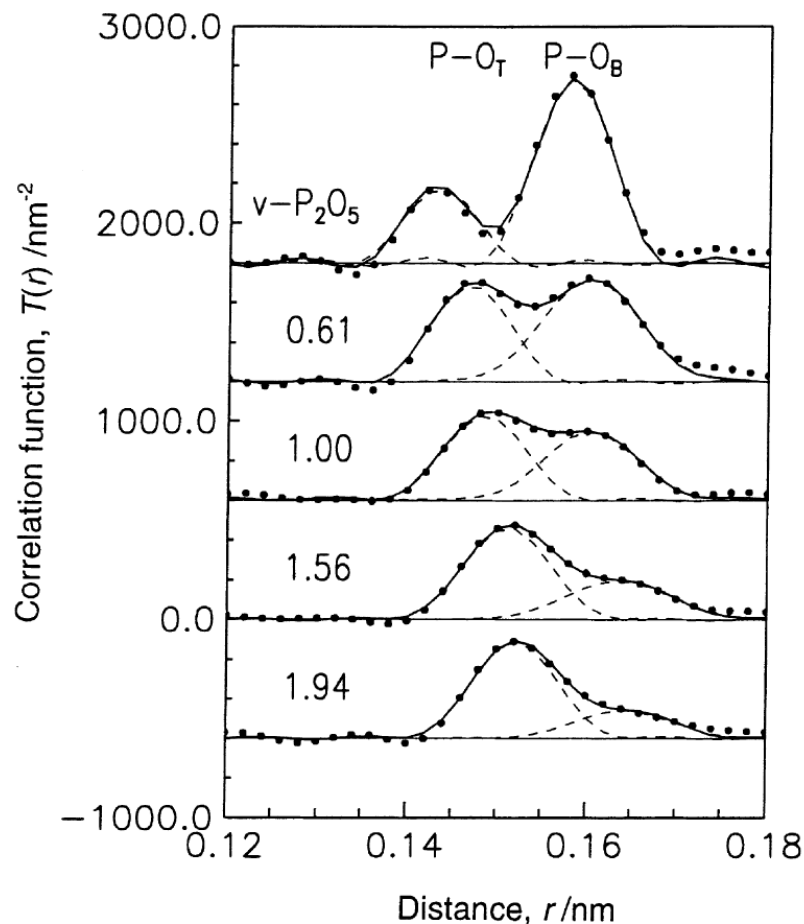


Figure 1.4: Lengths and magnitudes of the P-O correlations as a function of the molar ratio, $y = 1.94$ (Q^1), 1.56 (Q^1/Q^2), 1.00 (Q^2), 0.61 (Q^2/Q^3) and vitreous P_2O_5 (Q^3). From Hoppe *et al.* [29].

Hoppe *et al.* also report on the effect of different modifying cations on the lengths of the P-O bonds. Figure 1.5 shows the P-O correlations in five metaphosphate glasses with different modifiers. There is a fairly large split between the P-NBO and P-BO bonds in KPO_3 while the splitting is significantly reduced in AlP_3O_9 . This is explained in terms of the cation field strength shifting the local electron density away from the BOs. This effect cannot strictly be related to the cation field strength because the PbP_2O_6 P-O peak is less split than that of the LaP_3O_9 even though the nominal field strength of La^{3+} is less than the Pb^{2+} cation.

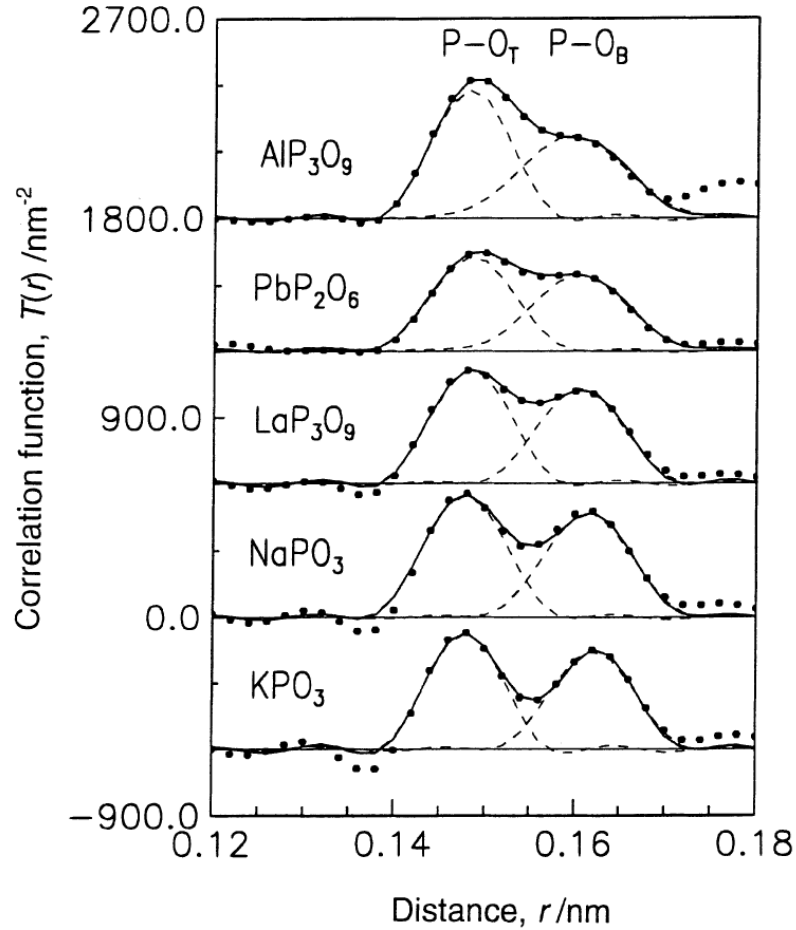


Figure 1.5: P-O bond length distribution for metaphosphate glasses with different modifying cations. From Hoppe *et al.* [29].

The base composition used in this study is $(P_2O_5)_{50}(CaO)_{30}(Na_2O)_{20}$, which has been studied both in terms of its physical and biological properties [30, 31]. Pickup *et al.* [32] have conducted neutron diffraction and ^{31}P nuclear magnetic resonance (NMR) studies on a similar ternary glass, $(P_2O_5)_{50}(CaO)_{40}(Na_2O)_{10}$, and the related binary systems, $(P_2O_5)_{50}(CaO)_{50}$ and $(P_2O_5)_{50}(Na_2O)_{50}$. All samples have $[O]/[P] = 3$ and are therefore metaphosphates.

The neutron diffraction data revealed that the average P-O distance was 1.55 \AA and that the first O-O distance was 2.52 \AA . Using this information the average O-P-O bond angle could be determined trigonometrically as 108.8° , which is consistent with the previously mentioned PO_4^{3-} network forming tetrahedral units (the tetrahedral angle being 109.5°). The P-NBO and P-BO bond lengths appear to become more similar

when Na^+ is replaced by Ca^{2+} (*i.e.* as the cation field strength increases) in agreement with Hoppe *et al.* [29]. Pickup *et al.* suggest that this corresponds to an increase in the covalency of the metal-NBO bonding; a conclusion further supported by the ^{31}P NMR results in the same study. The Ca-O bond has an average length of 2.34 Å with each Ca^{2+} being surrounded by ~5 NBOs within the Ca-O polyhedra, whilst each Na^{2+} is coordinated by ~4 NBOs at an average distance of 2.33 Å. The inter-tetrahedral P-P distance is reported as being at 2.93 Å with each phosphorus atom being neighboured by two others, which is consistent with interconnected PO_4^{3-} units forming chain-like structures.

The work of Wetherall *et al.* [33] further elucidates the structure of $(\text{P}_2\text{O}_5)_{50}(\text{CaO})_{50}$ using reverse Monte Carlo simulation and fitting of high energy X-ray and neutron diffraction data. Again the P-NBO, P-BO and first O-O correlations confirm the existence of interconnected PO_4^{3-} tetrahedral units expected in metaphosphates. It should be noted that, on the strength of their RMC model, Wetherall *et al.* replaced the second O-O correlation at 2.82 Å (Hoppe *et al.* [29] and Pickup *et al.* [32]) with a second Ca-O correlation. This is justified by the broad distribution of Ca-O bond lengths in metaphosphate crystals and by the agreement of the fit to X-ray and neutron data. The O-O correlation at 3.26 Å is due to oxygen neighbours in the CaO_x polyhedra. A small portion of the RMC model is shown in Figure 1.6 and demonstrates the phosphate chains being cross-linked by the Ca^{2+} modifiers.

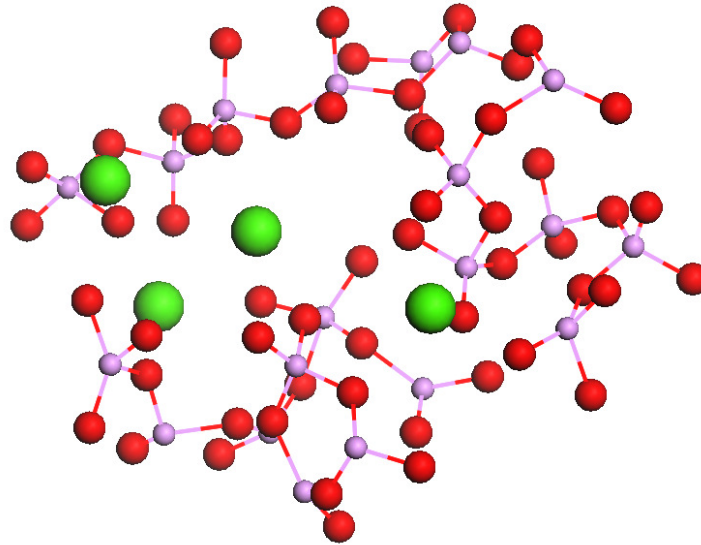


Figure 1.6: A small section of the structural model produced by Wetherall *et al.* [33] showing phosphorus (pink) and oxygen (red) atoms forming tetrahedral chains and calcium (green) atoms coordinating with the NBOs.

This fundamental understanding of the phosphate network forms the basis of the structural analysis presented in this thesis.

1.8 Biomaterials

Current biomaterials include steel, titanium and various polymers. These can be used individually or in combination and have good strength and durability but, as a result, can cause damage to surrounding soft tissue or bone. These materials are also selected for their bioinertness, meaning that they can be introduced into the body with minimal interaction with its surrounding tissue. However, this is rarely the case and a recent study reveals the presence of titanium ions that have diffused into the tissue surrounding an implant [34]. Biocompatible glasses have the potential to supplement or even supersede these traditional biomaterials in some applications.

The first bioactive glass was developed by Hench [35, 36] in the late 1960s. It is available commercially under the name BioGlass[®] but is also known as 45S5 and is composed of SiO₂, Na₂O, CaO and P₂O₅. The key features of BioGlass[®] that make it highly bioactive in an aqueous medium are:

- it contains less than 60 mol% SiO₂
- has high Na₂O and CaO content

- has high CaO:P₂O₅ ratio

In vivo tests show that BioGlass[®] induces gene activation in the tissue surrounding the implant, resulting in osteoblast attachment and eventually bone mineral formation [37]. This process is thought to be a response to the initial rapid loss of calcium ions from the glass matrix into the nearby tissue [38].

Since the seminal work of Hench, a significant amount of research has been devoted to the development of biomaterials in general and as a result there are many new biomaterials including melt derived glasses, polymer hybrids, sol-gel derived bioceramics and nanocomposites [39, 40]. These cover a wide range of applications, such as temporary supports for both soft and hard tissue, coatings on trans-dermal devices and permanent implants.

The materials under investigation here are novel phosphate based glasses, which have been found to exhibit unique properties that are of biomedical interest [27, 28, 41-45]. The abundance of easily hydrolysed P-O-P bonds in phosphate based glasses mean that they are soluble in an aqueous environment. The temporal characteristics of the dissolution can be tailored for specific applications with the addition of modifying metal ions [27]. Soluble glasses that contain ions normally found in the body are classed as bioresorbable, meaning that they can dissolve completely without causing any adverse effects to the surrounding tissue or disruption to normal biological processes. Bioresorbable phosphate based glasses of the formulation (P₂O₅)₅₀(CaO)_{50-x}(Na₂O)_x, with CaO content > 24 mol%, have been shown to exhibit good biocompatibility [46]. Their versatility has allowed them to be used in various biomedical applications. For example, fibres drawn from the melt are particularly useful as temporary supports in tissues with medium to high anisotropy such as muscle and ligaments [47]. The addition of metal ions such as Ag⁺ [43, 48] and Ga³⁺ [45] yield glasses that are antibacterial and could be of particular use in implant surgery, where a significant numbers of patients require post-surgery, infection-related treatment.

1.9 Summary

In these materials it is important to consider how the structure gives rise to the biomedical properties and how these properties can be controlled by manipulating the composition. Perhaps the most important property of phosphate glasses is the solubility which determines how fast ions are released from the material, how well cells attach and proliferate and how chemically durable the glass is. It has been shown that varying the concentration of metal ions in the composition can be used to control the solubility. For example, Franks *et al.* [49] showed that the dissolution rate of $(\text{P}_2\text{O}_5)_{45}(\text{CaO})_x(\text{Na}_2\text{O})_{55-x}$ exhibits an inverse trend with respect to the CaO concentration. Measurements show that the Ca^{2+} ions induce a structural change in the phosphate network where the connectivity decreases, giving rise to the varying solubility. Investigations such as these have shown that it is possible to reveal the structural origin of the composition dependent properties.

1.10 References

- [1] N. J. Kreidl and W. A. Weyl, *J Am Chem Soc* **24** (1941), p. 372.
- [2] J. R. Van Wazer, Phosphorus and its compounds, Interscience, New York (1958).
- [3] E. Kordes and R. Nieder, *Glastechn. Ber.* **41** (1968), p. 41.
- [4] E. Kordes, W. Vogel and R. Feterowsky, *Elektrochem.* **57** (1953), p. 282.
- [5] M. J. Weber, *J. Non-Cryst. Solids* **123** (1990), p. 208.
- [6] J. H. Campbell and T. I. Suratwala, *J. Non-Cryst. Solids* **263-264** (2000), p. 318.
- [7] R. K. Brow, L. Kovacic and R. E. Loehman, *Ceram. Trans.* **70** (1996), p. 177.
- [8] C. J. Quinn, G. H. Bell and J. E. Dickinson, *Proceedings of the XVIth International Congress on Glass* **4** (1992), p. 79.
- [9] D. E. Day, Z. Wu, C. S. Ray and P. Hrma, *J. Non-Cryst. Solids* **241** (1998), p. 1.
- [10] J. B. Bates, N. J. Dudney, G. R. Gruzalski, R. A. Zuhr, A. Choudhury, C. F. Luck and J. D. Robertson, *Solid State Ionics* **53-56** (1992), p. 647.
- [11] J. Fu, *J. Mater. Sci.* **33** (1998), p. 1549.
- [12] W. H. Zachariasen, *J Am Chem Soc* **54** (1932), p. 3841.
- [13] S. R. Elliott, The Physics and Chemistry of Solids, John Wiley & Sons Ltd., Chichester (1998).
- [14] A. C. Wright, Experimental Techniques of Glass Science, American Ceramic Society, Ohio (1993).
- [15] J. E. Shelby, Introduction to glass science and technology, The Royal Society of Chemistry, Cambridge (1997).
- [16] G. C. Righini, S. Pelli, M. Brenchi, M. Ferrari, C. Duverger, M. Montagna and R. Dall'igna, *J. Non-Cryst. Solids* **284** (2001), p. 223.
- [17] G. N. Greaves, *J. Non-Cryst. Solids* **71** (1985), p. 203.
- [18] G. N. Greaves, A. Fontaine, P. Lagarde, D. Raoux and S. J. Gurman, *Nature* **293** (1981), p. 611.
- [19] C. J. Phillips, *J. Non-Cryst. Solids* **63** (1983), p. 347.
- [20] M. R. Ebeid, S. K. Abdelraheem, E. M. Abdel-Minem, K. Abdel-Hady and A. A. Ramadan, *Egypt. J. Sol.* **23** (2000), p. 1.
- [21] A. A. Lebedev, *Trans. State Optical Inst.* **2** (1921), p. 1.

- [22] B. E. Warren, *Chem. Rev.* **26** (2002), p. 237.
- [23] F. L. Galeener and A. C. Wright, *Solid State Commun.* **57** (1986), p. 677.
- [24] Y. Abe In: M. Grayson and E. J. Griffith, *Topics in Phosphorus Chemistry*, Wiley, New York (1983).
- [25] S. W. Martin, *Eur. J. Solid State Chem.* **28** (1991), p. 163.
- [26] R. K. Brow, *J. Non-Cryst. Solids* **263** (2000), p. 1.
- [27] J. C. Knowles, *J. Mater. Chem.* **13** (2003), p. 2395.
- [28] E. A. Abou Neel, D. M. Pickup, S. P. Valappil, R. J. Newport and J. C. Knowles, *J. Mater. Chem.* **19** (2009), p. 690.
- [29] U. Hoppe, G. Walter, R. Kranold and D. Stachel, *J. Non-Cryst. Solids* **263** (2000), p. 29.
- [30] I. Ahmed, M. Lewis, I. Olsen and J. C. Knowles, *Biomaterials* **25** (2004), p. 491.
- [31] M. Bitar, V. Salih, V. Mudera, J. C. Knowles and M. P. Lewis, *Biomaterials* **25** (2004), p. 2283.
- [32] D. M. Pickup, I. Ahmed, P. Guerry, J. C. Knowles, M. E. Smith and R. J. Newport, *J. Phys.: Condens. Matter* **19** (2007), 415116.
- [33] K. M. Wetherall, D. M. Pickup, R. J. Newport and G. Mountjoy, *J. Phys.: Condens. Matter* **21** (2009), 035109.
- [34] O. Addison, private communication, Birmingham (2009).
- [35] L. L. Hench, *J. Am. Ceram. Soc.* **74** (1991), p. 1487.
- [36] L. L. Hench, *Biomaterials* **19** (1998), p. 1419.
- [37] W. Cao and L. L. Hench, *Ceram. Int.* **22** (1996), p. 493.
- [38] R. J. Newport, L. J. Skipper, V. FitzGerald, D. M. Pickup, M. E. Smith and J. R. Jones, *J. Non-Cryst. Solids* **353** (2007), p. 1854.
- [39] J. R. Jones, *Journal of the European Ceramic Society* **29** (2009), p. 1275.
- [40] N. A. Peppas and R. Langer, *Science* **263** (1994), p. 1715.
- [41] E. A. Abou Neel and J. C. Knowles, *J. Mater. Sci.: Mater. Med.* **19** (2008), p. 377.
- [42] E. A. Abou Neel, L. A. O'Dell, M. E. Smith and J. C. Knowles, *J. Mater. Sci.: Mater. Med.* **19** (2008), p. 1669.
- [43] I. Ahmed, D. Ready, M. Wilson and J. C. Knowles, *J. Biomed. Mater. Res., Part A* **79A** (2006), p. 618.

- [44] S. P. Valappil, D. M. Pickup, D. L. Carroll, C. K. Hope, J. Pratten, R. J. Newport, M. E. Smith, M. Wilson and J. C. Knowles, *Antimicrob. Agents Chemother.* **51** (2007), p. 4453.
- [45] S. P. Valappil, D. Ready, E. A. Abou Neel, D. M. Pickup, W. Chrzanowski, L. A. O'Dell, R. J. Newport, M. E. Smith, M. Wilson and J. C. Knowles, *Adv. Funct. Mater.* **18** (2008), p. 732.
- [46] V. Salih, K. Franks, M. James, G. W. Hastings, J. C. Knowles and I. Olsen, *J. Mater. Sci.: Mater. Med.* **11** (2000), p. 615.
- [47] I. Ahmed, C. A. Collins, M. P. Lewis, I. Olsen and J. C. Knowles, *Biomaterials* **25** (2004), p. 3223.
- [48] I. Ahmed, E. A. Abou Neel, S. P. Valappil, S. N. Nazhat, D. M. Pickup, D. Carta, D. L. Carroll, R. J. Newport, M. E. Smith and J. C. Knowles, *J. Mater. Sci.* **42** (2007), p. 9827.
- [49] K. Franks, I. Abrahams and J. C. Knowles, *J. Mater. Sci.: Mater. Med.* **11** (2000), p. 609.

Chapter 2 – Theory

2.1 Introduction

This chapter discusses the theory of X-ray and neutron scattering and the relation of the theory to the experimentally obtained interference function. The real space correlation function can be obtained from the Fourier inversion of the interference function and can be used to determine structural information, such as bond distances and coordination numbers. The theory of X-ray absorption spectroscopy is also covered and can be used to determine element specific information on the local structure in an amorphous solid. Although the scattering process can be described generically, there are important differences between X-ray and neutron scattering that will be made clear.

2.2 The scattering cross-section

An important concept in any scattering experiment is the scattering cross-section. Imagine an experiment in which a monochromatic beam of neutrons or X-rays (hereafter generically referred to as “probes”) are incident upon a sample containing N atoms. The total scattering cross-section is defined as:

$$\sigma = \frac{N_S}{N\Phi} \quad 2.1$$

where Φ is the incident probe flux and N_S is the number of probes scattered per unit time. The differential scattering cross-section, which is the quantity measured in a diffraction experiment, is written as:

$$\frac{d\sigma}{d\Omega} = \frac{N'_S}{N\Phi d\Omega} \quad 2.2$$

where N'_S is the number of probes scattered per unit time into the solid angle $d\Omega$. Figure 2.1 represents the scattering process and applies to any scattering probe.

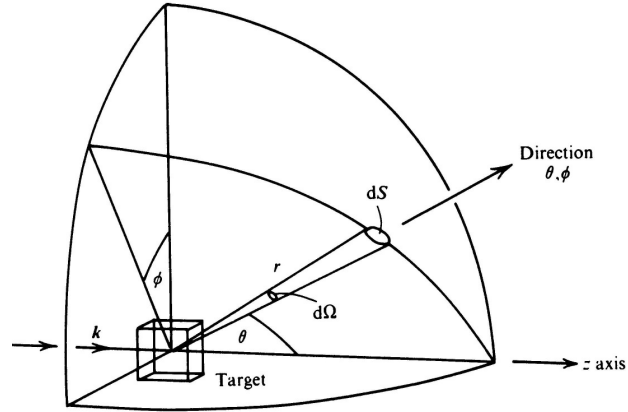


Figure 2.1: Geometrical representation of a diffraction experiment. Note that $dS = r^2 d\Omega$ and k represents the direction of the incident beam of probes [1].

The scattering cross-section is now derived from the point-of-view of the measured scattering intensity.

2.3 Scattering in general

The formal derivation of diffraction by an amorphous material can be followed in terms of the Van Hove [2] correlation functions, and such a derivation is presented by Wright *et al* [3-6]. The following theory is based on the simpler derivation by Urnes [7].

In a scattering experiment, a scattering probe of wavevector, \bar{k}_0 , and energy, E_0 , is incident on a sample and is scattered through an angle, 2θ , with a final wavevector, \bar{k} , and energy, E , such that each scattering event is characterised by an energy transfer:

$$\hbar\omega = E_0 - E \tag{2.3}$$

and a momentum transfer:

$$\hbar\bar{Q} = \hbar\bar{k}_0 - \hbar\bar{k} \tag{2.4}$$

Where $\hbar\omega$ and $\hbar\bar{Q}$ is the energy and momentum transferred to the sample respectively. In order to determine the structure of a sample, only values of \bar{Q} where

the scattering is elastic (*i.e.* $\hbar\omega=0$) are useful. In this case the probe wavelength, λ , remains unchanged and the magnitude of \bar{Q} is given by Equation 2.5.

$$|\bar{Q}| = Q = \frac{4\pi \sin \theta}{\lambda} \quad 2.5$$

In reality, a detector at fixed scattering angle, 2θ , records both the elastic and inelastic contribution. It can be said to be performing integration over ω at a constant scattering angle. This is the basis of total scattering, and a correction therefore needs to be applied to the raw data to remove the inelastic contribution. It should be noted that the inelastically scattered probe can be used to gain information about the dynamics of the sample [8], but discussions on this subject are beyond the scope of this work.

2.4 Scattering by a group of atoms

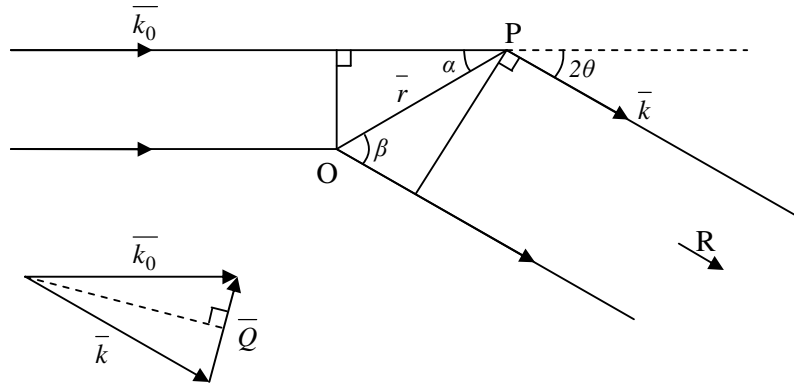


Figure 2.2: Scattering of a probe by sample through and angle 2θ .

The probe can be considered to exhibit quantum mechanical behaviour (*i.e.* having wave-like properties). Figure 2.2 depicts a situation where there is an atom at P a vector distance \bar{r} away from arbitrary origin O . A detector is placed at some distance R , such that $R \gg r$. The phase, at R , of a wave scattered at P relative to one scattered at O is:

$$\Phi = \frac{2\pi(r \cos \alpha - r \cos \beta)}{\lambda} \quad 2.6$$

By substitution of $\bar{r} \cdot \bar{k}_0 = (2\pi/\lambda)r \cos \alpha$ and $\bar{r} \cdot \bar{k} = (2\pi/\lambda)r \cos \beta$, the phase difference becomes:

$$\Phi = \bar{r} \cdot (\bar{k}_0 - \bar{k}) = \bar{r} \cdot \bar{Q} \quad 2.7$$

and the amplitude of the scattered wave for this single atom is:

$$A_1(Q) = a(Q)e^{i\bar{r} \cdot \bar{Q}} \quad 2.8$$

In Equation 2.8 $a(Q)$ represents either the X-ray form factor, $f(Q)$, or the neutron scattering length, b , as appropriate (the meanings of which are explained later). When the scattering takes place from a system of N atoms, the amplitudes need to be summed over all atoms, taking into account the relative phases.

$$A_N(Q) = \sum_n^N a_n(Q)e^{i\bar{r}_n \cdot \bar{Q}} \quad 2.9$$

The scattering intensity is obtained by multiplying $A_N(Q)$ by its complex conjugate.

$$I_N(Q) = A_N(Q)A_N^*(Q) = \sum_p \sum_q a_p(Q)a_q(Q)e^{i\bar{r}_{pq} \cdot \bar{Q}} \quad 2.10$$

where p and q are any two individual atoms regardless of type. It should be noted that the summations over p and q are taken over all atoms in the sample and that $I_N(Q)$ depends on the interatomic distance vector $\bar{r}_{pq} = \bar{r}_p - \bar{r}_q$ and is independent of the arbitrary origin. Equation 2.10 is universal for crystals, amorphous solids, liquids and gasses because no assumptions have been made about the atomic arrangements in the sample.

2.5 Scattering by an isotropic sample

An isotropic distribution, by definition, is one that is the same in all directions. A sample described as isotropic has no preferred orientation such that, for any given

interatomic vector, $\overline{r_{pq}}$, there will be other equivalent vectors in the sample in all possible orientations with respect \overline{Q} . This allows the vector formalism to be relaxed and Equation 2.10 can be rewritten as an average over all directions.

$$I_N(Q) = \sum_p \overline{a_p^2(Q)} + \sum_{p \neq q} \overline{a_p(Q)a_q(Q)} \frac{\sin(r_{pq}Q)}{r_{pq}Q} \quad 2.11$$

Equation 2.11 is known as the Debye equation and can be used to calculate the scattered intensity provided that all the interatomic distances are known or can be calculated. In an amorphous material, the interatomic vectors are unknown and it becomes necessary to look at the atomic correlations in real space to make sense of the structure.

2.6 Radial distribution functions

The atomic arrangement is related to the radial density function, $\rho(r)$, which describes how the number density fluctuates as a function of radial distance from an arbitrary origin atom. It should be noted that $\rho(r)$ is the average over all atoms in the sample taken as centre. Equation 2.12 defines $\rho(r)$ for a sample of N atoms.

$$\rho(r) = \frac{\sum_n^N \rho_n(r)}{N} \quad 2.12$$

where $\rho_n(r)$ is the radial density distribution around the n^{th} atom. The total correlation function is defined:

$$t(r) = 4\pi r \rho(r) \quad 2.13$$

and the differential correlation function, $d(r)$, is obtained by subtracting the average density term from $t(r)$.

$$d(r) = 4\pi r [\rho(r) - \rho_0] \quad 2.14$$

where ρ_0 is the average number density in the bulk sample. It is useful to recognise that for a sample containing m different atom types, $t(r)$, and hence $d(r)$, can be represented as the sum of $m(m+1)/2$ independent component correlations.

$$t(r) = \sum_i \sum_j t_{ij}(r) = \sum_i \sum_j 4\pi r \rho_{ij}(r) \quad 2.15$$

Equation 2.15 defines the distribution of atom type j about the i^{th} atom in one compositional unit of the sample. A composition unit contains a number of atoms of each type in proportion to the composition of the sample. It is typical to normalise the number of atoms per compositional unit to unity. A diffraction experiment measures a combination of correlations, but the weighting given to each correlation depends on the probe being used. It is now possible to rewrite Equation 2.11 in terms of $t_{ij}(r)$.

$$I(Q) = \sum_i \overline{a_i^2(Q)} + \sum_i \sum_j \overline{a_i(Q)a_j(Q)} \int_0^\infty t_{ij}(r) \frac{\sin Qr}{Q} dr \quad 2.16$$

$I(Q)$ is the scattering intensity per compositional unit. The second term on the right hand side of Equation 2.16 can be broken down into two further terms, the first involving $d_{ij}(r)$ and the second involving ρ_0 .

$$I(Q) = \sum_i \overline{a_i^2(Q)} + \sum_i \sum_j \overline{a_i(Q)a_j(Q)} \int_0^\infty d_{ij}(r) \frac{\sin(Qr)}{Q} dr + \int_0^\infty 4\pi r \rho_0 \left[\sum_i \overline{a_i(Q)} \right]^2 \frac{\sin Qr}{Q} dr \quad 2.17$$

The third term on the right hand side of Equation 2.17, usually called $I_0(Q)$, becomes a δ -function at $Q = 0$ for a sample of infinite extent. It is assumed that the contribution of the third term is condensed into unscattered primary beam and is, therefore, not recorded. It should be noted that $I(Q)$ is equivalent to the measured quantity $d\sigma/d\Omega$ defined earlier.

The part of $I(Q)$ that is of interest is called the interference function, $i(Q)$, and is defined as:

$$Qi(Q) = Q \left[I(Q) - \sum_i \overline{a_i^2(Q)} - I_0(Q) \right] = \sum_i \sum_j \overline{a_i(Q) a_j(Q)} \int_0^\infty d_{ij}(r) \sin(Qr) dr \quad 2.18$$

From Equation 2.18 it can be seen that $Qi(Q)$ is the weighted sum of the sine Fourier transform of $d_{ij}(r)$, with $\overline{a_i(Q)}$ and $\overline{a_j(Q)}$ being the weighting factors.

2.7 Experimental real space correlation functions

It is necessary to use a Fourier transform to extract the real space correlation function from the experimentally obtained interference function. Theoretically, the experimental differential correlation function, $D(r)$, is the sine Fourier transforms of $Qi(Q)$, which is correct if data could be collected from zero up to an infinite extent in Q . In this case it would follow that $D(r)$ is the sum over all atom pairs of the component differential correlation functions, $d_{ij}(r)$. Experimentally, data can not be collected over an infinite extent in Q and the relationship between $D(r)$ and $d_{ij}(r)$ is not straightforward and the Fourier transform requires the use of a modification function, $M(Q)$:

$$D(r) = \frac{2}{\pi} \int_0^\infty Qi(Q) M(Q) \sin(Qr) dQ \quad 2.19$$

The form of $M(Q)$ is discussed later, but it is important to note that $M(Q) = 0$ for $Q > Q_{max}$. The experimental total correlation function, $T(r)$, can be developed from $D(r)$ with the addition of the so-called “average density” term, $T^0(r)$, which is the Fourier transform of $QI_0(Q)$.

$$T(r) = D(r) + T^0(r) = \sum_i \sum_j t_{ij}^\bullet(r) \quad 2.20$$

The superscript filled circle (\bullet) in Equation 2.20 is used to identify a component that is probe dependent. Equation 2.20 defines $T(r)$ as being the sum of $t_{ij}^\bullet(r)$, which is not the same as $t_{ij}(r)$ defined in Equation 2.15, but these two functions are related by convolution.

$$t_{ij}^{\bullet}(r) = \int_0^{\infty} t_{ij}(r') [P_{ij}^{\bullet}(r-r') - P_{ij}^{\bullet}(r+r')] dr' \quad 2.21$$

r' is a dummy convolution variable and $P_{ij}^{\bullet}(r)$ is the component peak function that accounts for the real space resolution due to the finite upper limit of Q .

2.8 Application to neutron diffraction

Neutrons are scattered by the component atom nuclei, which have a property called the scattering length, denoted by the letter b , which is proportional to the strength of the scattering. The scattering length usually assumes some real value, but there are a few cases where b is complex and varies rapidly with the energy of the interacting neutrons. Examples of atoms that exhibit this behaviour (at neutron energies of interest to structural studies) are ^{103}Rh , ^{113}Cd , ^{157}Gd and ^{176}Lu . The scattering of such nuclei is a resonance phenomenon and is associated with the formation of a compound nucleus (original nucleus + interacting neutron) with an energy close to an excited state [1]. The majority of nuclei have scattering lengths where the imaginary part is vanishingly small or zero, and the present discussion is restricted to nuclei of this type. The values of the scattering lengths depend on the particular component nuclei and the nucleus-neutron system spin state, which is either $I+1/2$ or $I-1/2$, given that the interacting neutron has spin $1/2$ and the component nucleus has spin I (not equal to zero). On this basis, every nucleus with non-zero spin has two values of the scattering length, which shall be called b^+ and b^- . If the nucleus has zero spin then the nucleus-neutron system can only have spin $1/2$ and there is only one value of b . If a complete theory of nuclear potentials/forces existed, it would be possible to calculate b exactly, but such a model does not exist and scattering lengths are determined experimentally and are tabulated in various places, *e.g.* [9]. The scattering length varies erratically with atomic number, and can vary greatly between isotopes of the same element. This property can be exploited to yield structural information about a specific element by providing neutron contrast between two otherwise identical samples. This is the basis of neutron diffraction with isotopic substitution (NDIS), which is discussed later. A real sample can never be prepared so as to be free of impurities or, apart from rare instances (*e.g.* ^{31}P), to contain a single isotope. This gives rise to two categories of

scattering called coherent and incoherent. Coherent scattering arises from correlations between different nuclei at different times and from correlations between a single nucleus and itself at different times [1]. The incoherent contribution is due to the variation of b^+ and b^- from the mean, isotope mixing and impurities in the sample. It is more productive to split $d\sigma/d\Omega$ into distinct and self scattering terms. In this case the self scattering includes all the incoherent contributions and correlations between a nuclei and itself. The self scattering is typically featureless and tends to a constant in Q -space. The distinct scattering contains modulations that are indicative of interference effects, which is understandable because the distinct scattering contains only information about correlations between pairs of atoms in the sample.

Corrections are applied to the raw data to account for sample containment, intrinsic experimental background, multiple scattering and attenuation (see Chapter 3). Although some correction is always necessary, great care should be taken to ensure that they remain small. In neutron diffraction, it is typical to normalise the data to the scattering profile of vanadium, which scatters almost completely incoherently and allows the measured total scattering cross-section to be placed on an absolute scale.

Successful extraction of the distinct scattering intensity by this method relies on the static approximation, which states that the incident neutron energy is large compared to the energies of the nuclei in the sample and that the detector is equally efficient for counting scattered neutrons of any energy. Ultimately, the sample is assumed to be composed of nuclei in fixed positions and that the contribution from inelastic scattering can be neglected. On the whole this is a good approximation, but a correction is still performed to account for inadequacies in this assumption. The correction is due to Placzek [10] and detailed discussions are given elsewhere [8, 11, 12].

The experimentally obtained differential scattering cross-section can be compared to the result of the theoretical derivation in Equation 2.17 for $I(Q)$. Experimentally, $I_0(Q)$ is unmeasured and has been neglected, such that the differential scattering cross-section is defined:

$$\frac{d\sigma}{d\Omega} = I(Q) = i(Q) + \sum_i \overline{a_i^2(Q)} = i(Q) + \overline{b^2} \quad 2.22$$

In Equation 2.22, the weighting factor, $a(Q)$, is replaced by the neutron scattering length, b , which is Q independent. The final term in Equation 2.22 is the self scattering contribution described earlier.

From Equation 2.21, $P_{ij}^*(r)$ becomes $P_{ij}^N(r)$ and the form of $P_{ij}^N(r)$ is due only to the cosine Fourier transform of $M(Q)$.

$$P_{ij}^N(r) = \frac{\overline{b_i b_j}}{\pi} \int_0^\infty M(Q) \cos(rQ) dQ \quad 2.23$$

The cosine transform is used because $M(Q)$ is an even function, unlike $Qi(Q)$, which is odd and requires the sine transform. The values $\overline{b_i}$ and $\overline{b_j}$ are the coherent scattering lengths of atom i and atom j respectively. The experimentally derived neutron total correlation function, $T^N(r)$, is given by:

$$T^N(r) = 4\pi\rho^0 r \left(\sum_i c_i \overline{b_i} \right)^2 + \frac{2}{\pi} \int_0^\infty Qi(Q) M(Q) \sin(rQ) dQ \quad 2.24$$

$T^N(r)$ has units of barns \AA^{-2} .

2.9 The modification function

The effect of $M(Q)$ can be investigated by looking more closely at $P_{ij}^N(r)$. If a sharp truncation is used (*i.e.* $M(Q) = 1$ over the extent of measured Q , hereafter referred to as the step modification function) then $P_{ij}^N(r)$ exhibits pronounced termination ripples on either side of the central maximum [13] (see Figure 2.3). These features can be misinterpreted as being real and can lead to false results. It is possible to reduce the termination ripples by using different forms of $M(Q)$ to damp the high Q oscillations.

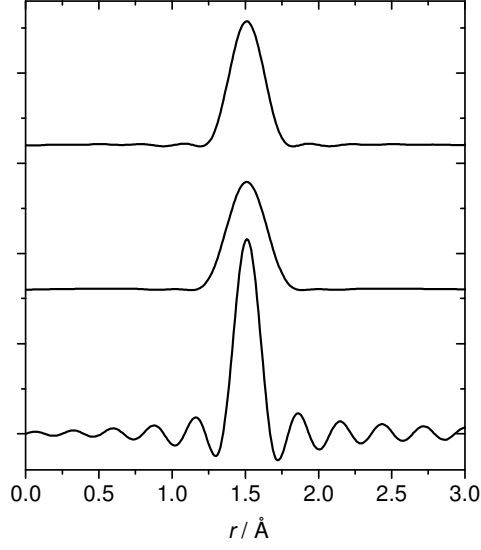


Figure 2.3: Variation in $P_{ij}^N(r)$ using step (bottom), Hanning (middle) and Lorch (top) modification functions.

Many variations of $M(Q)$ have been formulated but two are of particular interest here. The first is the modification function proposed by Lorch [14]:

$$M(Q) = \begin{cases} \sin(\Delta r Q) / \Delta r Q, & Q \leq Q_{\max} \\ 0, & \text{otherwise} \end{cases} \quad 2.25$$

The second is the raised cosine Hanning function:

$$M(Q) = \begin{cases} [1 + \cos(\Delta r Q)] / 2, & Q \leq Q_{\max} \\ 0, & \text{otherwise} \end{cases} \quad 2.26$$

In equations 2.25 and 2.26, Δr defines the experimental real space resolution and is equal to π/Q_{\max} . The different forms of $M(Q)$ are highlighted in Figure 2.4.

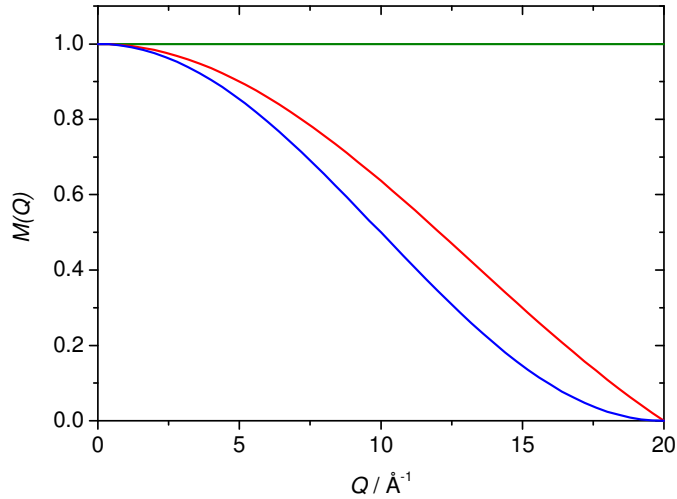


Figure 2.4: Graphical representation of $M(Q)$ over the range $0 \leq Q \leq 20 \text{ \AA}^{-1}$, with Hanning (blue), Lorch (red) and step function (green).

2.10 Special case – NDIS

As mentioned above, some elements have different scattering lengths associated with their different isotopes. A prime example of this is the case of titanium which has two isotopes that are of particular interest in this regard. ^{48}Ti has a coherent scattering length of -6.08 fm and has a natural abundance of 73.8%, while ^{46}Ti has a coherent scattering length of 4.93 fm and comprises 8.2% of natural abundance [9]. It is possible to prepare two samples; one enriched with ^{46}Ti and the other with ^{48}Ti . Chemically, these samples are identical, which can be verified with the use of X-ray diffraction. However, upon investigation with neutrons it is possible to observe differences in $T(r)$ from each sample. In the case of titanium, the difference is accentuated by virtue of the fact that ^{48}Ti has a negative scattering length, resulting from the neutron undergoing a π phase-shift upon interaction. This results in negative peaks in $T(r)$ where there are correlations between titanium and other atom types (with non-negative scattering lengths). There are other elements that can be used for NDIS (notably silver) but titanium is, perhaps, the clearest example.

As shown above, $T(r)$ can be considered as the sum of partial correlation functions, $t_{ij}(r)$ (see Equation 2.20). The difference in real space can be described for two isotopically enriched samples, having total correlations functions $T(r)$ and $T'(r)$ respectively:

$$T_{Aj}(r) = T(r) - T'(r) = c_A^2 (b_A^2 - b'_A{}^2) f'_{AA}(r) + 2 \sum_{j \neq A} c_j c_A b_j (b_A - b'_A) f'_{Aj}(r) \quad 2.27$$

where c and b take their usual meanings. $T_{Aj}(r)$ contains only correlations between the isotopically substituted element, A , and other elements, j (noting that $j = A$ is allowed). Hence the local environment of A can be inspected more closely than would normally be possible by total neutron diffraction alone.

2.11 Application to X-ray diffraction

The quantity that defines the strength of X-ray scattering is the atomic form factor or scattering factor, $f(Q)$. Similar to the neutron scattering length, $f(Q)$ also exhibits resonance behaviour for energies near an absorption edge. This is due to anomalous dispersion, which not only affects the magnitude of the collision photon but also imparts a phase shift; described by a complex component of $f(Q)$. X-ray diffraction experiments tend to be conducted at energies sufficiently removed from an absorption edge (material dependent) that the complex component becomes vanishingly small. Unlike the neutron scattering length, the atomic scattering factor is not independent of Q . In X-ray diffraction the scattering process is between the interacting X-rays and the electrons in the atoms. The process can be thought of as being the absorption of the incident X-ray photon, resulting in the excitation of the electronic system, followed immediately by relaxation and re-emission of an X-ray photon [15]. Since the atomic diameter is comparable to the X-ray wavelength it is necessary to consider intra-atomic interference effects, which accounts for the Q dependence. The forms of $f(Q)$ for most elements have been calculated and modelled as the sum of four Gaussians plus a constant. The atomic scattering factors can be reconstructed using a nine parameter equation:

$$f(Q) = \sum_i^4 a_i e^{-b_i s^2} + c \quad 2.28$$

where a_i , b_i and c are tabulated (see the *International Tables of Crystallography* and [16]) and $s = Q/4\pi$. Where possible the parameters for ionic species were used rather than neutral atoms because electrons involved in bonding are shifted away from their

parent atom effectively creating ionic states and the atoms can no longer be described as isolated. The X-ray differential scattering cross-section can then be defined as per Equation 2.17, with the atomic scattering factors assuming the role of $a(Q)$:

$$\frac{d\sigma}{d\Omega} = I(Q) = i(Q) + \overline{f^2(Q)} \quad 2.29$$

Since the scattering is due to the electron cloud around each atom, the direct sine Fourier transform of the X-ray $i(Q)$ (as Equation 2.19) yields the electronic correlation function. This suffers from poor real space resolution because the electron clouds have a significant size compared to the X-ray wavelength. It is conventional to divide the X-ray $i(Q)$ by the average scattering factor per atom squared, $f_e^2(Q)$, sometimes referred to as the sharpening function. This has the effect of collapsing the scattering to that expected of a point scatterer, with $f_e(Q)$ having the form:

$$f_e(Q) = \sum_i c_i f_i(Q) \quad 2.30$$

where c_i and $f_i(Q)$ are the concentration and scattering factor of the i^{th} atom type in the sample, respectively. This modification means that the X-ray total correlation function, $T^X(r)$, has a different form to the neutron equivalent.

$$T^X(r) = 2\pi^2 \rho^0 r + \int_0^\infty \frac{Q i(Q)}{f_e^2(Q)} M(Q) \sin(rQ) dQ \quad 2.31$$

$T^X(r)$ has units of \AA^{-2} and, for historical reasons, has been multiplied by a factor of $\pi/2$, compared to $T^N(r)$. The X-ray component peak function, $P_{ij}^X(r)$, becomes complicated by the Q -dependent form factors, and for data normalised to the sharpening function is defined by Equation 2.32.

$$P_{ij}^X(r) = \frac{1}{\pi} \int_0^\infty \frac{f_i(Q) f_j(Q)}{f_e^2(Q)} M(Q) \cos(rQ) dQ \quad 2.32$$

Since $f(Q)$ is different for each type of atom, $P_{ij}^X(r)$ is different for each ij atomic pair.

2.12 X-ray absorption spectroscopy

X-ray absorption spectroscopy (XAS) is an element specific technique that can be used to determine the local structure of a specified atom type, even if it is highly diluted in a sample. This is particularly useful to elucidate the structure of multi-component systems, where fitting scattering data can become complicated by the existence of overlapping real space correlations. An XAS measurement is performed with X-rays of sufficient energy to remove electrons from core states to the continuum. The outgoing electron is considered as a quantum mechanical entity resembling a spherical wave emanating from the target atom at its centre.

XAS measurements can be broken down into two parts. X-ray absorption near edge spectroscopy (XANES) is concerned with the region close to the absorption edge. The shape and position of the edge allows determination of the target atom's oxidation state and coordination environment. The second part of XAS measurements is extended X-ray absorption fine structure (EXAFS). This is the region beyond the absorption edge where there is interference between the outgoing and backscattered photoelectrons. Figure 2.5 show a typical XAS trace with the separate regions marked out.

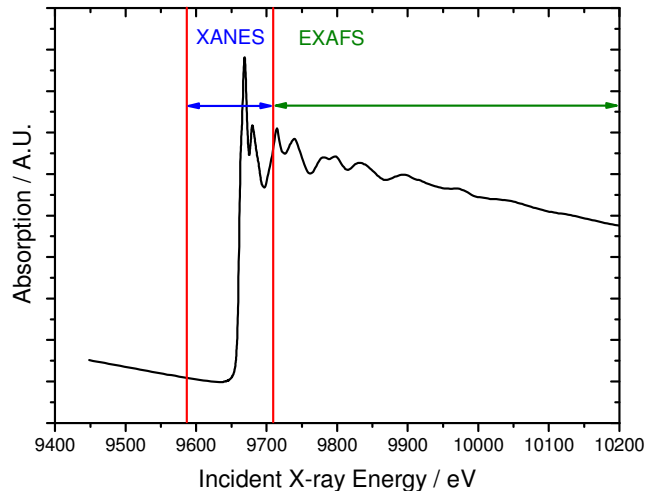


Figure 2.5: XAS spectrum indicating the XANES and EXAFS regions.

XANES

The XANES region starts at approximately 20 eV before the absorption edge and incorporates all the strong oscillations up to approximately 50 eV after the edge. This region is dominated by multiple scattering of the outbound photoelectrons, and the size and shape of the oscillations are determined by the geometrical arrangement of atoms in the local cluster around the absorbing atom. It is possible to gain quantitative information from XANES [17], but this can be very complex and it is more common to compare the shape of the XANES region with reference materials of known structure.

EXAFS

In the EXAFS region the interference effects between emitted and reflected photoelectrons modulate the absorption cross-section. This modulation results in oscillations superimposed on the isolated atom absorption. The theory of EXAFS is complicated and only a broad overview is offered here. In-depth derivations can be found elsewhere [18-20]. In order to quantitatively describe EXAFS the scattering and absorption processes must be separated. The photon absorption cross-section for an atom in a solid is defined as:

$$\sigma(E) = \sigma_0(E)[1 + \chi(E)] \quad 2.33$$

where E is the X-ray photon energy, $\sigma_0(E)$ is the absorption cross-section for an isolated atom and $\chi(E)$ is the EXAFS function representing the modulation in the photoabsorption rate due to scattering processes. $\sigma_0(E)$ is essentially featureless except for sudden jumps that correspond to rapid increases in absorption at energies equal to the electron binding energies for a particular atom. The form of $\sigma_0(E)$ for tin is shown in Figure 2.6.

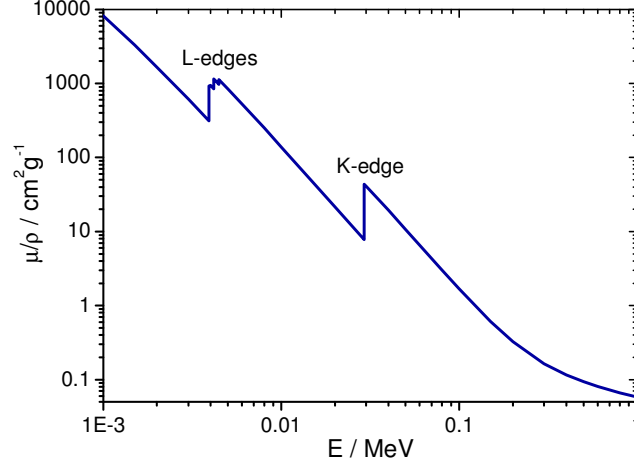


Figure 2.6: Absorption cross-section as a function of photon energy for isolated tin atom. The L_3 , L_2 and L_1 edges are at 3.93, 4.16 and 4.46 keV respectively. The K-edge is at 29.20 keV.

The EXAFS function, $\chi(E)$, is defined as:

$$\chi(E) = \frac{\mu(E) - \mu_0(E)}{\mu_0(E)} \quad 2.34$$

where $\mu_0(E)$ is the background absorption and $\mu(E)$ is the experimentally observed absorption. In order to derive structural parameters from $\chi(E)$, it must be expressed as a function of the photoelectron wavevector, \bar{k} . The magnitude of \bar{k} can be derived from the photon energy using the classical free electron relationship.

$$k = \sqrt{\frac{2m_e}{\hbar^2} (E - E_0)} \quad 2.35$$

E_0 is the threshold energy for the particular absorption edge being studied, E is the incident photon energy, m_e is the mass of the electron and \hbar is Planck's constant divided by 2π . The theory of EXAFS scattering was first developed by Sayers, Stern and Lytle [21], who compared the structures of crystalline and amorphous germanium and simulated the EXAFS signal with a sum of damped oscillations to obtain structural information.

Plane wave theory

Photoelectrons with kinetic energy > 100 eV can be treated as plane waves where they interact with surrounding atoms [19]. In this case, $\chi(k)$, due to a single atom scattering at a fixed distance, R , from the absorbing atom can be written as:

$$\chi(k, R) = \frac{-A(k)}{kR^2} |f(k, \pi, R)| \exp\left[\frac{-2R}{\lambda(k)}\right] \sin(2kR + 2\delta(k) + \psi(k, R)) \quad 2.36$$

where $f(k, \pi, R)$ is the electron backscattering factor for the atom at R and is a complex number of magnitude $|f(k, \pi, R)|$ and phase $\psi(k, R)$. A phase shift, $\delta(k)$, is introduced due to the transit of the photoelectron through the absorbing atom potential. $\lambda(k)$ is the elastic mean free path of the photoelectron and $A(k)$ is an energy independent amplitude factor, which allows for non-EXAFS contributing photo-absorption events, such as multi-electron excitations.

The measured EXAFS signal is the sum of contributions from all central and scattering atoms. The standard expression for the EXAFS equation becomes a sum:

$$\chi(k) = -A(k) \sum_j \frac{N_j}{kR_j^2} |f(k, \pi, R_j)| \exp\left[\frac{-2R_j}{\lambda(k)}\right] \exp[-2\sigma_j k^2] \sin(2kR_j + 2\delta(k) + \psi(k, R_j)) \quad 2.37$$

Equation 2.37 is valid for a shell j containing N_j atoms at a mean distance R_j from the absorbing atom, with a mean square deviation σ_j^2 . The factor $2\sigma_j^2$ is the Debye-Waller factor.

Curved wave theory

More recently the plane wave theory has been extended to accurately model the scattering of photoelectrons with kinetic energies < 100 eV. In this regime the curvature of the photoelectron wave must be considered, which complicates the theoretical derivation of $\chi(k)$ considerably. Curved wave theory is discussed in detail elsewhere [22, 23] and forms the basis of all modern EXAFS analysis programs.

2.13 References

- [1] G. L. Squires, *Introduction to the Theory of Thermal Neutron Scattering*, Dover Publications, Inc., New York (1996).
- [2] L. Van Hove, *Phys. Rev. A* **95** (1954), p. 447.
- [3] D. I. Grimley, A. C. Wright and R. N. Sinclair, *J. Non-Cryst. Solids* **119** (1990), p. 49.
- [4] P. A. V. Johnson, A. C. Wright and R. N. Sinclair, *J. Non-Cryst. Solids* **58** (1983), p. 109.
- [5] R. N. Sinclair and A. C. Wright, *J. Non-Cryst. Solids* **57** (1983), p. 447.
- [6] A. C. Wright and R. N. Sinclair, *J. Non-Cryst. Solids* **76** (1985), p. 351.
- [7] S. Urnes, *Modern Aspects of Vitreous state*, Butterworths, London (1960).
- [8] C. G. Windsor, *Pulsed Neutron Scattering*, Taylor & Francis Ltd., London (1981).
- [9] V. F. Sears, *Neutron News* **3** (1992), p. 26.
- [10] G. Placzek, *Physical Review* **86** (1952), p. 377.
- [11] G. E. Bacon, *Neutron Diffraction*, Oxford University Press, London (1975).
- [12] J. G. Powles, *Molecular Physics* **26** (1973), p. 1325
- [13] A. C. Wright, *Experimental Techniques of Glass Science*, American Ceramic Society, Ohio (1993).
- [14] E. Lorch, *J. Phys. C: Solid State Phys.* **2** (1969), p. 229.
- [15] S. R. Elliott, *The Physics and Chemistry of Solids*, John Wiley & Sons Ltd., Chichester (1998).
- [16] D. T. Cromer and J. B. Mann, *Acta Crystallogr.* **A24** (1968), p. 321.
- [17] P. J. Durham, J. B. Pendry and C. H. Hodges, *Comput. Phys. Commun.* **25** (1982), p. 193.
- [18] C. A. Ashley and S. Doniach, *Phys. Rev. B* **11** (1975), p. 1279.
- [19] P. A. Lee and J. B. Pendry, *Phys. Rev. B* **11** (1975), p. 2795.
- [20] E. A. Stern, *Phys. Rev. B* **10** (1974), p. 3027.
- [21] D. E. Sayers, E. A. Stern and F. W. Lytle, *Phys. Rev. Lett.* **27** (1971), p. 1204.
- [22] S. J. Gurman, N. Binsted and I. Ross, *J. Phys. C: Solid State Phys.* **17** (1984), p. 143.
- [23] S. J. Gurman, N. Binsted and I. Ross, *J. Phys. C: Solid State Phys.* **19** (1986), p. 1845.

Chapter 3 – Experimental

3.1 Introduction

This section describes the procedure of conducting experiments and the process of data reduction for each technique. It also covers the production of neutrons at a spallation source and X-rays at a synchrotron source.

3.2 Production of neutrons at the ISIS pulsed neutron source

The neutron scattering data presented here were all collected at the ISIS facility at the Rutherford Appleton Laboratory, UK. Neutron production at ISIS starts with H^- ions, which are accelerated to 70 MeV in a LINAC. The ions are stripped of their electrons by a thin sheet of alumina before entry into a proton synchrotron. The protons are accelerated to 800 MeV and bunches are extracted from the synchrotron 50 times per second to produce a proton beam current of approximately 200 μA . No further acceleration is applied to the protons at this stage but there are a series of magnets along the extracted beam pipe that ensure the protons remain in bunches and do not go off course. The 800 MeV protons collide with a tantalum target. Each incident proton yields about 15 neutrons along with a significant amount of γ radiation. The neutrons are expelled from the target in all directions. The target sits in a heavily shielded container that has 18 radial beam ports to various instruments. Only neutrons that head towards these ports can be used. The neutrons are too energetic to be useful in a diffraction experiment at this point so, before entering the beam ports, the neutrons pass through a moderator. In order to lose energy, the neutrons are required to undergo inelastic collisions with the moderator material. The energy transferred from the neutron to the moderator is maximised when the neutron interact with nuclei of similar mass. The moderator is, therefore, composed of a hydrogen-rich material, such as liquid methane at ~ 110 K. If the neutrons were to stay in the moderator for a long time, the neutrons would reach thermal equilibrium with the methane. However, the neutrons are transient and some pass through without interaction while others undergo one or multiple scattering events before exiting the moderator. The neutron energy distribution, after moderation, becomes broadened and is characterised by a Maxwell-Boltzmann distribution. At ISIS, time-of-flight (TOF) measurements are made, the

details of which are discussed later; suffice to say that the neutron detectors not only measure number of neutrons arriving, but also the time the neutron has taken to arrive (to determine its energy). In this regime it is undesirable to allow the pulse to become too broad because this could allow the slowest neutrons from one pulse to arrive at a detector at the same time as neutrons from the next pulse. This is called frame overlap and results in spurious peaks in the experimental data. By making the moderator reservoir small the neutrons are under-moderated, leaving many high energy neutrons in the beam, but resulting in a narrower pulse. A simulation of the neutron beam profile is shown in Figure 3.1.

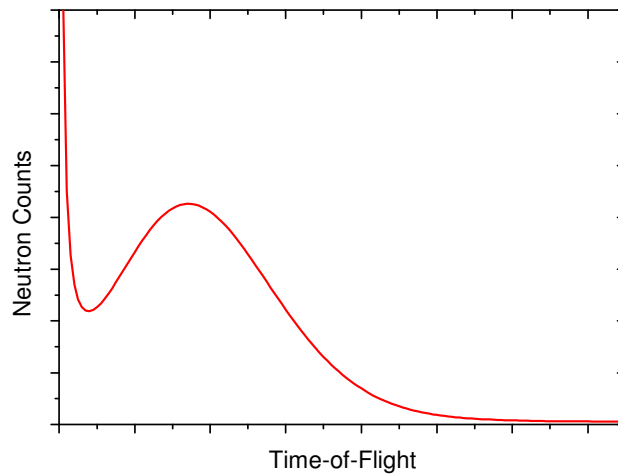


Figure 3.1: Simulated, post-moderated neutron flux.

Before reaching the sample the neutrons may encounter choppers. These rotating devices are designed to block the neutron beam for some fraction of each revolution. When the protons hit the target, the choppers are initially in a closed position to cut out the “gamma flash” and the very fast, epithermal neutrons. They then move to an open position to allow a certain window of neutron energies to pass through before moving to a closed position in time for the next target impact. The chopper revolution speed can be tuned to open different energy windows.

The pulsed nature of ISIS allows time-of-flight (TOF) measurements to be performed. The length of the path taken by the neutron from the moderator to the detector, *via* the sample, can be measured; the time it takes for a neutron to cover that distance is

dependent on the kinetic energy of the neutron. During a TOF measurement, the detectors record the scattered neutron intensity as a function of time. The time can be converted to neutron wavelength by Equation 3.1:

$$t = \frac{m_n}{h} L\lambda \quad 3.1$$

where t is the neutron arrival time, m_n is the neutron rest mass, h is Planck's constant and L is total path length. It can be seen from the definition of Q in Equation 2.5, that if a detector has a fixed angular position, and measures a range of wavelengths over time, it also measures a range of Q over time. This allows a higher maximum Q value to be obtained compared to the scattering of a monochromatic probe.

3.3 Processing experimental neutron diffraction data

The neutron diffraction data presented here were collected on the General Materials (GEM) diffractometer at ISIS [1]. The samples were prepared as solid glass rods, which were attached to the provided sample holder and placed directly in the neutron beam at the focus of the detector array (see Figure 3.2). Samples were typically measured for ~8 hrs to ensure that the data was of appropriate statistical quality.

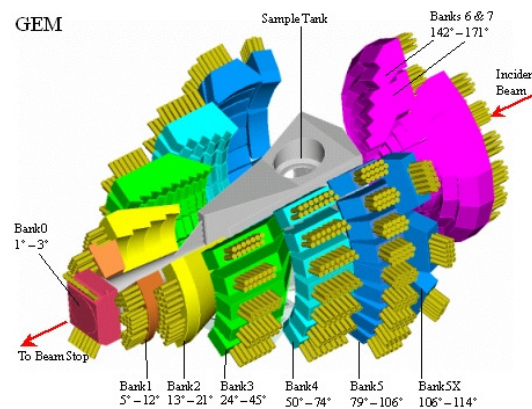


Figure 3.2: 3D representation of GEM showing the large detector array and the sample loading position in the top of the sample tank.

GEM has 7270 $\text{ZnS}/^6\text{Li}$ scintillator detectors arranged in 8 banks covering an angular range of 1.2-171.4 deg. The detector array covers an area of 7.3 m², which corresponds to a solid angle of 3.86 steradians. The variation in detector efficiency is

~0.1 % over a 24 hour period. The primary beam path is 17 m and has two disc choppers that select neutron wavelengths in the range of 0.05-3.40 Å and prevent frame overlap complexities, described earlier. GEM also has a 50 Hz nemonic chopper, which can be used to remove very high energy neutrons, but this is typically deactivated for studies of amorphous materials because it cannot move out of the beam quickly enough and increases the minimum neutron wavelength available in the experiment, thus reducing Q_{max} [1].

The raw data collected on GEM is in the form of counts as a function of arrival time for each detector. The data reduction and processing can be broken down into distinct sections, which are necessary to obtain a normalised interference function from the raw data.

1. Detector dead-time correction
2. Normalisation to the incident flux
3. Background subtraction for sample environment
4. Calibration to vanadium scattering profile
5. Attenuation and multiple scattering corrections
6. Self scattering and the Placzek inelasticity correction
7. Merge individual detector banks

These steps are done using the program *Gudrun* [2] such that the actual process is “hidden” from the user. This section offers a qualitative explanation of each step, and references are given where additional information may be required. *Gudrun* supersedes the obsolete *ATLAS* analysis suite [3], however, the *ATLAS* manual contains useful information about each of the following steps.

Detector dead-time correction

Detectors are always “dead” for a short time after a neutron event has occurred. This corresponds to the lag time between the event and when the event is recorded. In a neutron experiment this dead-time is in the range 0.1-10 µs depending on the type of detector being used and the set-up. The dead-time correction is usually of the order of a few percent and can readily be calculated [2]. In practice the dead-time correction is complicated by the data acquisition electronics configuration. Due to the large number of detectors involved, an encoder is used to deal with a sub-set of detectors and the

encoder dead-time should be considered in the correction. Furthermore, the encoder is only capable of dealing with one event at a time so all the detectors in the encoder's sub-set are dead when one detector fires.

Normalisation to the incident flux

The next step is to divide the dead-time corrected intensity by the monitor counts. A low efficiency monitor detector is placed in the neutron beam before the sample and is used to remove fluctuations due to variations in moderator temperature and proton beam steering. On GEM a thin vanadium foil is placed in the incident beam and the scattered neutron intensity is monitored by shielded detectors [1].

Background subtraction for sample environment

In addition to measuring the samples, it is also necessary to measure the scattering from the empty instrument, which is corrected for dead-time, normalised to the monitor counts and subtracted from the sample profile. In an experiment where the sample is in the form of a powder, it is typical to pack the sample in to a vanadium can. In this instance, it is necessary to collect data for an empty can to be subtracted from the sample data. In this study, only solid self supporting samples were measured and a vanadium can was not used.

Calibration to vanadium scattering profile

A vanadium rod is measured as part of the diffraction experiment. The neutron scattering from vanadium is almost completely incoherent, allowing its differential cross-section to be estimated with reasonable accuracy. The sample data is divided by the smoothed vanadium data such that an absolute scale is obtained.

Attenuation and multiple scattering corrections

The attenuation correction has been discussed in detail for different sample and scattering geometries in various places [4, 5]. The method employed by *Gudrun* for the multiple scattering and attenuation correction is that reported by Soper and Egelstaff [6] for an isotropic sample with cylindrical geometry. The attenuation factors depend only on the sample geometry and the total neutron cross-section, which can be calculated exactly within the static approximation. *Gudrun* also includes an azimuthal correction to account for the cylindrical geometry of the sample since the

detectors are not distributed with cylindrical symmetry. The multiple scattering can never be evaluated with a high degree of accuracy because it requires detailed information about the sample structure and dynamics. Instead, the multiple scattering correction is estimated based on the measured total transmission cross-section and the assumption that the scattering is isotropic at all neutron energies. This is called the isotropic approximation, which is generally accepted for samples that scatter less than 20% of the incident beam.

Self scattering and the Placzek inelasticity correction

Once these corrections have been completed the Q -space data oscillates about the self scattering level ($\sum_i c_i \overline{b_i^2}$). The inelasticity correction represents the difference between the static approximation and the measured differential cross-section. Placzek [7] showed that, for nuclei more massive than the neutron, the correction becomes independent of the detailed dynamics of the structure. Placzek's theory was later extended by Powles [8] to accommodate TOF measurements. The overall inelasticity correction tends to be small and is subtracted from the experimental data. In terms of data analysis, the self scattering and Placzek corrections are combined into the factor $I_S(Q)$, produced by a program called *PLATOM* [3].

$$I_S(Q) = \sum_i c_i \overline{b_i^2} [1 - P_i(\theta, \mu_i, \overline{K}, f, \varepsilon(E), \phi(E))] \quad 3.2$$

where c_i and b_i take their usual meanings. P_i is the Placzek correction for the i^{th} atom in the sample, where θ is half the scattering angle, μ_i is the ratio of the mass of the i^{th} atom to that of the neutron, \overline{K} is the average kinetic energy per atom (depends on the sample temperature), f is the scattered to total flight path ratio, $\varepsilon(E)$ is the energy-dependent detector efficiency and $\phi(E)$ is the energy-dependent neutron flux. Figure 3.3 shows how the effect of the Placzek correction is isolated to the low Q region of $I_S(Q)$.

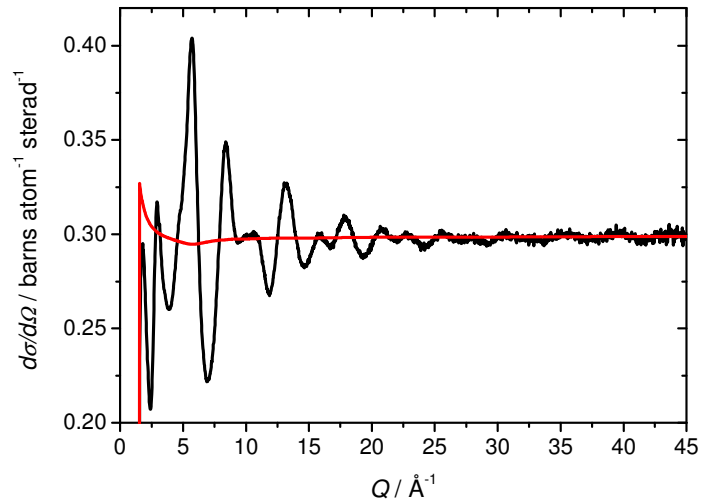


Figure 3.3: Neutron differential scattering cross-section (black) from GEM detector bank 5 and $I_S(Q)$ (red).

Merge individual detector banks

The output from *Gudrun* is typically in the form of the individual detector banks shown in Figure 3.2 (labelled 0-7). $I_S(Q)$ is calculated for each scattering angle and each bank is scaled such that the high Q region oscillates about $I_S(Q)$ as shown in Figure 3.3. In order to produce an $i(Q)$ over the whole Q range it is necessary to manually merge the banks together. This is done on a statistical basis since *Gudrun* also outputs an error for each data point, which comes directly from the number of counts received per channel (the error being \sqrt{N} for a channel with N counts). Figure 3.4 shows the data from each bank.

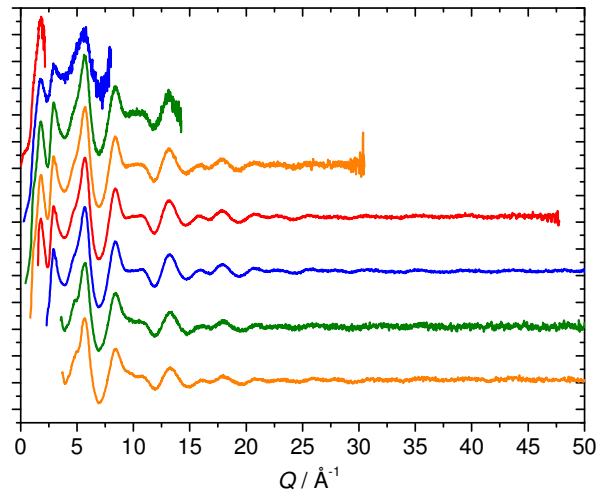


Figure 3.4: Unscaled $d\sigma/d\Omega$ for GEM detector banks 0 through 7 (top to bottom).

3.4 Production of X-rays at the Synchrotron Radiation Source

The X-ray diffraction and X-ray absorption data presented in this study were collected at the Synchrotron Radiation Source (SRS) at Daresbury Laboratory, UK. The X-rays are produced by the continuous acceleration of relativistic electrons in magnetic fields. The radiation is emitted tangentially to the electron's curved path.

The SRS consists of a LINAC, which accelerates electrons, produced by a hot wire cathode, up to 12 MeV. These electrons are injected into a booster ring and are further accelerated to 600 MeV. From the booster ring they are placed in the storage ring itself, having a diameter of 96 m, and are accelerated to a working energy of 2 GeV. In normal operation, 150 bunches of electrons circulate the storage ring at 500 MHz. The storage ring consists of a series of bending magnets and straight sections. The bending magnets have a field strength of 1.2 T. The synchrotron photons are emitted as the electrons are subject to the magnet's field and have a characteristic wavelength of $\sim 3.9 \text{ \AA}$ (see Figure 3.5).

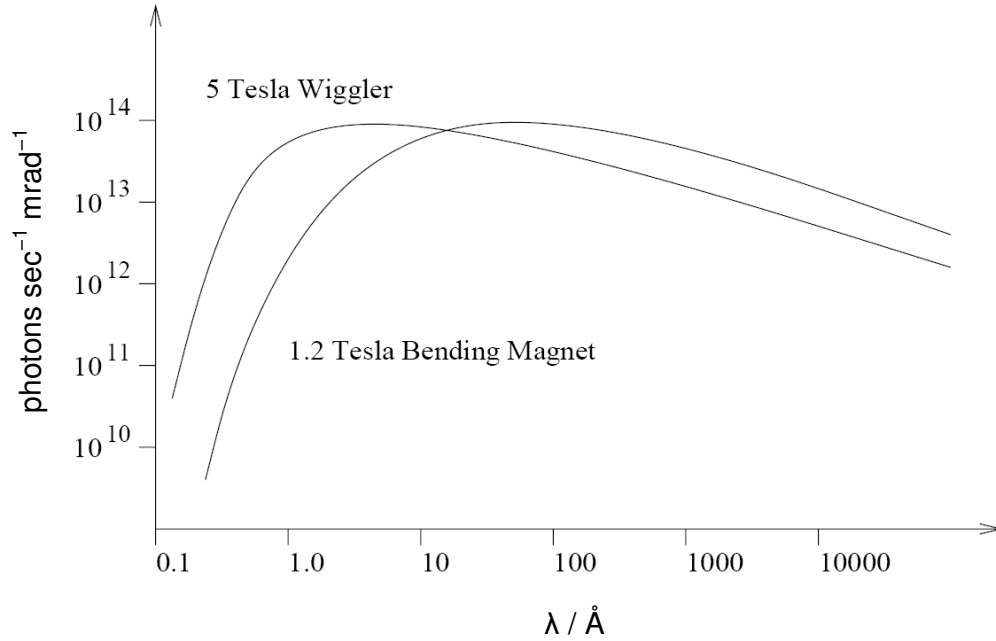


Figure 3.5: Comparison of a bending magnet and wiggler wavelength spectrum [9].

In order to increase the range of wavelengths available, some of the straight sections are replaced with insertion devices (ID), which consist of an array of magnets to produce a periodic field, inducing transverse acceleration on the electrons. There are two types of IDs that are used to produce forward-directed synchrotron radiation. The first is a wiggler, where the strength and period of the magnetic field is not tuned to the frequency of the radiation produced. These can be considered as a series of bending magnets placed close together and results in a broad energy distribution. By way of example, the SRS has a 5 T wiggler insertion device, which has a characteristic wavelength of $\sim 0.9 \text{ \AA}$ (see Figure 3.5). The radiation intensity scales with the number of magnetic poles in the wiggler. The second type of ID is the undulator, where the radiation produced cause sympathetic, resonant oscillations in other electrons, resulting in a relatively narrow energy distribution. In this case the radiation intensity scales with the square of the number of poles in the undulator. A dimensionless parameter, K , is used to characterise IDs.

$$K = \frac{eBd_u}{\pi m_e c} \quad 3.3$$

where e is the electron charge, B is the magnetic field strength, d_u is the distance between two consecutive poles, m_e is the electron mass and c is the speed of light. An ID with $K < 1$ is an undulator and with $K > 1$ is a wiggler. It should be noted that IDs are not essential to the operation of the synchrotron. The entire electron path is kept under ultra-high vacuum to prevent degradation of the bunches by air scattering.

3.5 Processing of experimental X-ray diffraction data

The X-ray diffraction data were collected on station 9.1 at the SRS. Station 9.1 has a diffractometer set to record in theta-two theta geometry (see Figure 3.6). The sample holders were aluminium disks of thickness 0.5 mm. The samples were ground into a fine powder and packed into a 15×5 mm rectangular cut-out in the sample holder. The powder was held in place by a thin layer of Kapton on the front and back faces of the holder.

Station 9.1 is situated 15 m from a 5 T superconducting wiggler [10]. The incident radiation wavelength is selected in the range of 0.4-1.7 Å by a Si(111) double crystal monochromator with 0.1 mdeg resolution. A thin Kapton foil is placed in the beam before the sample so that a monitor spectrum can be collected in a detector perpendicular to the primary beam path, as shown in Figure 3.6. Various slits and jaws are used to collimate the beam, but have been omitted from the diagram for clarity.

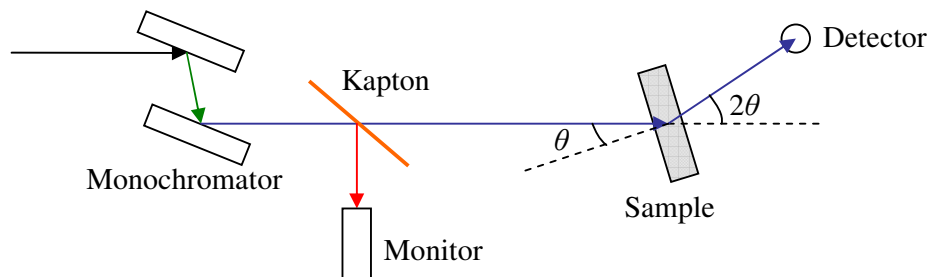


Figure 3.6: Schematic diagram of experimental set-up at SRS station 9.1 in theta-two theta geometry.

The primary beam goes on to interact with the sample and the scattered intensity is collected by a NaI/Tl scintillation detector [10], which scans over an angular range of 1.6-120.0 deg in steps of 0.2 deg. In a typical scan the detector integration time of 8 s was used at each step and the high angle region ($2\theta \geq 28.0$ deg) was scanned twice to

improve the intrinsic reduction in scattered intensity at high angle resulting from the atomic form factor.

In order to obtain useful information from X-ray diffraction data, a series of corrections must be performed. These corrections arise from the following:

1. Normalisation to incident flux
2. Background subtraction for sample environment
3. X-ray beam polarisation
4. Scattering volume variation
5. Compton scattering
6. Sample absorption
7. Self scattering
8. Isolation of the interatomic scattering signal

These steps were performed using software written “in-house”, predominantly in *MATLAB*. An explanation of each step is given here, with references where additional information may be required.

Normalisation to incident flux

This step in the data processing accounts for the temporal variation in incident X-ray flux and allows for the varying collection time for each detector angle. This is done by dividing the data by the monitor count obtained from a fixed detector placed before the sample.

Background subtraction for sample environment

It is necessary to take into account the background scattering due to the sample container, surrounding air and equipment. This is done by performing a scan over the same range as the diffraction experiment on an empty sample holder. In some instances it is necessary to scale the background subtraction to account for the difference in attenuation of the sample and air.

Polarisation factors

The intensity of the diffracted beam is dependent upon the polarisation of the incident X-ray beam. The correction is defined thusly:

$$I_p(\theta) \propto \frac{I_n(\theta)}{P_{\perp} + P_{\parallel} \cos^2(2\theta)} \quad 3.4$$

where $I_p(\theta)$ is the polarisation corrected intensity, $I_n(\theta)$ is the normalised and background subtracted intensity, P_{\perp} and P_{\parallel} are the fraction of perpendicular and parallel polarised X-rays (perpendicular and parallel to the plane of scattering) in the beam, respectively. These parameters are source dependent; for the powder diffractometer on Station 9.1 at the SRS the incident X-ray beam is approximately 90% perpendicularly polarised. This is only an approximation because these factors also depend on the number of reflections in the monochromator, each of which would increase the proportion of parallel polarised X-rays [9].

Sample volume variation

The volume of sample illuminated by the X-ray beam changes as the sample is rotated through theta during a theta-two theta measurement. Given that the sides of the samples are flat and parallel, the correction for sample rotation is given by the following simple expression:

$$I_v(\theta) = \frac{I_p(\theta) \cos \theta}{t} \quad 3.5$$

where $I_v(\theta)$ is the volume corrected intensity, θ is the angle of the sample rotation (corresponding to half the scattering angle) and t is the thickness of the sample. This correction would not be necessary in the case where the sample container's symmetry is such that there is no change in sample volume with scattering angle, *e.g.* a cylinder orientated with its axis on the diffractometer axis of rotation.

Compton scattering

A correction is made for the inelastic contribution to the scattering intensity. This tends to be small, but becomes increasingly more significant at larger scattering angles. The form of the Compton scattering correction for each atom type, $I_i^C(Q)$, is different depending on the atomic number, Z .

- For $Z \leq 20$:

$$I_i^C(Q) = \left[Z - \frac{f_i^2}{Z} \right] \{1 - A(\exp(-Bs) - \exp(-Cs))\} \quad 3.6$$

- For $Z > 20$:

$$I_i^C(Q) = Z \left[1 - \frac{A}{(1+Bs)^C} \right] \quad 3.7$$

The values of A , B and C are tabulated in [11] for $Z \leq 20$ and in [12] for $Z > 20$. The independent variable $s = Q/4\pi$. The Compton scattering correction, $I_{Comp}(Q)$, for the sample is given by the concentration weighted sum of the individual $I_i^C(Q)$:

$$I_{Comp}(Q) = \sum_i c_i I_i^C(Q) \quad 3.8$$

Self scattering

In X-ray diffraction the self scattering results primarily from the finite size of the electron cloud in the atom. As noted earlier, a drop off in scattered intensity is observed as the scattering angle is increased and is described by the X-ray form factor, $f(Q)$. The self scattering is given by:

$$I_{Self}(Q) = \sum_i c_i \overline{f_i^2(Q)} \quad 3.9$$

Sample absorption

The attenuation of the X-ray beam by the sample has an angular dependence, which, for a flat faced sample, is characterised by the exponential described in Equation 3.10:

$$I_{abs}(\theta) = \exp \left[-\frac{\mu t}{\cos(\theta)} \right] \quad 3.10$$

where μ is the linear mass absorption coefficient and t is the thickness of the sample. Values of the X-ray total cross-section, $\sigma = \mu/\rho$, for different X-ray energies are tabulated [13] for each atom type and μt can be determined by the concentration weighted sum:

$$\mu = \rho_s t \sum_i c_i \left(\frac{\mu}{\rho} \right)_i \quad 3.11$$

where ρ_s is the sample number density and c_i is the concentration of the i^{th} atom type.

Isolation of the interatomic scattering signal

Equation 3.12 is used to produce the X-ray interference function, $i(Q)$. Unlike neutron diffraction, there is no X-ray equivalent of vanadium and it is not possible to directly calibrate the X-ray scattering to a known absolute level. Instead, the corrections are all done together such that the data can be scaled to oscillate about zero. θ can easily be converted to Q via Equation 2.5, such that $I_v(\theta)$ and $I_{abs}(\theta)$ become $I_v(Q)$ and $I_{abs}(Q)$ respectively.

$$\frac{i(Q)}{f_e^2(Q)} = \frac{SI_v(Q)I_{abs}(Q) - (AI_{Comp}(Q) + I_{Self}(Q))}{f_e^2(Q)} \quad 3.12$$

where $f_e^2(Q)$ is the sharpening function defined earlier. The parameter A can be varied but should be kept as close to unity as possible and S is an arbitrary scaling constant that allows $i(Q)/f_e^2(Q)$ to oscillate about zero as required by Equation 2.31. The corrections to achieve $i(Q)$ are shown graphically in Figure 3.7.

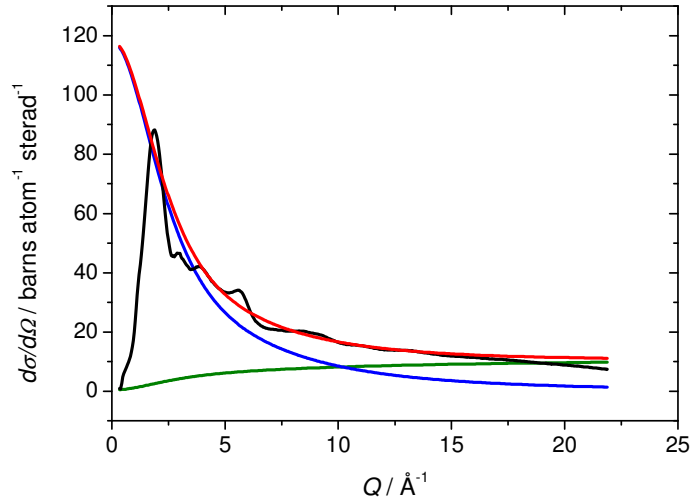


Figure 3.7: $I_{Comp}(Q)$ (green), $I_{Self}(Q)$ (blue). The experimental diffraction data (black), $I_s(Q)I_{abs}(Q)$, has been scaled, by adjusting S , to oscillate about the sum $I_{Comp}(Q)+I_{Self}(Q)$ (red). In this case A has been set to unity.

It is sometimes necessary to fit a polynomial to the high Q region of $i(Q)/f_e^2(Q)$, where a drop-off is observed (see Figure 3.8). This is probably due to the sample not lying exactly at the centre of the diffractometer axis of rotation, causing the sample volume correction to be slightly inaccurate.

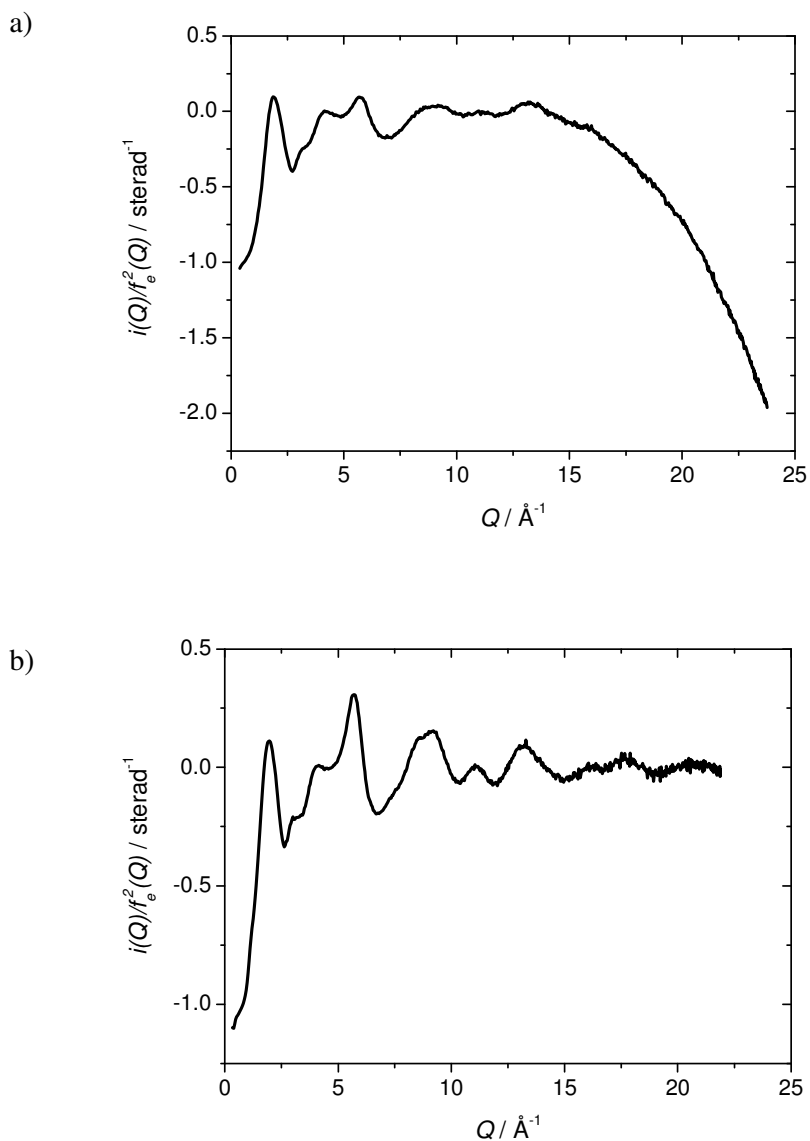


Figure 3.8: $i(Q)/f_e^2(Q)$ a) showing the drop-off at high Q and b) after polynomial correction.

3.6 Analysis of diffraction data

Real space simulation

$T(r)$ exhibits peaks, which correspond to interatomic distances between pairs of atoms and the number of atoms at that distance. In a crystalline sample the peaks tend to be well separated and can be fitted with relative ease. In disordered materials, the peaks become “blurred” and begin to overlap and it becomes necessary to deconvolve the contributions from each atomic pair to yield structural information. $T(r)$ is modelled using the pair function, $p_{ij}(Q)$:

$$p_{ij}(Q) = \frac{N_{ij} w_{ij}(Q) \sin(QR_{ij})}{c_j QR_{ij}} \exp\left[\frac{-Q^2 \sigma_{ij}^2}{2}\right] \quad 3.13$$

where N_{ij} , R_{ij} and σ_{ij} are the coordination number, atomic separation and disorder parameter (*i.e.* a measure of the thermal and static disorder) respectively of atom type i in relation to atom type j . The weighting factors, $w_{ij}(Q)$, are probe-dependent quantities and the X-ray weighting factor, $w_{ij}^X(Q)$, is given by Equation 3.14:

$$w_{ij}^X(Q) = \frac{(2 - \delta_{ij}) c_i c_j f_i(Q) f_j(Q)}{f_e^2(Q)} \quad 3.14$$

while the neutron weighting factor, $w_{ij}^N(Q)$, is constant in Q and may be labelled simply as w_{ij}^N and is given by Equation 3.15:

$$w_{ij}^N(Q) = w_{ij}^N = (2 - \delta_{ij}) c_i c_j b_i b_j \quad 3.15$$

In equations 3.14 and 3.15 δ_{ij} is the Kronecker delta function (*i.e.* $\delta_{ij} = 1$ for $i = j$ or $\delta_{ij} = 0$ otherwise) and c_{ij} , b_{ij} , $f_{ij}(Q)$ and $f_e^2(Q)$ take their usual meanings.

Individual $p_{ij}(Q)$ for each atom pair can be summed and Fourier transformed for comparison with $T(r)$. The advantage of simulating $T(r)$ in this way is that the Fourier transform is the same for both the data and the fit, negating the effects of the component peak function, $P_{ij}^\bullet(r)$ (see Equation 2.21), provided that the same Q range is used. The values of N_{ij} , R_{ij} and σ_{ij} are varied to obtain a better fit to the experimental data.

It should be noted that various real space functions exist (*e.g.* $T(r)$, $D(r)$, $g(r)$, $J(r)$, *etc.*). However, $T(r)$ is used in this case because the peak width distribution and broadening associated with the Fourier transform is most symmetric for this function. This validates the use of $p_{ij}(Q)$, which gives a symmetric Gaussian-like profile upon Fourier transform.

Reverse Monte Carlo modelling

The theory of Reverse Monte Carlo (RMC) modelling is covered in extensive detail by McGreevy and Pusztai [14], McGreevy [15] and Evrard and Pusztai [16] as well as a variety of other places. Therefore, the description of RMC given here is limited to qualitative explanation. The program used to perform RMC on amorphous materials is *RMCA* [17] originally written in *FORTRAN*.

The ultimate yield of RMC is a 3D model that is one possible arrangement of atoms that describes the experimentally measured scattering pattern. This is achieved by randomly moving virtual atoms around inside a box and after each move the derived scattering pattern is compared to experimental data and the move is either accepted or rejected. The box size is defined by the number of atoms and the number density of the sample. Periodic boundary conditions are imposed, meaning that if an atom moves out of the box on one side it moves back into the box on the opposite side.

Constraints are applied to RMC that represent existing knowledge of the structure (*e.g.* density, coordination environment, atomic radii). By ensuring that RMC adheres to these constraints it is much more likely that the resulting model agrees quantitatively with the experimental data.

RMC is started with an initial configuration of N atoms that represents the real configuration of the sample. The positions of the N atoms may be chosen randomly or be based on a known crystal structure or some previous model/simulation. Based on this configuration it is possible to calculate the radial distribution function, $g(r)$, for the sample:

$$g(r) = \frac{n(r)}{4\pi r^2 \Delta r \rho} \quad 3.16$$

where $n(r)$ is the number of atoms at a distance between r and $r+\Delta r$ from the central atom, averaged over all atoms as centres and ρ is the number density. The configuration size should be chosen such that there are no correlations across the box (*i.e.* for a box of side length L , $g(r > L/2) = 1$).

The Fourier inversion of $g(r)$ yields the modelled structure factor, $S^M(Q)$, which can be compared to the experimentally obtained structure factor, $S^E(Q)$. The parameter that RMC attempts to minimise is χ_n^2 which is the difference between the $S^M(Q)$ and $S^E(Q)$ after n moves:

$$\chi_n^2 = \sum_i \frac{(S_{n,i}^M(Q) - S_i^E(Q))^2}{\sigma_i^2(Q)} \quad 3.17$$

where $\sigma_i(Q)$ is the standard deviation of the normally distributed statistical error at the i^{th} point in Q . It is possible to fit more than one data set at a time with RMC and in this case the separate χ_n^2 are summed. A new particle configuration is created (*i.e.* $n \rightarrow n+1$) by moving one atom at random and χ_{n+1}^2 is calculated. If $\chi_{n+1}^2 < \chi_n^2$ then the new move is accepted by default, else if $\chi_{n+1}^2 > \chi_n^2$ then the new move is accepted with probability $\exp[(\chi_n^2 - \chi_{n+1}^2)/2]$, else the move is rejected and the n^{th} configuration is maintained. By accepting moves that do not improve the fit to the data RMC can avoid getting stuck in local minima. Eventually the above procedure reduces χ^2 to an “equilibrium value” corresponding to a global minimum within the parameter space defined by the constraints.

It should be noted that RMC does not produce a unique solution for the structure of amorphous materials. The model produced is simply a configuration of atoms that satisfies the constraints imposed by the user and matches the experimental data to a reasonable degree of accuracy. Therefore, care should be taken when the results of RMC are interpreted and, where possible, should be combined with complimentary analysis methods.

3.7 Processing of experimental X-ray absorption spectroscopy data

The XAS data used in this study were collected on Station 9.3 at the SRS, which was run in transmission mode; depicted schematically in Figure 3.9. Various slits and jaws are used to define the beam size, but have been omitted in the diagram for clarity.

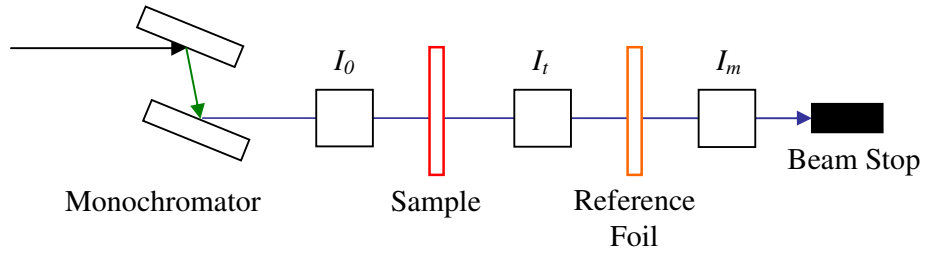


Figure 3.9: Schematic diagram of the XAS experimental set-up in transmission mode.

I_0 , I_t and I_m represent the incident, transmitted and reference ionisation chambers respectively. Provided that the gas mixture is correct, the current measured in each chamber is directly proportional to the X-ray intensity passing through. It can be seen in Figure 3.10 that there is no single gas that covers all energies. It is possible to use a mixture of gasses so that the ionisation chamber performance is optimal for the energy range of interest.

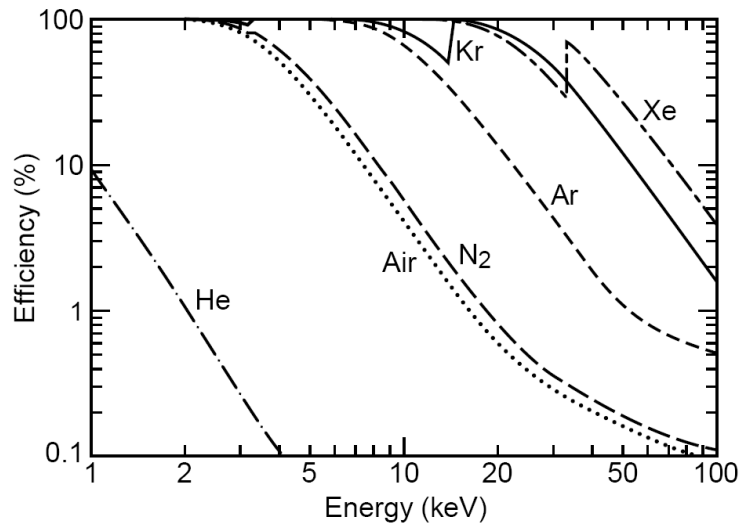


Figure 3.10: Efficiency of a 10 cm long gas ionisation chamber as a function of energy for different gasses at normal pressure [18].

The raw data is collected in terms of the monochromator angle and the current captured in each of the ionisation chambers. The sample absorption can be obtained directly from the ionisation current measurements:

$$I_t = I_0 e^{-\mu} \quad 3.18$$

where I_0 and I_t are the incident and transmitted ionisation currents and μ is the sample attenuation. Equation 3.18 can be rearranged to give:

$$\mu = \ln\left(\frac{I_0}{I_t}\right) \quad 3.19$$

The monochromator is a single crystal, usually silicon, cut along one of its crystallographic planes (typically 111 or 220 for silicon). From the Miller indices (hkl), the interplanar spacing, d , can be calculated:

$$d = \frac{a}{\sqrt{h^2 + k^2 + l^2}} \quad 3.20$$

where a is the lattice parameter (5.43 Å for silicon). This result makes it possible to convert the monochromator angle to X-ray wavelength *via* the Bragg equation:

$$\lambda = 2d \sin(\theta) \quad 3.21$$

where θ is the monochromator angle. A characteristic of Bragg scattering is that the primary beam can be “poisoned” by the presence of harmonic modes such that it is not genuinely monochromatic. Harmonic modes are undesirable in XAS measurements and can be reduced by a process called harmonic rejection. This can be most easily understood in terms of a double crystal monochromator as shown in Figure 3.9. In order to get the most flux of the desired energy, the crystals should be set parallel and both rotate through the same angle as the energy is varied. Instead they are detuned slightly such that one is set at angle θ and the other at $\theta + \Delta\theta$, where $\Delta\theta$ is a very small angular increment. This has the effect of reducing the contribution from the higher order harmonics.

The data reduction of XAS data can be broken down into the following distinct parts:

1. Monochromator angle to energy conversion and calibration
2. Pre-edge background subtraction

3. Post-edge background subtraction and normalisation

Monochromator angle to energy conversion and calibration

Although the change in monochromator angle can be measured accurately (within the time scale of one measurement), it is not possible to find the monochromator's absolute orientation, due to two main factors:

1. The monochromator crystal is subject to thermal expansion/contraction over time, changing its position.
2. The path that the X-ray beam takes upon leaving the synchrotron varies after each refill cycle, and therefore is not incident on the same area of the monochromator each time.

This is overcome by recording a constant reference spectrum simultaneously with the sample. The reference ionisation current is collected such that I_r and I_m can be used to find the foil absorption spectrum. This study has concentrated on the role of the metal ions in a glass matrix and the reference for each measurement was a thin foil of the element under investigation. Metals tend to have a well defined absorption edge that can be compared to tabulated values [18]. The position of the foil edge can then be used to calibrate each scan individually.

At this point the absorption of each sample depends on the amount of material in the beam and the concentration of the absorbing element in the sample. In order to compare different samples it is necessary to put all spectra on a common scale by dividing by an empirical background that simulates the isolated atom absorption as shown in Figure 2.5 for tin.

Pre-edge background subtraction

The pre-edge is the region before the sharp increase in absorption that corresponds to core electron emission. The pre-edge region tends to be flat and is fitted with a straight line, which is subtracted across the whole range of the spectrum.

Post-edge background subtraction and normalisation

The post edge starts from a position on the absorption edge where the gradient is maximised. This point is nominally labelled E_0 and corresponds to the energy at which

the core electron is liberated, but has zero kinetic energy in the continuum (*i.e.* E_0 corresponds to the binding energy of the electron). When undertaking XANES analysis only, it is typical to fit this region with a second or third order polynomial, which fits through the post-edge oscillations. The polynomial is evaluated from E_0 up to the largest energy value in the XANES spectrum. EXAFS analysis requires a much more careful approach to the post-edge subtraction and it is usual to fit a spline from E_0 up to the end of the extended spectrum. The spline is a series of third order polynomials that are tied at certain, user specified points, called knots. At each knot the polynomials must satisfy a set of boundary conditions, with respect to their neighbours:

1. the polynomial values must be equal
2. the first derivative must be equal
3. the second derivative must be equal

These conditions ensure that the spline is continuous across its fitted range and does not introduce any discontinuities. The knots can be moved around until a satisfactory fit is obtained. A good fit is determined by visual inspection of the resulting $k^3\chi(k)$ and the Fourier transform of $k^3\chi(k)$. $k^3\chi(k)$ should oscillate about zero and the Fourier transform should be relatively flat at low r . Failure to produce a satisfactory background leads to the presence of non-physical features in the spectrum. Regardless of whether a polynomial or spline has been used for the post-edge, Equation 2.34 is used to normalise the data to produce $\chi(E)$, where the derived pre- and post-edge corrections simulate $\mu_0(E)$.

3.8 Analysis of EXAFS data

Once the EXAFS oscillations have been isolated it is necessary to extract structural information by iteratively refining the theoretical EXAFS spectra in order to obtain the best fit to the experimental data. This process is done with a program called *EXCURV98*, which is available on the Daresbury Laboratory computing system [19]. The refinement procedure, in *EXCURV98*, is based on least squares minimisation in k -space under constrained conditions.

EXCURV98 uses the fast curved wave theory, developed by Gurman, Binsted and Ross [20, 21] as described earlier and requires the user to define a series of shells, which correspond to layers of atoms about the absorbing atom. In a disordered material, the shells are typically broad. The shells are simulated using Equation 2.37, where the phase-shifts are calculated based on the types of atoms in each shell. It is possible to fit the data with multiple shells. Generally the user should aim to get a satisfactory fit with the minimum number of shells, since the addition of further shells can lead to solutions in false minima [22]. It is possible to evaluate how well the theoretical, $\chi_t(k)$, fits the experimental, $\chi_e(k)$, using the fit index, F :

$$F = \frac{\sum_i [k_i^3 \chi_e(k_i) - k_i^3 \chi_t(k_i)]^2}{100N_p} \quad 3.22$$

where N_p is the total number of data points. F is the quantity that is refined by the optimisation routine in *EXCURV98*. An extra shell should only be considered as significant if it causes a substantial reduction in F . This is not easy to quantify, but a rigorous assessment can be applied, called the reduced chi-squared test. First the number of independent points, N_{ind} , should be determined:

$$N_{ind} = \frac{2 \cdot \Delta k \cdot \Delta r}{\pi} + 1 \quad 3.23$$

where Δk and Δr are the respective ranges in k - and r -space over which the data is fitted. It should be noted that the total number of parameters, N_{pars} , should not be more than N_{ind} . The reduced chi-squared, RCS , can be defined:

$$RCS = \frac{\sum_i [k_i^3 \chi_e(k_i) - k_i^3 \chi_t(k_i)]^2}{N_{ind} - N_{pars}} \quad 3.24$$

When a further shell is added, N_{pars} changes and RCS should be recalculated. If RCS does not become smaller, then the addition of the extra shell may not be justified. Equation 3.24 assumes that each point has the same error and is therefore not correct for very noisy data.

Correlations exist between certain parameters and it is possible to produce contour maps showing the relationship between two variables. The contours denote lines of constant F and if these lines are close together, then the minimum is well defined. Maps can be used to estimate the errors in the fitted parameters by seeing how much they could change and not affect F . This does not include measuring errors, background subtraction errors or systematic errors and can therefore only be treated as the minimum error.

The value of $A(k)$ is determined by fitting a crystalline sample of known structure and correspond to the proportion of photons that undergo an EXAFS type of event in the sample. Typical values are in the range of 0.1 to unity. The value of $A(k)$ was fixed and used throughout the analysis of the experimental data.

The experimental data is input in the form of k vs. $k^3\chi(k)$ such that the oscillations at high k are amplified. It is these oscillations that contain information about the interatomic distances and should, therefore, be more heavily weighted. This is the origin of k^3 in the numerator of equations 3.22 and 3.24. In Equation 2.37 there are three free parameters per shell, namely R , N and σ , which are the central atom to shell radius, number of atoms in the shell and width of the shell, respectively. These parameters are varied by *EXCURV98* to obtain the best fit to the data by minimising F .

3.9 References

- [1] A. C. Hannon, *Nucl. Instrum. Methods Phys. Res., Sect. A* **551** (2005), p. 88.
- [2] S. E. McLain, D. T. Bowron, A. C. Hannon and A. K. Soper, GUDRUN, A computer program developed for analysis of neutron diffraction data., (2006).
- [3] A. C. Hannon, W. S. Howells and A. K. Soper, *Inst. Phys. Conf. Ser.* **107** (1990), p. 193.
- [4] A. P. Kendig and C. J. Pings, *J. Appl. Phys.* **36** (1965), p. 1692.
- [5] H. H. Paalman and C. J. Pings, *J. Appl. Phys.* **33** (1962), p. 2635.
- [6] A. K. Soper and P. A. Egelstaff, *Nucl. Instrum. Methods* **178** (1980), p. 415.
- [7] G. Placzek, *Phys. Rev.* **86** (1952), p. 377.
- [8] J. G. Powles, *Mol. Phys.* **26** (1973), p. 1325
- [9] D. T. Bowron, A Study of Rare Earth Doped Silicate and Phosphate Glasses, *Department of Physics, University of Kent, Canterbury* (1994).
- [10] G. Bushnell-Wye and R. J. Cernik, *Rev. Sci. Instrum.* **63** (1992), p. 999.
- [11] F. Hajdu, *Acta Crystallogr.* **A27** (1971), p. 73.
- [12] G. Palinkas, *Acta Crystallogr.* **A29** (1973), p. 10.
- [13] W. H. McMaster, N. K. Del Grande, J. H. Mallett and J. H. Hubbell, Compilation of X-ray cross sections, *Lawrence Livermore National Laboratory Report*, (1969).
- [14] R. L. McGreevy and L. Pusztai, *Mol. Simul.* **1** (1988), p. 359.
- [15] R. L. McGreevy, *J. Phys.: Condens. Matter* **13** (2001), R877.
- [16] G. Evrard and L. Pusztai, *J. Phys.: Condens. Matter* **17** (2005), S1.
- [17] R. L. McGreevy, M. A. Howe and J. D. Wicks, RMCA: A general purpose reverse Monte Carlo code, *NFL Studsvik Internal Report*, Studsvik Neutron Research Laboratory (1993).
- [18] A. Tompson and D. Vaughan, X-ray Data Booklet, Lawrence Berkeley National Laboratory, Berkeley (2001).
- [19] S. Tomic, B. G. Searle, A. Wander, N. M. Harrison, A. J. Dent, J. F. W. Mosselmanns and J. E. Inglesfield, New tools for the Analysis of EXAFS: The DL_EXCURV Package, *CCLRC Technical Report*, CCLRC (2005).
- [20] S. J. Gurman, N. Binsted and I. Ross, *J. Phys. C: Solid State Phys.* **17** (1984), p. 143.

[21] S. J. Gurman, N. Binsted and I. Ross, *J. Phys. C: Solid State Phys.* **19** (1986), p. 1845.

[22] R. W. Joyner, K. J. Martin and P. Meehan, *J. Phys. C: Solid State Phys.* **20** (1987), p. 4005.

Chapter 4 – Computational Developments: *NXFit*

This chapter introduces a program that was developed as part of this project. *NXFit* is capable of optimising structural parameters and simultaneously fitting X-ray and neutron diffraction data.

4.1 Introduction

Diffraction has become an important tool for determining the atomic scale structure of matter and advanced instrumentation has made the collection of high quality data possible. However, analysis and interpretation of that data can still be difficult, particularly where the material has a complicated structure and/or multiple components. There are various approaches to fitting data from crystalline materials, the most common of which is the Rietveld refinement [1], which can be applied to both X-ray and neutron diffraction data. Fitting diffraction data relating to amorphous materials is more subjective and different processes have been formulated. One method is to prepare atomistic models to simulate the experimentally obtained diffraction pattern. These models are usually produced by Reverse Monte Carlo (RMC) [2, 3], Molecular Dynamics (MD) [4, 5] or, more recently, by Empirical Potential Structure Refinement (EPSR) [6, 7].

This work presents another method, whereby the experimental data is represented in real space and a series of peaks are fitted to simulate correlations between atom pairs. This has been demonstrated as a viable technique for both crystalline [8] and disordered materials [9]. Furthermore, it is possible to simultaneously fit X-ray and neutron data of the same sample using the same structural parameters. For example, in a multicomponent glass, where there is a large number of overlapping correlations, this feature is particularly useful because the relative weighting to each atomic pair is different depending on the radiation used. X-rays interact with the electrons in the atoms and preferentially pick out high-Z atomic species, whereas the neutrons interact with the nuclei in the sample and the scattering strength does not exhibit a monotonic trend with atomic number. The program presented here automates the fitting

procedure and is capable of co-fitting X-ray and neutron scattering data from crystalline or amorphous materials. It should be noted that the program is as yet untested on crystalline materials.

4.2 Technical

NXFit has a graphical user interface (GUI) so that the user can set the operating parameters easily. The program is written in *MATLAB* but has been compiled to run along side the *MATLAB* Compiler Runtime (MCR) on an end users' machine. *NXFit* uses the Nelder-Mead (also known as the downhill or amoeba) method, which is a commonly used nonlinear optimisation algorithm, to vary a set of "best guess" parameters to achieve a fit to experimentally derived data. The scheme was developed by Nelder and Mead [10] and is a numerical method for minimising an objective function in an N dimensional space. The method uses the concept of a simplex, which is a polytope with $N+1$ vertices. For example, in one dimension the polytope is a line segment, in two dimensions it is a triangle and in three dimensions it is a tetrahedron. As the dimensionality of the problem increases the polytope becomes more complex. The Nelder-Mead simplex method finds, approximately, the solution to a problem with N variables when the objective function varies smoothly. In the case of *NXFit*, the objective function is the combination of peaks that are being used to simulate the experimental $T(r)$ and the value of interest to the optimisation routine is the least squares fit index, FI . The value of FI is determined at each vertex of the polytope. In the simplest case, the point that yields the worst FI value is rejected and a new test point is developed by reflecting the simplex through the centroid of the remaining N points. If the new point is much better, then the simplex stretches out exponentially along this line. However, if the new point is not much better than the original test point, then the algorithm assumes that it is stepping across a valley and shrinks the simplex towards the best point. In order to clarify, the Nelder-Mead algorithm is outlined below in seven steps, which are conducted in order.

0. Setup

Define the $N+1$ vertices of the initial simplex as follows:

The primary vertex, v_{N+1} , has N coordinates that define its position in the parameter space. The coordinates correspond to the initial guess. This set of

coordinates are then duplicated N times, with the exception that, at each duplication, the n^{th} parameter, p_n , for $1 \leq n \leq N$, is shifted by +5%, thus defining a distinct position for the n^{th} vertex, v_n . The positions, in parameter space, of the N new vertices lie on orthogonal axes with the v_{N+1} being the point at the intersection of lines of $-\infty \leq p_n \leq \infty$ for each v_n . If $p_n = 0$ then a standard offset of 0.00025 is applied.

1. Order

Sort the results according to the values of FI at each of the $N+1$ vertices: $FI(x_1) \leq FI(x_2) \leq \dots \leq FI(x_{N+1})$, where x_1 and x_{N+1} are points in parameter space whose coordinates correspond a set of structural parameters that give the best and worst value of FI respectively (*i.e.* the current best and worst point).

2. Calculate

Determine x_0 , the centre of gravity of all points except x_{N+1} .

3. Reflect

Compute the reflected point, $x_r = x_0 + \alpha(x_0 - x_{N+1})$.

IF $FI(x_1) \leq FI(x_r) \leq FI(x_N)$ then create a new simplex by replacing x_{N+1} with x_r and go to step 1.

ELSE go to step 4

4. Expand

IF $FI(x_r) < FI(x_1)$ then compute the expanded point, $x_e = x_0 + \gamma(x_0 - x_{N+1})$.

IF $FI(x_e) < FI(x_r)$ then create a new simplex by replacing the worse point, x_{N+1} , with x_e and go to step 1.

ELSE create a new simplex by replacing the worse point x_{N+1} with x_r and go to step 1.

ELSE continue to step 5.

5. Contract

At this point it is certain that $FI(x_r) \geq FI(x_N)$. Compute the contracted point, $x_c = x_{N+1} + \rho(x_0 - x_{N+1})$.

IF $FI(x_c) \leq FI(x_{N+1})$ then create a new simplex by replacing x_{N+1} with x_c and go to step 1.

ELSE go to step 6.

6. Reduce

For all but the best point, replace the points $x_i = x_l + \sigma(x_i - x_l)$ for i in the range $2 \leq i \leq N+1$ and go to step 1.

The parameters α , γ , ρ and σ are the reflection, expansion, contraction and shrink coefficients respectively. The values used are $\alpha = 1$, $\gamma = 2$, $\rho = 0.5$ and $\sigma = 0.5$ and are set within the built-in *MATLAB* function *fminsearch*.

An occasional problem of multidimensional optimisation algorithms is that they can become stuck in local minima due to the collapse of the simplex. The Nelder-Mead method is not immune in this regard [11]. The standard approach to handling this is to arrange a new simplex starting from the current best parameter values. There are alternatives to Nelder-Mead, such as the flexible polyhedron method, but this tends to make a large number of unnecessary steps in regions of little interest and takes longer to converge on a solution.

The Nelder-Mead routine alone does not have any capacity to include constraints, but in order to fit experimental diffraction data it is necessary to constrain the fitting parameters to avoid non-physical solutions. Upper and lower bounds are implemented with a wrapper function called *fminsearchcon*[†], which sits on top of *fminsearch* and uses a sinusoidal transformation of the parameters:

$$y(i) = LB(i) + \frac{1}{2}[UB(i) - LB(i)][\sin(z(i)) + 1] \quad 4.1$$

where $y(i)$ is the real parameter, $z(i)$ is the transformed parameter and $UB(i)$ and $LB(i)$ are the upper and lower bound of $y(i)$ respectively. It is evident from Equation 4.1 that

[†] *fminsearchcon* was created by John D'Errico (*MATLAB* user community) and can be freely downloaded from the *MATLAB* file exchange, <http://www.mathworks.co.uk/matlabcentral/fileexchange/>.

$z(i)$ is unconstrained and can take any value $-\infty \leq z(i) \leq +\infty$, while $y(i)$ is restricted to the range $LB(i) \leq y(i) \leq UB(i)$ upon transformation. This is illustrated graphically in Figure 4.1.

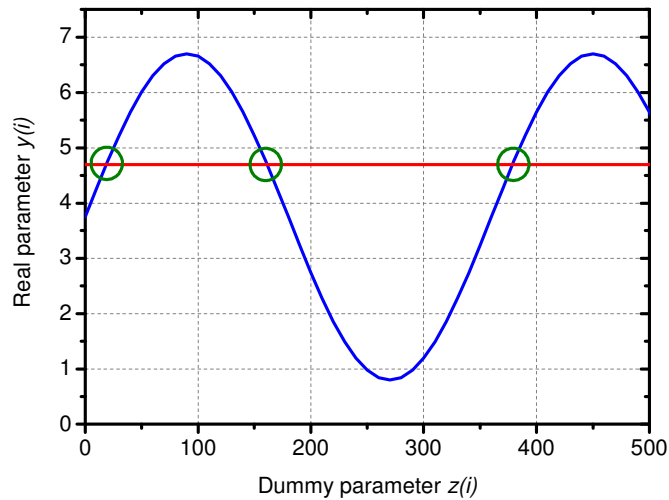


Figure 4.1: Graphical representation of the sinusoidal parameter transform. Here three distinct values of $z(i)$ are highlighted, each giving the same real parameter, $y(i)$.

4.3 Preparing to run *NXFit*

In order to run *NXFit*, the user is required to set up a series of files to supply information about the sample and the diffraction measurement as described below. It should be noted that the headings that appear in the following figures should be omitted in the actual files.

Input data files

The data should be Fourier transformed, as per equations 2.24 and 2.31 depending on the radiation being used and should be saved in a two column text file.

r	$T(r)$
0.00	0
0.02	0.013227836
0.04	0.029622524
0.06	0.051921274
0.08	0.082051709
1.00	0.12084574
...	...

Figure 4.2: Example input data file.

Sample composition files

The file required for neutron diffraction data to describe the sample is simple. The different atom types are distinguished by their atomic number, Z , in the left-most column. Z is used for identification purposes only and is not used by *NXFit*. The second column is the coherent scattering length in units of fm from tables (*e.g.* [12]) and the third column is the atomic fraction of each atom type.

Z	b_i	c_i
15	5.13	0.213
20	4.76	0.064
11	3.58	0.085
47	5.922	0.000
8	5.803	0.638

Figure 4.3: Example neutron sample composition file.

In contrast, the X-ray sample description file is more complicated and the information is entered in columns for each atom type. Z is entered in the first row and is again used for identification only. The second row is the atomic fraction of each element. Rows three through eleven contain the parameters that are used to simulate the X-ray scattering factors (see Equation 2.28) and are tabulated in [13] and the *International Tables of Crystallography*. Rows twelve to fourteen contain the parameters that are used to simulate the Compton scattering (see equations 3.6 and 3.7) [14, 15]. The Compton parameters are not used by *NXFit* and can be set to zero.

<i>Z</i>	15	20	11	47	8
<i>c_i</i>	0.2128	0.0638	0.0851	0.0000	0.6383
<i>a1</i>	6.4345	15.6348	3.2565	19.2808	3.0485
<i>a2</i>	4.1791	7.9518	3.9362	16.6885	2.2868
<i>a3</i>	1.7800	8.4372	1.3998	4.80450	1.5463
<i>a4</i>	1.4908	0.8537	1.0032	1.04630	0.867
<i>b1</i>	1.9067	-0.0074	2.6671	0.6446	13.2771
<i>b2</i>	27.157	0.6089	6.1153	7.47260	5.7011
<i>b3</i>	0.5260	10.3116	0.2001	24.6605	0.3239
<i>b4</i>	68.1645	25.9905	14.039	99.8156	32.9089
<i>c</i>	1.1149	-14.875	0.4040	5.1790	0.2508
<i>A</i>	0.5136	0.50934	0.45524	1.0549	0.37033
<i>B</i>	1.10729	0.9172	1.22322	0.6874	1.22426
<i>C</i>	14.635	14.7943	21.7068	1.8487	25.4902

Figure 4.4: Example X-ray sample composition file.

Input parameters and bounds file

A five column file must be supplied to set the starting parameters in *NXFit*. Each row describes an individual atomic pair correlation, and hence a peak in real space. The first three columns contain the interatomic separation (in Å), number of atoms at that distance and disorder parameter (in Å) from left to right corresponding to R_{ij} , N_{ij} and σ_{ij} respectively in Equation 3.13. The next two columns define the atomic pair and the numbers refer to the position of that atom in the sample composition file. In the case of the example in Figure 4.5, the first correlation is at 1.48 Å with 1.9 lots of atom type 5 around each atom type 1 with a Gaussian distribution width of 0.04 Å. The input parameter file can be extended to include as many correlations as are necessary.

<i>R_{ij}</i>	<i>N_{ij}</i>	<i>σ_{ij}</i>	<i>atom i</i>	<i>atom j</i>
1.48	1.9	0.04	1	5
1.60	1.9	0.04	1	5
2.33	4.0	0.10	3	5
2.35	5.0	0.13	2	5
2.51	4.0	0.08	5	5
...

Figure 4.5: Example input parameter file.

Each parameter has a constraint which is defined in the bounds file. The three columns below correspond to the first three columns in the input parameter file and

there must be a constraint for each parameter. By way of example, the first parameter in Figure 4.5 is 1.48 Å, which can vary by ± 0.03 Å according to the file in Figure 4.6. Parameters can be fixed by setting the corresponding bound to zero.

ΔR_{ij}	ΔN_{ij}	$\Delta \delta_{ij}$
0.03	0.2	0.02
0.03	0.2	0.02
0.05	0.2	0.03
0.05	0.2	0.03
0.05	0.4	0.03
...

Figure 4.6: Example bound constrains file.

4.4 Running NXFit

Once *NXFit* has been started, the user is presented with the main GUI, as shown in Figure 4.7. The various widgets can be used to control *NXFit*. In the first instance the user must select the type of data being fitted with the check boxes in the appropriate section. Once the data type has been selected the user can fill in the necessary information and select the appropriate input files using the *Browse* buttons.

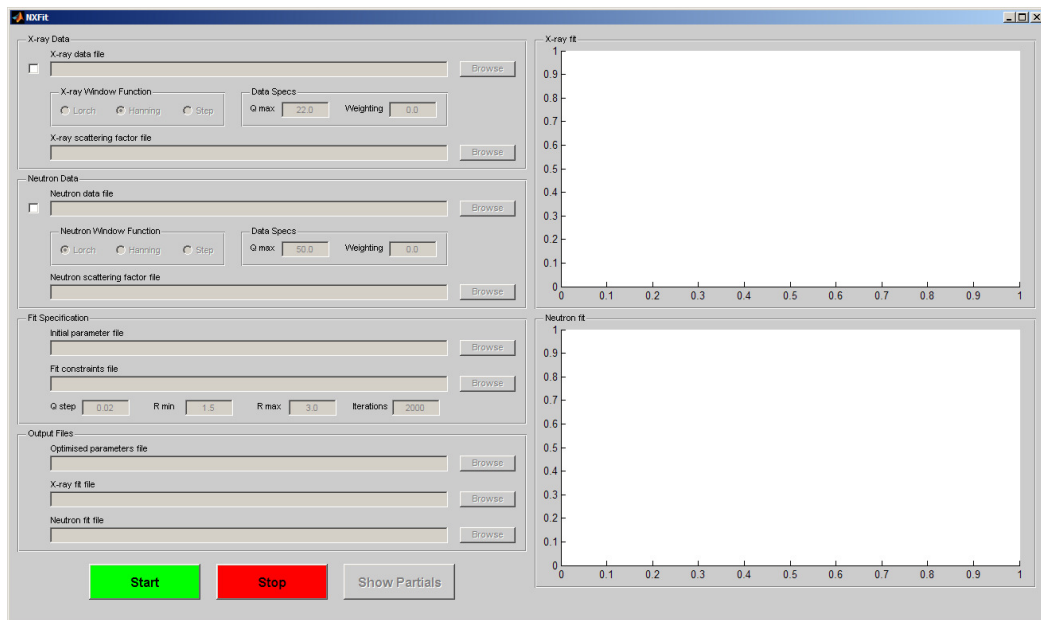


Figure 4.7: Initial view of the main *NXFit* GUI.

For each type of data the user must specify which type of window function was used when the data was Fourier transformed. It should be noted that the step function is equivalent to using no modification function at all (*i.e.* $M(Q) = 1$ over the whole extent of Q). The user should also enter the maximum Q value that was used in the original Fourier transform. These two factors are essential for producing a fit of the correct form and with the correct real space resolution. A discussion of the effect that these have on the data is given in Chapter 2. The user can only change the weighting if both X-ray and neutrons are being co-fitted else it is set to unity. When co-fitting the relative weighting of each data set can be changed. Nominally it may be preferable to give the X-ray and neutron data an even weighting (*i.e.* 0.5:0.5). However, it may be sensible to reweight the data if, for example, there are certain features that are more prominent in one set than the other or if one set of data is more reliable. Some issues surrounding the weighting of the experimental data in the current version of *NXFit* are discussed in more detail later (Section 4.5)

In addition to the sample-specific information, the user must also enter some details about the fit. The *Qstep* parameter controls the spacing between consecutive Q points over the range that $p_{ij}(Q)$ is being simulated. It may be prudent to use a *Qstep* value identical to that of the original data, but using a larger *Qstep* allows for faster execution of the routine. The parameters *Rmin* and *Rmax* define the region of interest over which *FI* is determined. The user also has the option to change the number of iterations used by the routine. The output files can be selected with the use of the *Browse* buttons or can be typed in by hand. If the file does not exist it will be created upon completion of the routine.

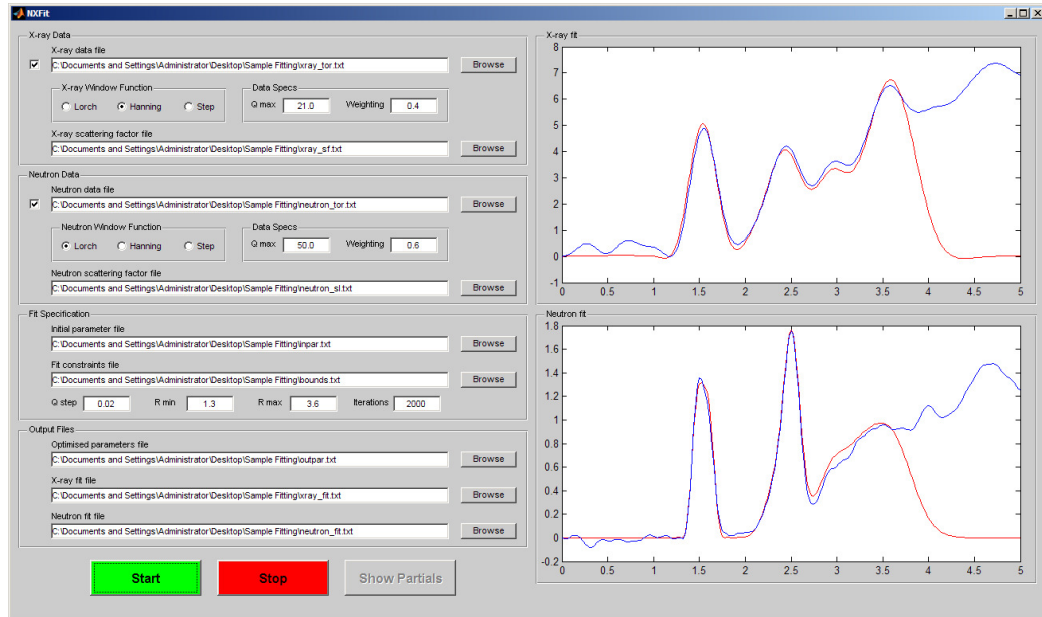


Figure 4.8: NXFit GUI with all fields filled out. Plots on the right show the experimental data (blue) and the simulated fit (red) and is updated in real-time.

Once the routine is started, the plots on the right hand side of the GUI (see Figure 4.8) are updated after each iteration to reflect the current state of the optimisation. The user can halt execution at anytime by pressing the *Stop* button. Once the process has finished successfully or has been stopped by the user, the *Show Partial* button becomes active and can be used to display the individual correlations as shown in Figure 4.9.

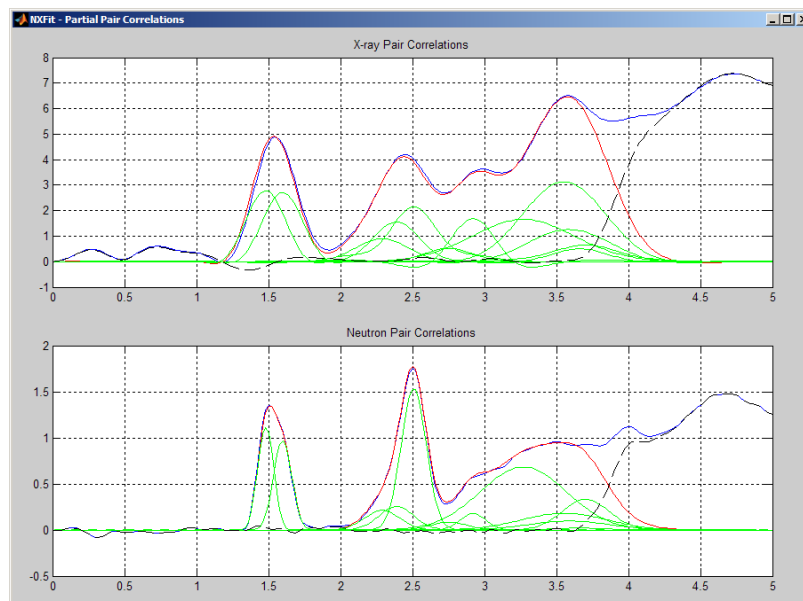


Figure 4.9: The individual partial correlations functions (green) are shown along with the fit (red), the data (blue) and the residual (black dashed).

4.5 Future improvements

There are a number of areas where *NXFit* could be improved to bring it in line with the user-friendly applications that people are accustomed to using on a day-to-day basis. Currently, preparing to run *NXFit* is relatively complicated and requires that the user gathers information from a variety of sources, including papers and/or tables that may not be easily accessible. In future versions of the program it would be an advantage to have the various tables integrated so that the parameters relating to X-ray form factors and neutron scattering lengths are looked up automatically. In this way the user would only need to provide basic information about the sample composition, which would be generic for both X-ray and neutron data.

The current parameters being used to produce the X-ray form factors [13] are old and in some cases may be inaccurate. New parameters are available, which simulate the form factor more accurately up to a maximum Q value of $\sim 75 \text{ \AA}^{-1}$ [16]. In a future version of *NXFit* it may be wise to use these form factors or even give the user the choice over which parameters are used.

The fitting routine relies on the data and the fit undergoing the same Fourier transformation. Presently the user is required to input the diffraction data in the form

of $T(r)$ (*i.e.* already having been Fourier transformed). This could be problematic if *NXFit* is distributed to a wider user group, where various Fourier transform routines exist. For this reason, future versions of *NXFit* should accept the data in the form of $i(Q)$ and perform the Fourier transform step internally such that it is wholly self-consistent.

When X-ray or neutron data is fitted individually, FI is calculated:

$$FI = \sum_{r=R \min}^{r=R \max} (T_e(r) - T_s(r))^2 \quad 4.2$$

where $T_e(r)$ and $T_s(r)$ is the experimental and simulated total correlation functions respectively. In this case the absolute size of FI is not important because the optimisation routine only looks to reduce this number. A problem occurs when co-fitting is attempted because the X-ray $T(r)$ has different units to the neutron $T(r)$ (see the y-axis in Figure 4.9) by the definitions given in Chapter 2. If a linear combination of the X-ray and neutron FI is used, the neutrons effectively become “down-weighted” such that a user-defined 0.5:0.5 weighting on the GUI does not actually correspond to a true 0.5:0.5 weighting of FI . An attempt to improve this has been made such that FI is derived as per Equation 4.3 for co-fitted data.

$$FI = \sum_{r=R \min}^{r=R \max} \left[w^X \frac{(T_e^X(r) - T_s^X(r))^2}{\overline{T_e^X(r)}} + w^N \frac{(T_e^N(r) - T_s^N(r))^2}{\overline{T_e^N(r)}} \right] \quad 4.3$$

where w^X is the X-ray weighing defined in the GUI and $\overline{T_e^X(r)}$ is the average of $T_e^X(r)$ over the range $Rmin \leq r \leq Rmax$, and similarly for neutrons. The form of FI in Equation 4.3 reduces the effect of down-weighting but does not solve the problem completely. Instead, the problem is more fundamental and relates the way the different types of data are normalised. Equations 2.24 and 2.31 define the Fourier inversion of $i(Q)$ to $T(r)$ for neutrons and X-rays respectively. They are repeated below for easy comparison:

$$T^N(r) = 4\pi\rho^0 r \left(\sum_i c_i \bar{b}_i \right)^2 + \frac{2}{\pi} \int_0^\infty Qi(Q)M(Q) \sin(rQ) dQ \quad 4.4$$

$$T^X(r) = 2\pi^2 \rho^0 r + \int_0^\infty \frac{Qi(Q)}{\left(\sum_i c_i f_i(Q) \right)^2} M(Q) \sin(rQ) dQ \quad 4.5$$

It should be noted that, strictly speaking, the above two equations cannot both describe $T(r)$ because the units are different in both cases, but are defined as such nonetheless (Keen [17] gives a good account of various definitions of the scattering functions). If $a(Q)$ is reintroduced (see Chapter 2) to describe either the neutron scattering length, b , or the X-ray form factor, $f(Q)$, then it can be seen that, with some rearrangement, $T(r)$ can be defined generically:

$$T(r) = 4\pi\rho^0 r + \frac{2}{\pi} \int_0^\infty \frac{Qi(Q)}{\left(\sum_i c_i a_i(Q) \right)^2} M(Q) \sin(rQ) dQ \quad 4.6$$

where the total scattering structure factor, $S(Q)$, is defined thusly [17]:

$$S(Q) - 1 = \frac{i(Q)}{\left(\sum_i c_i a_i(Q) \right)^2} \quad 4.7$$

Figure 4.10 illustrates X-ray and neutron $T(r)$ produced *via* Equation 4.6. A maximum Q value of 20 \AA^{-1} was used in both cases so that the real-space resolution is consistent and direct comparison is easier. It should be noted that this is not a requirement of *NXFit*.

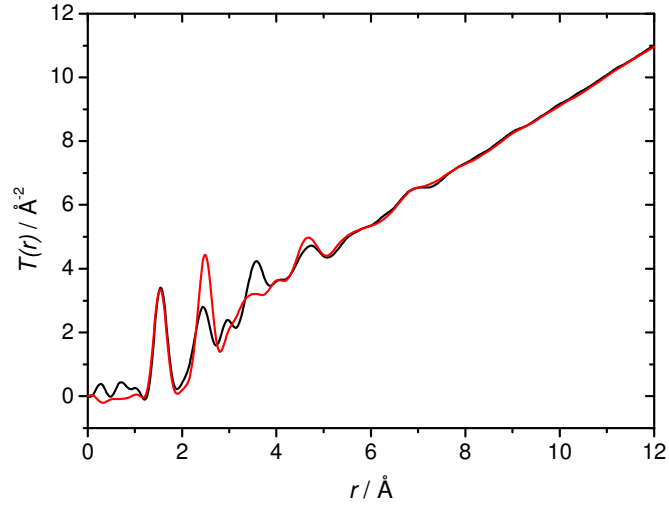


Figure 4.10: An example of $T(r)$ for X-ray (black) and neutron (red) data.

The diffraction data can then be fitted as described in Section 3.6 with the pair-wise correlation weighting factors, $w_{ij}(Q)$, (see equations 3.14 and 3.15 and related text) being defined generically:

$$w_{ij}(Q) = \frac{(2 - \delta_{ij})c_i c_j a_i(Q) a_j(Q)}{\left(\sum_i c_i a_i(Q) \right)^2} \quad 4.8$$

Using this method the X-ray and neutron $T(r)$ have the same units and Equation 4.2 can be used for each data set individually such that the combined FI can be calculated simply as a linear combination of the two:

$$FI = \sum_{r=R_{\min}}^{r=R_{\max}} \left[w^X \left(T_e^X(r) - T_s^X(r) \right)^2 + w^N \left(T_e^N(r) - T_s^N(r) \right)^2 \right] \quad 4.9$$

Presently, *NXFit* does not output errors for each parameter, which is something that should be addressed in the future. A method by which this could be achieved has not been investigated.

4.6 References

- [1] H. Rietveld, *J. Appl. Crystallogr.* **2** (1969), p. 65.
- [2] R. L. McGreevy and L. Pusztai, *Mol. Simul.* **1** (1988), p. 359.
- [3] R. L. McGreevy, *J. Phys.: Condens. Matter* **13** (2001), R877.
- [4] B. J. Alder and T. E. Wainwright, *J. Chem. Phys.* **31** (1959), p. 459.
- [5] A. N. Cormack and Y. Cao, *Molecular Engineering* **6** (1996), p. 183.
- [6] A. K. Soper, *Mol. Phys.* **99** (2001), p. 1503.
- [7] A. K. Soper, *Phys. Rev. B* **72** (2005), 104204.
- [8] A. C. Hannon, E. R. Barney, D. Holland and K. S. Knight, *J. Solid State Chem.* **181** (2008), p. 1087.
- [9] U. Hoppe, D. Stachel and D. Beyer, *Phys. Scr.* **T57** (1995), p. 122.
- [10] J. A. Nelder and R. Mead, *The Computer Journal* **7** (1965), p. 308.
- [11] K. I. M. McKinnon, *Siam Journal on Optimization* **9** (1998), p. 148.
- [12] V. F. Sears, *Neutron News* **3** (1992), p. 26.
- [13] D. T. Cromer and J. B. Mann, *Acta Crystallogr.* **A24** (1968), p. 321.
- [14] F. Hajdu, *Acta Crystallogr.* **A27** (1971), p. 73.
- [15] G. Palinkas, *Acta Crystallogr.* **A29** (1973), p. 10.
- [16] D. Waasmaier and A. Kirfel, *Acta Crystallogr.* **A51** (1995), p. 416.
- [17] D. A. Keen, *J. Appl. Crystallogr.* **34** (2001), p. 172.

Chapter 5 – Calcium Sodium Phosphate: Total Diffraction & RMC

5.1 Introduction

As mentioned previously, the base composition used for all glasses studied was $(\text{P}_2\text{O}_5)_{50}(\text{CaO})_{30}(\text{Na}_2\text{O})_{20}$. It was therefore wise to investigate this particular composition in detail to formulate a good understanding of its structure so that changes induced by adding further modifiers could be determined. X-ray and neutron diffraction data have been collected and analysed by RMC modelling and by fitting peaks in real space. *NXFit* (see Chapter 4) was used to optimise the structural parameters by fitting both data sets simultaneously.

5.2 Experimental

Sample preparation

An 8 mm diameter $(\text{P}_2\text{O}_5)_{50}(\text{CaO})_{30}(\text{Na}_2\text{O})_{20}$ glass rod was prepared by the conventional melt-quench method using NaH_2PO_4 , CaCO_3 , P_2O_5 (BDH, UK). The precursors were weighed out into a 30 ml silica crucible (Saint-Gobain, U.K.), mixed and the crucible loaded into a preheated furnace. The mixture was left at 300 °C for half an hour, raised to 600 °C for a further half hour and finally melted at 1200 °C for one hour. The molten glass was then poured into an 8 mm diameter graphite mould, which had been preheated to 370 °C. The mould was then left to cool slowly to room temperature in order to remove any residual stress.

High Energy X-ray Diffraction

The data were collected on Station 9.1 at the Synchrotron Radiation Source at Daresbury Laboratory, UK. The instrument was set up to collect data in theta-two theta geometry with a 12×1 mm beam of monochromatic ($\lambda = 0.509 \text{ \AA}$, $E = 25.514 \text{ keV}$) X-rays incident on the sample. The sample holders were aluminium disks of thickness 0.5 mm. The glass was ground into a fine powder and was packed into a 15×5 mm rectangular cut-out in the sample holder. The sample was held in place by a

thin (25 μm) layer of Kapton (a polyimide film) on the front and back faces of the holder.

Neutron Diffraction

The data presented here were collected on the GEM diffractometer at the ISIS pulsed neutron facility at the Rutherford Appleton Laboratory, UK [1]. The solid glass rods were mounted on a sample holder and placed directly in the neutron beam. The jaws were set to define a beam size of 40×15 mm at the sample. Time-of-flight data were collected over a large Q -range (up to 50 \AA^{-1}). Vanadium and empty instrument patterns were also measured for normalisation purposes. The program *Gudrun* [2] was used to perform the corrections and data reduction.

5.3 Results

An RMC model was constructed to simulate the structure of the $(\text{P}_2\text{O}_5)_{50}(\text{CaO})_{30}(\text{Na}_2\text{O})_{20}$ glass. The model was assembled with 1128 atoms consistent with the composition (*i.e.* 240 P, 240 BO, 480 NBO, 72 Ca and 96 Na). Coordination constraints and minimum interatomic separations were applied to move the atoms into an initial configuration. The minimum interatomic separations or “cut-offs” are shown in Table 5.1 for each atom pair.

The model was built incrementally by arranging the atoms into sub-structures. The initial configuration was constructed using appropriate constraints. The P and BOs were added first and were arranged into ...-P-BO-P-BO-... chains. NBOs were added randomly and the coordination and angular (triplet) constraints were applied to build PO_4 tetrahedral units. The calcium and sodium atoms were added randomly and moved into positions consistent with their coordination constraints. The coordination and triplet constraints that were applied to define the sub-structures are listed below.

Atomic Pair	Cut-off / Å
P··P	2.75
P-BO	1.48
P-NBO	1.36
P··Ca	3.00
P··Na	3.00
BO··BO	2.20
BO··NBO	2.20
BO··Ca	3.00
BO··Na	3.00
NBO··NBO	2.20
NBO-Ca	2.05
NBO-Na	2.00
Ca··Ca	3.00
Ca··Na	3.00
Na··Na	3.00

Table 5.1: Minimum interatomic separation for each atom pair in the RMC model.

PO₄ tetrahedra

- The number of phosphorus atoms within the range 2.75-3.00 Å of any other phosphorus atoms must be exactly 2.
- The number of BOs within the range 1.375-1.76 Å of any phosphorus atom must be exactly 2 and *vice versa*.
- The number of NBOs within the range 1.29-1.61 Å of any phosphorus atom must be exactly 2.
- The number of phosphorus atoms within the range 1.29-1.61 Å of any NBO must be exactly 1.
- The BO-P-BO, BO-P-NBO and NBO-P-NBO bond angles must all be approximately 109°.

CaO_x polyhedra

- The number of NBOs within the range 2.05-3.00 Å of any calcium atom must be greater than 4.
- The number of BOs within the range of 0.00-3.00 Å of any calcium atom must be exactly 0.

NaO_x polyhedra

- The number of NBOs within the range 2.00-3.00 Å of any sodium atom must be greater than 3.
- The number of BOs within the range of 0.00-3.00 Å of any sodium atom must be exactly 0.

Once these constraints were met to a satisfactory degree (*i.e.* > 98% of atoms obeyed relevant constraints) the model was refined by fitting the experimental data. Effectively, the X-ray and neutron data provide two further constraints on the RMC process. The final RMC model is shown in Figure 5.1 along with the experimental $i(Q)$.

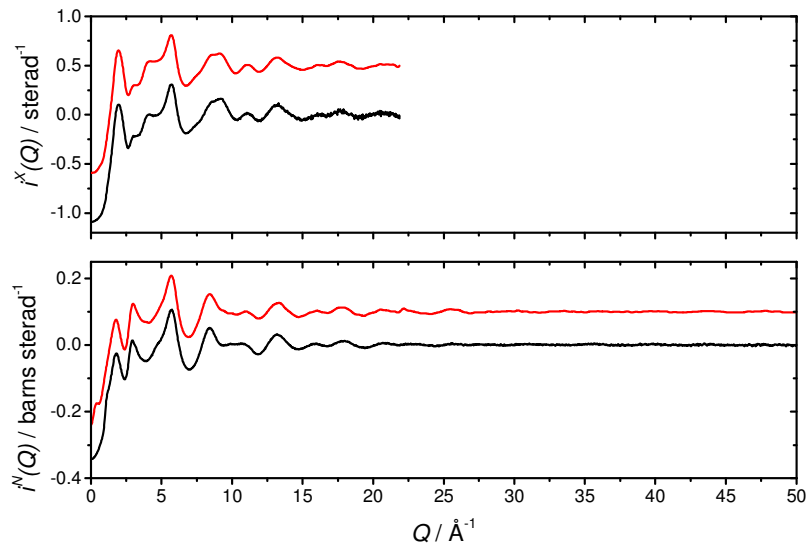


Figure 5.1: X-ray (top) and neutron (bottom) $i(Q)$ (black) and RMC model (red) for $(\text{P}_2\text{O}_5)_{50}(\text{CaO})_{30}(\text{Na}_2\text{O})_{20}$.

Structural parameters can be obtained from the RMC model but it is necessary to specify a range in r over which atoms are counted as neighbours. This can be thought of as defining coordination shells. The lower boundary (r_1) of the first coordination shell is set equal to the cut-offs described earlier and the upper boundary (r_2) is determined by the plateaus in the coordination function, $C_{ij}(r)$, (see Equation 5.1) which describes the number of atom type j between the distances 0 and r from an atom of type i [3].

$$C_{ij}(r) = \int_0^r 4\pi\rho_0 c_j r^2 g_{ij}(r) dr \quad 5.1$$

It should be noted that $C_{ji}(r)$ can be determined by substituting c_i in the place of c_j in Equation 5.1.

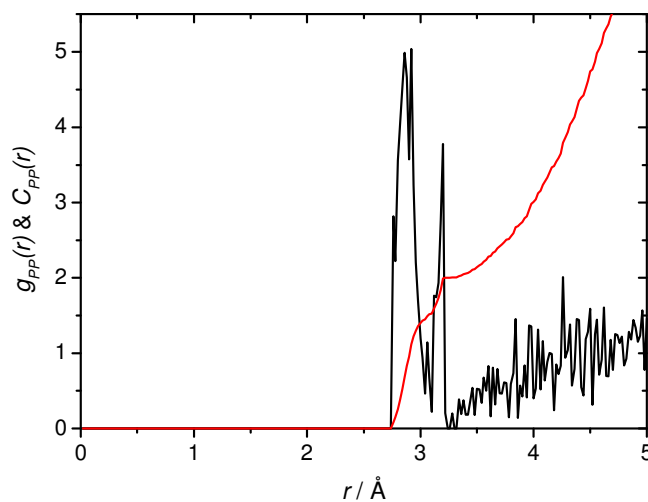


Figure 5.2: $g_{PP}(r)$ (black) and $C_{PP}(r)$ (red) showing a clear plateau in $C_{PP}(r)$ at 3.30 Å, which defines the upper boundary of the first P-P coordination shell.

An example of $C_{ij}(r)$ is shown in Figure 5.2 for the P-P correlation. A plateau is observed at 3.30 Å and defines the upper boundary of the coordination shell. Table 5.2 shows the structural parameters for various atomic pairs and the boundaries of the shells over which the parameters were calculated. N_{ij} is the average coordination number determined by the RMC utility program *Neighbours* and is equal to $C_{ij}(r_2)$. R_{ij} is the mean interatomic separation defined by Equation 5.2.

$$R_{ij} = \frac{\sum_k r_k g_{ij}(r_k)}{\sum_k g_{ij}(r_k)} \quad 5.2$$

where k is all the points in r between and including r_1 and r_2 .

Correlation	$R_{ij} / \text{\AA}$	N_{ij}	Shell boundaries / \AA	
			r_1	r_2
P...P	2.94	2.0	2.75	3.30
P-BO	1.59	2.0	1.48	1.90
P-NBO	1.54	2.0	1.36	1.64
P...Ca	3.42	1.2	3.00	3.84
P...Na	3.44	1.6	3.00	3.80
BO...BO	2.51	1.9	2.20	2.86
BO...NBO	2.50	3.9	2.20	2.84
BO...Ca	4.14	3.5	3.00	5.38
BO...Na	4.00	3.8	3.00	5.12
NBO...NBO	2.46	1.8	2.20	2.74
NBO-Ca	2.45	0.8 (5.5)	2.05	3.00
NBO-Na	2.43	0.8 (4.2)	2.00	2.78
Ca...Ca	3.41	0.7	3.00	3.64
Ca...Na	3.38	1.8	3.00	3.80
Na...Na	3.21	1.0	3.00	3.60

Table 5.2: Structural parameters derived from the RMC model. N_{ij} values shown in parentheses are the coordination numbers given in the opposite sense (*i.e.* N_{ji}).

The X-ray and neutron $T(r)$ are shown in Figure 5.3. The maximum Q values used in the Fourier transform of both the X-ray and neutron $i(Q)$ was 21 \AA^{-1} . The Lorch function was used to modify the neutron and X-ray data during the Fourier transform.

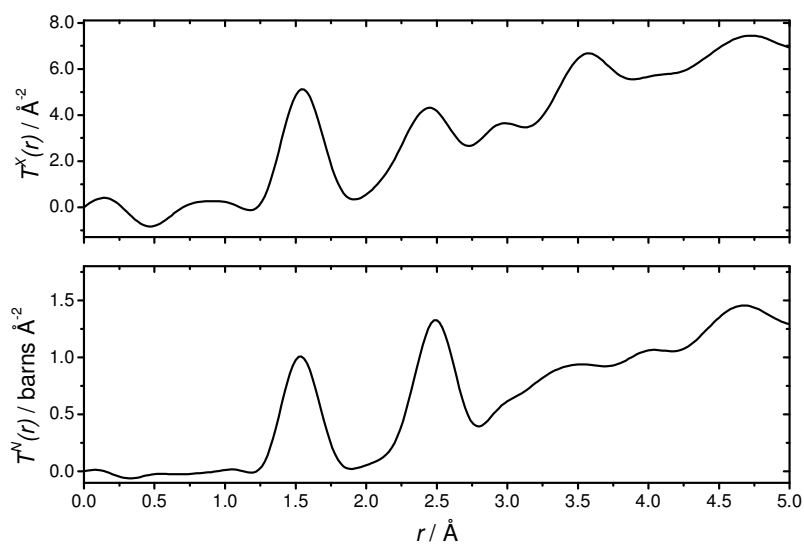


Figure 5.3: $T(r)$ produced by X-ray (top) and neutron (bottom) diffraction for $(\text{P}_2\text{O}_5)_{50}(\text{CaO})_{30}(\text{Na}_2\text{O})_{20}$.

The initial guesses of the structural parameters can be obtained by looking at the literature or using crystallographic databases (*e.g. The Chemical Database Service, Daresbury* [4]). In order to fit these data sets, the parameters given by the RMC model (see Table 5.2) were used as a starting point.

The endemic problem with fitting $T(r)$ is the existence of overlapping correlations at higher r . The goodness-of-fit at any singular point depends on the contribution of each correlation at that point. For this reason it is necessary to use two or three peaks after the last correlation to act as “background fillers”, which do not necessarily yield any useful information. Table 5.3 shows the optimised output structural parameters from *NXFit*, the background filling peaks are identified by the light grey characters.

Correlation	$R / \text{\AA}$ (± 0.02)	N (± 0.2)	$\sigma / \text{\AA}$ (± 0.02)
P-O	1.54	3.8	0.08
Na-O	2.33	4.3	0.12
Ca-O	2.39	6.1	0.12
O··O	2.52	3.9	0.08
P··P	2.88	1.9	0.07
O··O	3.17	5.2	0.22
P··Ca	3.39	3.9	0.30

Table 5.3: Optimised structural parameters output by *NXFit* upon co-fitting X-ray and neutron diffraction data of $(\text{P}_2\text{O}_5)_{50}(\text{CaO})_{30}(\text{Na}_2\text{O})_{20}$.

The final fit produced by the parameters in Table 5.3 is shown in Figure 5.4. The relative magnitudes of the peaks for like correlations shows how the weighting for different atomic pairs varies in X-ray and neutron scattering and exemplifies the strength of using both techniques in combination.

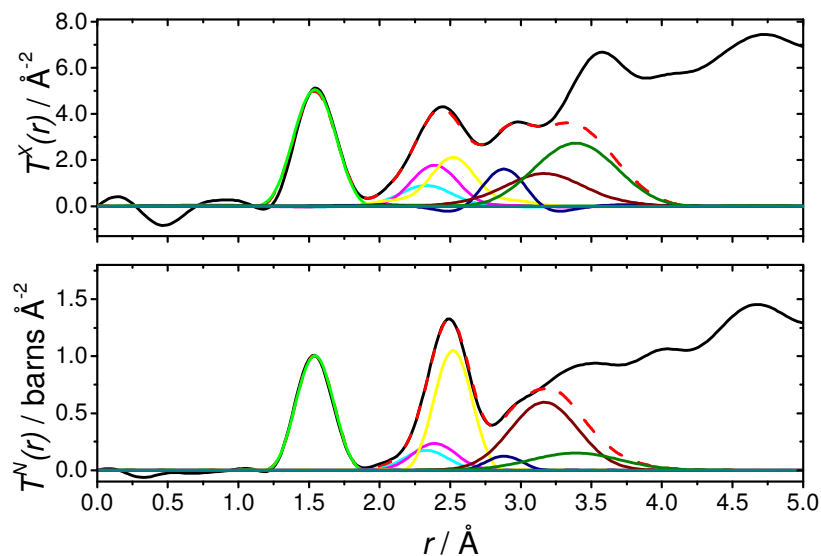


Figure 5.4: Fit (red dashed) to X-ray (top) and neutron (bottom) $T(r)$ (black) produced by refining the input parameters. Correlations from left to right: P-O (green), Na-O (cyan), Ca-O (magenta), O...O (yellow), P...P (navy), O...O (burgundy) and P...Ca (olive).

5.4 Discussion

The sample under investigation here has $[O]/[P] = 3$, such that each phosphorus atom is expected to be coordinated by four oxygen atoms in Q^2 units. The first set of parameters in Table 5.3 correspond to the P-O correlation, which has a coordination equal to four within the error of the measurement. It is possible to further elucidate the P-O peak into contributions from P-NBO and P-BO using the full dynamic range of the neutron diffraction data. Figure 5.5 shows the $T^N(r)$ over the range 1.0-2.0 Å. In this case $i^N(Q)$ has been Fourier transformed using a maximum Q value of 50 \AA^{-1} and no modification has been applied to maximise the real space resolution. The split between the P-NBO and P-BO correlations is clear and these have been fitted using the technique outlined in Chapter 3.

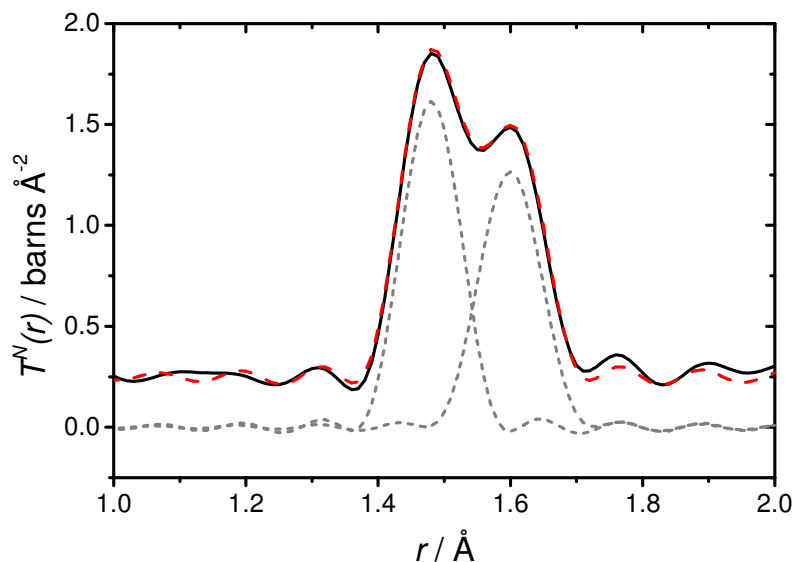


Figure 5.5: $T^N(r)$ highlighting the split in the P-O peak. The contributions are from P-NBO (left) and P-BO (right).

The structural parameters obtained by fitting the P-O contributions are given in Table 5.4. As expected of a metaphosphate structure, the split between P-NBO and P-BO is equal.

Correlation	$R / \text{Å}$ (± 0.01)	N (± 0.1)	$\sigma / \text{Å}$ (± 0.01)
P-NBO	1.48	2.0	0.04
P-BO	1.60	1.8	0.04

Table 5.4: P-NBO and P-BO structural parameters derived from fitting $T^N(r)$.

The next most prominent peak in the X-ray and neutron $T(r)$ is the O-O correlation. On average every oxygen atom is surrounded by four others at a distance of 2.52 Å. Using an average P-O distance of 1.54 Å, the average O-P-O bond angle is calculated as 109.8°, which corresponds well with the tetrahedral angle. Further support is lent to the Q² chain-like structure by the P···P correlation, which shows that each phosphorus atom has 1.9 phosphorus neighbours at a mean distance of 2.88 Å, consistent with the formation of P-O-P linkages. It is then possible to calculate the average P-O-P angle as 138.5°, in good agreement with Hoppe *et al.* [5] and Wetherall *et al.* [6].

The Ca- and Na-O correlations (hereafter referred to generically as M-O) can be characterised by the valence of the metal ion at the centre of the MO_x polyhedra, which is balanced by the nearby NBOs. The amount of valence neutralised by any one NBO (V_{M-O}) depends on the distance (R_{M-O}) it is from the central ion. This dependency was determined empirically by Brese and O’Keeffe [7] and is shown in Equation 5.3.

$$V_{M-O} = \exp\left[\frac{r_{M-O} - R_{M-O}}{0.37}\right] \quad 5.3$$

where r_{M-O} is the bond valence parameter, which is tabulated for various M-anion pairs by Brese and O’Keeffe [7]. The factor of 0.37 in the denominator of the exponential of Equation 5.3 is their so-called “universal” constant.

The Na-O parameters given in Table 5.3 show that each sodium atom is coordinated by 4.3 NBOs with a mean separation of 2.33 Å. Based on these parameters and using $r_{Na-O} = 1.80$ Å in Equation 5.3, the total sodium valence being neutralised by its neighbouring NBOs is 1.03, which corresponds well with the ideal value of 1.00 for a Na^+ ion.

The Ca-O correlations can be justified in a similar way, with each Ca being surrounded by 6.1 NBOs at 2.39 Å. Using Equation 5.3 with $r_{Ca-O} = 1.97$ Å, it can be determined that the total valence neutralised by the NBOs is 1.94, again corresponding well with the ideal value of 2.00 for a Ca^{2+} ion.

The RMC results (see Table 5.2) show that the total NBO-M coordination number is 1.6. This means that 60% of the NBOs are coordinated by two metal atoms on average, and as a result, the MO_x polyhedra are not isolated. This gives rise to $M \cdots M$ correlations, also shown by the RMC. According to the model, 70% of all calcium atoms have another calcium as their second neighbour, 75% have two sodium atoms as second neighbours and the remaining 25% have just one sodium. On average, each sodium has one sodium second neighbour. Isolating these second neighbour contributions is very tricky with total diffraction data due to the aforementioned overlapping correlation problem. It may be feasible to investigate these features further by other techniques such as XAS, NMR and NDIS where possible.

5.5 Conclusions

The structure of $(\text{P}_2\text{O}_5)_{50}(\text{CaO})_{30}(\text{Na}_2\text{O})_{20}$ has been shown to be consistent with previous studies on metaphosphate glasses of similar compositions. The P-O correlations are composed of contributions from P-BO and P-NBO pairs suggesting that each PO_4 tetrahedral unit is connected to two others to form chain-like structures. On average the sodium ions are coordinated by ~ 4 NBOs while the calcium ions tend to coordinate with ~ 6 NBOs. These structural parameters are in good agreement with other studies of similar materials [6, 8-11] and with bond valence calculations. Over half of the NBOs in the sample are shared between adjacent MO_x polyhedra giving rise to M \cdots M correlations in $T(r)$.

5.6 References

- [1] A. C. Hannon, *Nucl. Instrum. Methods Phys. Res., Sect. A* **551** (2005), p. 88.
- [2] S. E. McLain, D. T. Bowron, A. C. Hannon and A. K. Soper, GUDRUN, A computer program developed for analysis of neutron diffraction data., (2006).
- [3] D. A. Keen, *J. Appl. Crystallogr.* **34** (2001), p. 172.
- [4] D. A. Fletcher, R. F. McMeeking and D. Parkin, *J. Chem. Inf. Comput. Sci.* **36** (1996), p. 746.
- [5] U. Hoppe, R. K. Brow, D. Ilieva, P. Jóvári and A. C. Hannon, *J. Non-Cryst. Solids* **351** (2005), p. 3179.
- [6] K. M. Wetherall, D. M. Pickup, R. J. Newport and G. Mountjoy, *J. Phys.: Condens. Matter* **21** (2009), 035109.
- [7] N. E. Brese and M. O'Keeffe, *Acta Cryst.* **B47** (1991), p. 192.
- [8] A. Hall, J. Swenson, C. Karlsson, S. Adams and D. T. Bowron, *J. Phys.: Condens. Matter* **19** (2007), 415115.
- [9] D. M. Pickup, I. Ahmed, P. Guerry, J. C. Knowles, M. E. Smith and R. J. Newport, *J. Phys.: Condens. Matter* **19** (2007), 415116.
- [10] J. Swenson, A. Matic, C. Karlsson, L. Borjesson and C. Meneghini, An investigation of the mixed mobile ion effect in glasses, *ESRF experimental report*, European Synchrotron Radiation Facility (2005).
- [11] G. Mountjoy, *J. Non-Cryst. Solids* **353** (2007), p. 1849.

Chapter 6 – Silver Calcium Sodium Phosphate I: NDIS

This chapter presents the findings of a study into the local silver environment of $(\text{P}_2\text{O}_5)_{50}(\text{CaO})_{30}(\text{Na}_2\text{O})_{10}(\text{Ag}_2\text{O})_{10}$ glass using neutron diffraction with isotopic substitution (NDIS) and Ag K-edge XANES. The results presented in this chapter can be found in R. M. Moss, D. M. Pickup, I. Ahmed, J. C. Knowles, M. E. Smith and R. J. Newport. *Adv. Funct. Mater.* **18** (2008), p. 634.

6.1 Introduction

Bioresorbable phosphate-based glasses incorporating silver ions are potential materials for antibacterial devices. Glasses have been produced of the general composition $(\text{P}_2\text{O}_5)_{50}(\text{CaO})_{30}(\text{Na}_2\text{O})_{20-x}(\text{Ag}_2\text{O})_x$ for $x = 0, 5, 10, 15$ and 20 mol%. The wide spectrum of solubility offers potential applications as temporary devices where a second device removal operation would therefore not be necessary. This property also offers a mechanism by which the antibacterial metal ions are released in a controlled way from the network. Degradation studies of these glasses have shown that the silver ions are released slowly and continuously over time when in contact with an aqueous medium [1]. Silver has been shown to exert a biocidal effect against a wide range of microbes including *Staphylococcus aureus*, *Escherichia coli*, *Pseudomonas aeruginosa*, *Candida albicans* and methicillin-resistant *Staphylococcus aureus* (MRSA) [2]. Initial cell work has shown that the antibacterial effectiveness of these glasses does not vary smoothly with silver concentration. Figure 6.1 shows that glasses containing ≥ 15 mol% Ag_2O are less effective than those with lower silver content; the same study also showed that the chemical durability of the glass increased with silver content, resulting in a reduced rate of silver ion release [1]. This latter result was used to explain the diminished antimicrobial properties at higher silver content: it was concluded that the increase in chemical durability was a result of a structural change related to the silver content.

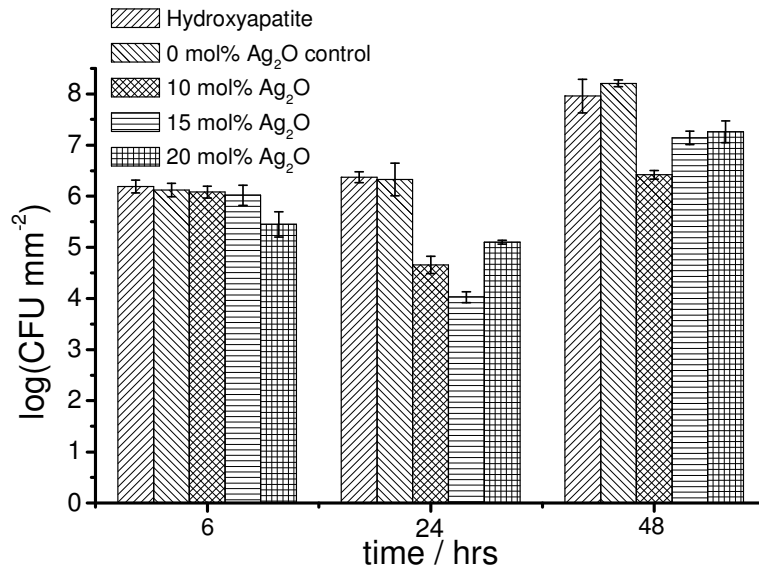


Figure 6.1: Number of viable culture forming units (CFU) present as a function of time for various silver concentrations [1].

To understand better and to optimise the antibacterial action of silver-doped phosphate based glasses it is necessary to study the structure of the glass network and to focus in particular on the local environment of the silver sites.

6.2 Characterisation of the local silver environment

The preferred choice of technique to isolate the contribution from one element (and particularly if it is a minority component) in the sample is XAS. Unfortunately, Ag K-edge EXAFS and XANES are also of limited use in this regard. The XANES measurements can reveal variations in the coordination number and/or local symmetry of the silver site between samples, but cannot yield definitive structural parameters [3]. The EXAFS results are also inconclusive due to the weak Ag K-edge EXAFS oscillations, which are a result of silver ions occupying very disordered sites in this type of material [4]. However, it is possible to use the variation in the neutron scattering length of the two stable silver isotopes (¹⁰⁷Ag and ¹⁰⁹Ag) to conduct an isotopic difference experiment to isolate the silver contribution to the network [5]. In this case it is important to prepare two samples that are identical except for the silver isotope being used.

6.3 Experimental

It should be noted that the glass was prepared by collaborators at Eastman Dental Institute (UCL) using the method and materials outlined in Ahmed *et al.* [6]. The method summarised below, and the UV-vis spectroscopy and X-ray diffraction were carried out by colleges at the University of Kent.

Sample preparation

The glass samples were prepared using NaH_2PO_4 , CaCO_3 , P_2O_5 (BDH, UK) and isotopically enriched Ag_2SO_4 as starting materials. Two samples of Ag_2SO_4 were prepared from 98.9 at% enriched ^{107}Ag and 99.4 at% enriched ^{109}Ag metal (STB Isotope, Germany) using the following method. First the powdered metal (1 g) was dispersed in deionised water (4.6 ml) before adding concentrated nitric acid (2.75 ml, BDH, UK) drop wise, whilst stirring. After 15 min., when the silver metal had dissolved and the solution cooled, a stoichiometric amount of 5 M H_2SO_4 standard solution (0.92 ml, Sigma-Aldrich, UK) was added using a pipette. After a further 1 hr, the precipitation of Ag_2SO_4 was complete. The H_2O and HNO_3 were removed from the precipitate at 40 °C using a vacuum line and a water bath to supply the heat. The resultant powder was dried under vacuum for 1.5 hrs at 300 °C using a heating mantle. As a final drying step, the Ag_2SO_4 powder was placed in an oven at 250 °C overnight.

Two 6 mm diameter $(\text{P}_2\text{O}_5)_{50}(\text{CaO})_{30}(\text{Na}_2\text{O})_{10}(\text{Ag}_2\text{O})_{10}$ glass rods were prepared using the isotopically enriched Ag_2SO_4 . The precursors were weighed out into a 30 ml silica crucible (Saint-Gobain, U.K.), mixed and the crucible loaded into a preheated furnace. The mixture was left at 300 °C for half an hour, raised to 600 °C for a further half hour and finally melted at 1200 °C for one hour. The molten glass was then poured into a 6 mm diameter graphite mould, which had been preheated to 370 °C. The mould was then left to cool slowly to room temperature in order to remove any residual stress.

Measurements of the glass density (using a Quantachrome micro pycnometer, operating with He gas) and composition (using ICP and OES by Medac Ltd., UK) show that the two samples were identical in these basic respects (within the experimental error) except for the silver isotope used in the preparation. The results of this analysis are shown in Table 6.1.

Sample	Measured composition [at%] (± 0.1)					Density [gcm^{-3}] (± 0.05)
	P	O	Ca	Na	Ag	
^{107}Ag doped glass	21.6	64.1	5.9	4.5	3.9	2.88
^{109}Ag doped glass	21.5	64.0	5.8	4.7	3.9	2.81

Table 6.1: Sample characterisation of melt-quench prepared $^{107/109}\text{Ag}$ doped phosphate glasses.

Their structural equivalence was demonstrated using high energy X-ray diffraction and the resulting X-ray interference functions, $i^X(Q)$, are shown in Figure 6.2.

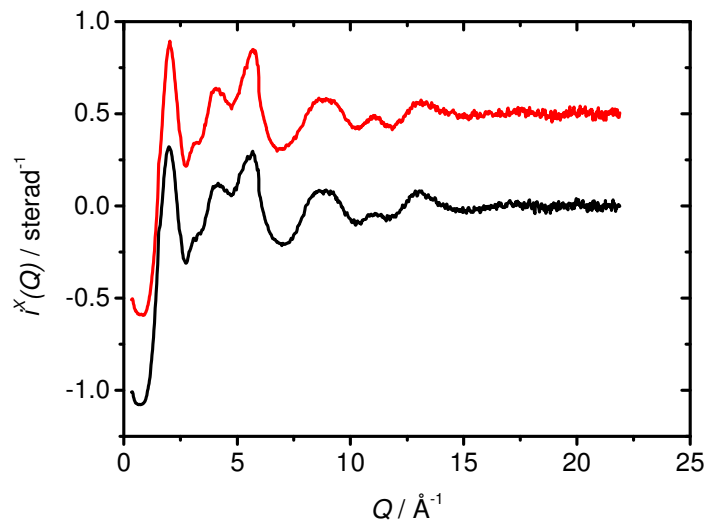


Figure 6.2: $i^X(Q)$ for ^{107}Ag (top) and ^{109}Ag (bottom) NDIS samples.

UV-vis spectroscopy

Similar materials produced by the melt-quenching method have been shown to contain silver nano-particles [7]. Absorption bands are seen in the UV-vis spectra at 200-230 nm and 400-500 nm in the presence of even small concentrations of metallic nano-particles, which refer to silver electronic transitions and surface plasmon resonances, respectively [8]. The UV-spectra from the samples prepared here were measured on a Cary 400 Scan UV-Visible Spectrophotometer and no evidence of silver nano-particulates was observed.

Neutron Diffraction

The data presented here were collected on the GEM diffractometer at the ISIS Pulsed Neutron Facility at the Rutherford Appleton Laboratory, UK [9]. The solid glass rods were mounted on a sample holder and placed directly in the neutron beam, which was trimmed to 36×12 mm. Time-of-flight data were collected over a large Q -range (up to 50 \AA^{-1}). The program *Gudrun* [10] was used to perform corrections and data reduction.

6.4 Results

The neutron interference functions, $i^N(Q)$, for the two glass samples are shown in Figure 6.3.

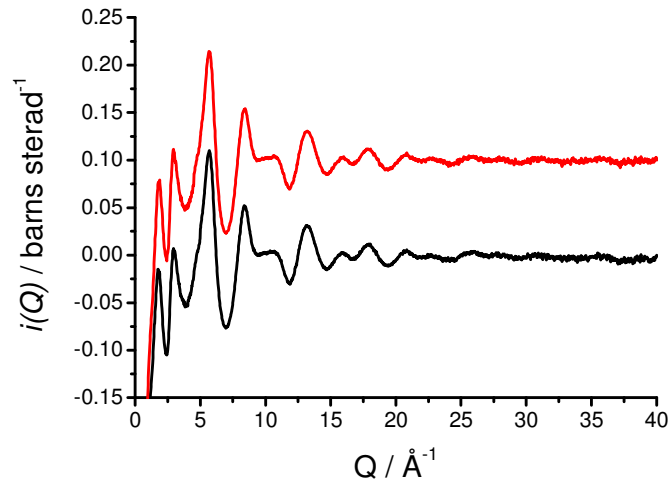


Figure 6.3: Neutron diffraction $i^N(Q)$ measured for the ^{107}Ag (upper) and ^{109}Ag (lower) doped phosphate glasses. The ^{107}Ag $i^N(Q)$ is off-set for clarity.

Fourier transformation of $i^N(Q)$ gave the real-space correlation functions, $T^{107}(r)$ and $T^{109}(r)$. Figure 6.4 shows the difference correlation function, $T_{Ag-j}(r)$, obtained by taking the first-order difference, $T^{107}(r) - T^{109}(r)$. It can be seen from Figure 6.4 that $T_{Ag-j}(r)$ in the range $0-2 \text{ \AA}$ is very flat, which is expected given that there are no Ag- j correlations in this region and further suggest that the other pairwise correlations have been removed successfully. It should also be noted that, to a good approximation, the systematic errors are also removed from a first order difference.

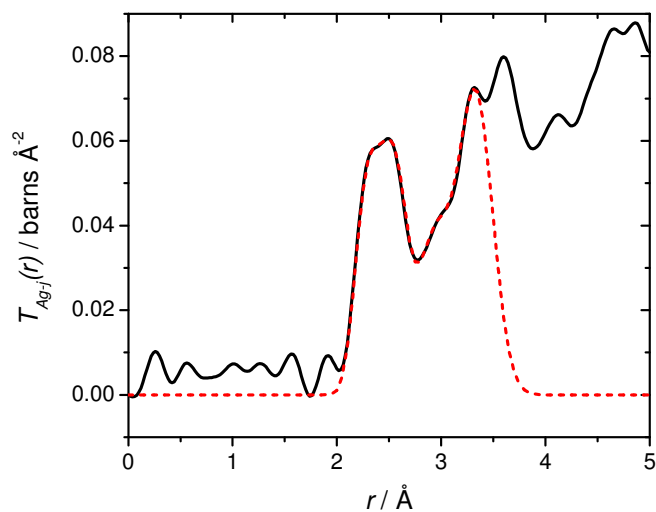


Figure 6.4: $T_{Ag-j}(r)$ for the experimentally measured (solid) and the simulated (dashed) functions.

Correlation	R / Å (±0.03)	N (±0.5)	σ / Å (±0.03)
Ag-O	2.28	2.1	0.08
Ag-O	2.51	2.7	0.09
Ag-O	2.73	1.1	0.10
Ag···O	2.99	2.5	0.12
Ag···P	3.31	6.0	0.11

Table 6.2: Ag- j correlations determined by fitting $T_{Ag-j}(r)$. Atom pairs separated by \cdots are considered to be in the second coordination sphere.

The structural parameters obtained by fitting $T_{Ag-j}(r)$, using the method described in Chapter 3, are shown in Table 6.2. Figure 6.5 shows the total correlation functions for the two samples after having the Ag- j correlations removed. Table 6.3 contains the structural parameters obtained by fitting these functions. As expected from two structurally equivalent samples, these parameters are identical within experimental error.

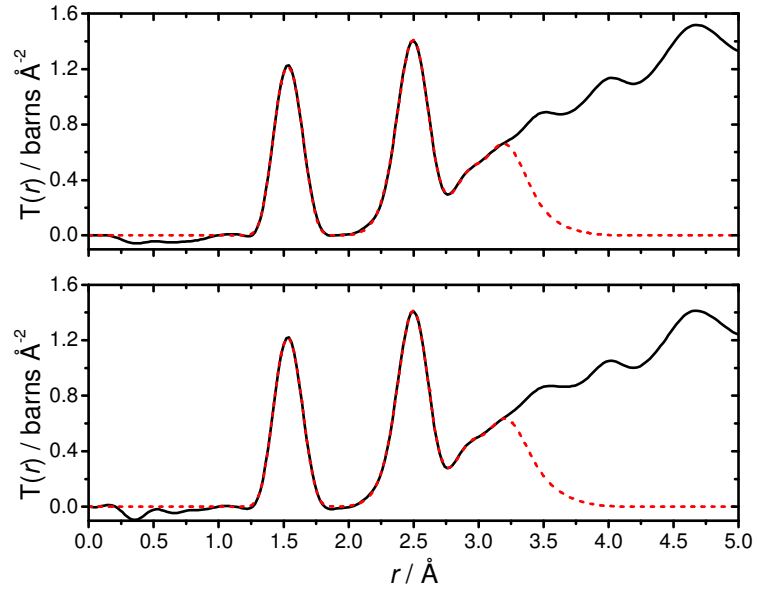


Figure 6.5: $T(r)$, with the Ag- j correlations removed (solid) for ^{107}Ag (upper) and ^{109}Ag (lower) doped samples. The real space simulation (dashed) is shown for each sample.

Sample	Correlation	$R / \text{Å}$ (± 0.01)	N (± 0.2)	$\sigma / \text{Å}$ (± 0.01)
^{107}Ag doped glass	P-NBO	1.48	1.9	0.06
	P-BO	1.60	1.9	0.06
	Na-O	2.33	3.4	0.13
	Ca-O	2.38	4.0	0.10
	O...O	2.51	4.0	0.10
	O...O	2.81	0.7	0.11
	P...P	2.93	2.2	0.08
^{109}Ag doped glass	P-NBO	1.48	1.9	0.06
	P-BO	1.60	1.9	0.06
	Na-O	2.33	3.5	0.13
	Ca-O	2.38	4.1	0.11
	O...O	2.51	4.1	0.10
	O...O	2.82	0.6	0.11
	P...P	2.93	2.2	0.08

Table 6.3: Structural parameters obtained by fitting $T(r)$. The Ag- j correlations were fixed with the values shown in Table 6.2.

6.5 Discussion

The distances and coordination numbers obtained from the $T_{Ag-j}(r)$ function (see Table 6.2) are consistent with the silver ions occupying a site surrounded by a distorted octahedron of oxygen atoms. There are three discrete Ag-O distances in the first coordination shell at 2.28 Å, 2.51 Å and 2.58 Å with associated coordination numbers of 2.1, 2.7 and 1.1, respectively. This suggests that the silver ions occupy highly disordered sites within the glass matrix. Similar disordered sites are found in crystalline materials containing polyphosphate chains (e.g. $AgBa(PO_3)_3$, Ag_2HPO_4 and $AgZn(PO)_3$) [11-13]. The observed degree of disorder is qualitatively supported by Ag K-edge EXAFS data from $(P_2O_5)_{50}(CaO)_{30}(Na_2O)_{20-x}(Ag_2O)_x$ glasses, where $x = 5, 10, 15$ and 20 mol%; this work revealed the EXAFS oscillations to be very weak, despite cooling the samples to ~ 77 K, suggesting a large degree of static disorder around the silver ions. Ag K-edge XANES measurements on the same samples have proven more successful [1, 14]. The data shown in Figure 6.6 reveals that there is no variation observed as the silver content of the samples was varied. The position of the Ag K-edges in these samples were identical to that of the reference material Ag_2SO_4 , indicating identical charge states, and the overall shape of the spectra are also similar. Thus, it may be concluded that these glasses contain Ag^+ ions in a structural environment very similar to that of silver in Ag_2SO_4 ; there is no change in this environment as a function of silver content. Since silver in Ag_2SO_4 resides in a distorted octahedral site with two short Ag-O distances of 2.39 Å, two intermediate Ag-O distances of 2.44 Å and two long Ag-O distances of 2.66 Å [4], it may now be surmised that silver occupies a qualitatively similar site in the isotopically substituted glasses. Hence, the results of the NDIS experiment are in agreement with those from the XANES study – and in addition provide data of significantly enhanced quantitative reliability across a broader set of length scales, and relating to all atom-pairs present in the glass.

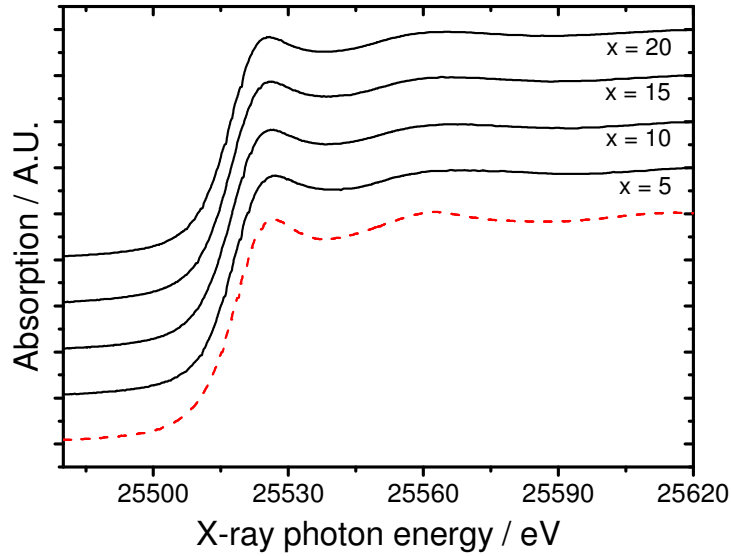


Figure 6.6: Ag K-edge XANES for samples of composition $(P_2O_5)_{50}(CaO)_{30}(Na_2O)_{20-x}(Ag_2O)_x$. The spectrum for Ag_2SO_4 is also shown (dashed) for comparison. Spectra for $x = 5$ and 10 mol% are from [14] and [1] respectively.

Furthermore, the $T_{Ag-j}(r)$ function also reveals information about the second $Ag\cdots O$ coordination sphere and the first $Ag\cdots P$ nearest neighbour distance. The distances obtained from the fitting process of 2.99 \AA and 3.21 \AA , respectively, are consistent with those observed in crystalline polyphosphate materials containing Ag^+ ions of similar composition [11].

The parameters in Table 6.3 for the P-O, Na-O, Ca-O, $O\cdots O$ and $P\cdots P$ correlations are typical of those from a metaphosphate glass [15]. The primary peak at about 1.55 \AA in the $T(r)$ functions shown in Figure 6.5 is due to P-O bonding within the PO_4^{3-} tetrahedra. Two distinct P-O distances are observed in phosphate-based glasses: a shorter distance of $\sim 1.49 \text{ \AA}$ is ascribed to bonds associated with NBOs and a longer distance of $\sim 1.60 \text{ \AA}$ due to bonds linked with BOs.

Comparing the disorder parameters for these bonds (σ_{P-NBO} and σ_{P-BO} , derived from the width of the relevant pair correlation peak) given in Table 6.3, which both have values of 0.06 \AA , with those measured in a previous study of $(P_2O_5)_{50}(CaO)_{50-x}(Na_2O)_x$ glasses [15], of $\sigma_{P-NBO} = 0.03 \text{ \AA}$ and $\sigma_{P-BO} = 0.05 \text{ \AA}$, we see there is significantly more

disorder in the P-NBO bonding in the silver-doped glasses. The origin of this difference is related to the connectivity of the PO_4^{3-} tetrahedra. In a previous ^{31}P solid state NMR study of $(\text{P}_2\text{O}_5)_{50}(\text{CaO})_{30}(\text{Na}_2\text{O})_{20-x}(\text{Ag}_2\text{O})_x$ glasses it was observed that the relative concentration of Q^1 and Q^3 species increases with silver content [1]. This result suggested that the addition of Ag^+ ions to the matrix causes disproportionation of the phosphate groups according to $2\text{Q}^2 \rightarrow \text{Q}^1 + \text{Q}^3$. It was suggested that this structural change was responsible for an increase in the chemical durability of the glass and reduced dissolution rate of the silver ions, which resulted in decreased antimicrobial potency [1]. Thus, the increase in the $\sigma_{\text{P-BO}}$ with the addition of silver observed here provides clear evidence that disproportionation is occurring. This can be understood by considering the nature of the P-NBO bonds in the various Q^n species using a simple bond order model [16]. Given that the phosphorus valence can be considered as +5 and the oxygen valence as -2, the P-NBO bond order ($\eta_{\text{P-NBO}}$) can be calculated from the simple expression $\eta_{\text{P-NBO}} = (5 - N_{\text{BO}}) / N_{\text{NBO}}$, where N_{BO} and N_{NBO} are the number of BOs and NBOs per unit. For Q^1 , Q^2 and Q^3 units $\eta_{\text{P-NBO}}$ is 1.33, 1.5 and 2.0 respectively. It is expected that the P-NBO distance will vary inversely with the bond order. Table 6.4 lists the P-NBO bond distances for the Q^n species found in crystalline and amorphous sodium and calcium phosphates and confirms the variation of P-NBO distance with bond order. Hence, if disproportionation occurs in phosphate-based glasses the increase in the number of Q^n species present will introduce static disorder into the P-NBO bonding, as observed here.

Q^n species	Compound	Form	Bond length / Å	
			P-NBO	P-BO
Q^1	$\text{Na}_4\text{P}_2\text{O}_7$	Crystalline	1.51 ^a	1.63 ^a
	$\text{Ca}_2\text{P}_2\text{O}_7$	Crystalline	1.52 ^a	1.62 ^a
Q^2	NaPO_3	Crystalline	1.48 ^a	1.61 ^a
	NaPO_3	Amorphous	1.48 ^b	1.61 ^b
	CaP_2O_6	Crystalline	1.49 ^a	1.58 ^a
	CaP_2O_6	Amorphous	1.49 ^b	1.60 ^b
	$\text{Ca}_2\text{NaP}_5\text{O}_{15}$	Amorphous	1.49 ^b	1.60 ^b
Q^3	$\nu\text{-P}_2\text{O}_5$	Amorphous	1.43 ^c	1.58 ^c

Table 6.4: P-NBO and P-BO bond length variation for different Q^n speciation and cations modifiers in crystalline and amorphous samples. Parameters taken from ^a[5], ^b[12] and ^c[13].

The O···O distances measured give information on the PO₄, CaO_x, and NaO_x polyhedra that comprise the structure. Taking an average P-O bond length of 1.54 Å and assuming a tetrahedral angle of 109°, the calculated average O···O distance for the PO₄ group is 2.51 Å which agrees exactly with the shorter O···O distance measured here. The longer O···O distance is probably associated with the separation between phosphate groups which are not directly connected to each other, but this assignment remains tentative. The structural parameters for the Ca-O and Na-O correlations are consistent with those previously found in phosphate-based glasses [15, 17].

6.6 Conclusions

Neutron diffraction with isotopic substitution has been used to reveal three distinct Ag-O distances in (P₂O₅)₅₀(CaO)₃₀(Na₂O)₁₀(Ag₂O)₁₀ melt-quench derived glass. The results are consistent with silver being in a highly distorted octahedral environment and agree with those from Ag K-edge XANES measurements on (P₂O₅)₅₀(CaO)₃₀(Na₂O)_{20-x}(Ag₂O)_x glasses, where x = 5, 10, 15 and 20 mol%. Since the XANES spectra exhibited no variation as a function of silver content, it is concluded that the Ag⁺ ions adopt this environment at all the compositions studied. The introduction of silver ions causes disproportionation of phosphate network forming units. The Q² rings and chains that are normal for metaphosphate glasses are transformed into Q¹ and Q³ units. This is confirmed by the broadening of the P-NBO correlation compared to glasses containing no silver. It is this subtle change in the network structure, not observed directly hitherto, that is likely to be the cause of the decreased biocidal efficacy of the glass at higher silver contents.

6.7 References

- [1] S. P. Valappil, D. M. Pickup, D. L. Carroll, C. K. Hope, J. Pratten, R. J. Newport, M. E. Smith, M. Wilson and J. C. Knowles, *Antimicrob. Agents Chemother.* **51** (2007), p. 4453.
- [2] P. S. Stewart and J. William Costerton, *The Lancet* **358** (2001), p. 135.
- [3] O. Sivr, G. Dalba and F. Rocca, *Phys. Rev. B* **69** (2004), 134201.
- [4] D. A. Fletcher, R. F. McMeeking and D. Parkin, *J. Chem. Inf. Comput. Sci.* **36** (1996), p. 746.
- [5] J. C. Wasse, I. Petri and P. S. Salmon, *J. Phys.: Condens. Matter* **13** (2001), p. 6165.
- [6] I. Ahmed, D. Ready, M. Wilson and J. C. Knowles, *J. Biomed. Mater. Res., Part A* **79A** (2006), p. 618.
- [7] L. Baia, M. Baia, W. Kiefer, J. Popp and S. Simon, *Chem. Phys.* **327** (2006), p. 63.
- [8] L. Baia, D. Muresan, M. Baia, J. Popp and S. Simon, *Vib. Spectrosc.* **43** (2007), p. 313.
- [9] A. C. Hannon, *Nucl. Instrum. Methods Phys. Res., Sect. A* **551** (2005), p. 88.
- [10] S. E. McLain, D. T. Bowron, A. C. Hannon and A. K. Soper, GUDRUN, A computer program developed for analysis of neutron diffraction data., (2006).
- [11] M. T. Averbuchpouchot and A. Durif, *J. Solid State Chem.* **49** (1983), p. 341.
- [12] I. Belharouak, H. Aouad, M. Mesnaoui, M. Maazaz, C. Parent, B. Tanguy, P. Gravereau and G. Le Flem, *J. Solid State Chem.* **145** (1999), p. 97.
- [13] I. Tordjman, A. Boudjada, J. C. Guitel and R. Masse, *Acta Crystallogr.* **B34** (1978), p. 3723.
- [14] I. Ahmed, E. A. Abou Neel, S. P. Valappil, S. N. Nazhat, D. M. Pickup, D. Carta, D. L. Carroll, R. J. Newport, M. E. Smith and J. C. Knowles, *J. Mater. Sci.* **42** (2007), p. 9827.
- [15] D. M. Pickup, I. Ahmed, P. Guerry, J. C. Knowles, M. E. Smith and R. J. Newport, *J. Phys.: Condens. Matter* **19** (2007), 415116.
- [16] U. Hoppe, G. Walter, R. Kranold and D. Stachel, *J. Non-Cryst. Solids* **263** (2000), p. 29.
- [17] R. K. Brow, *J. Non-Cryst. Solids* **263** (2000), p. 1.

Chapter 7 – Silver Calcium Sodium Phosphate II: Total Diffraction & RMC

7.1 Introduction

The NDIS results suggested that further investigation was required into the role of silver in these glasses and its effect on the underlying phosphate network. Samples were prepared over a range of compositions and X-ray and neutron diffraction data were collected. The structural analysis was supplemented with RMC models to simulate two of the samples.

7.2 Experimental

Sample preparation

Samples were prepared of the general composition $(P_2O_5)_{50}(CaO)_{30}(Na_2O)_{20-x}(Ag_2O)_x$ for $x = 0, 5, 15$ and 20 mol% by collaborators at Eastman Dental Institute (UCL) using the method and materials outlined by Valappil *et al.* [1]. A sample containing 10 mol% Ag_2O was not necessary as this had been measured *via* the isotope experiment. Due to the lower cost of the raw materials, 8 mm diameter rods were cast for the neutron diffraction experiment. A small amount of each sample was ground into a fine powder in a Retsch RM100 grinder for use in the X-ray diffraction experiment. Table 7.1 shows the nominal glass composition and the density of each sample given by helium pycnometry (using a Quantachrome micro pycnometer).

x / mol% (batch composition)	Nominal composition / at% (± 0.1)					Density / gcm^{-3} (± 0.05)
	P	O	Ca	Na	Ag	
5	21.3	63.8	6.4	6.4	2.1	2.67
15	21.3	63.8	6.4	2.1	6.4	2.89
20	21.3	63.8	6.4	-	8.5	3.02

Table 7.1: Compositions and measured densities for $(P_2O_5)_{50}(CaO)_{30}(Na_2O)_{20-x}(Ag_2O)_x$ samples.

High Energy X-ray Diffraction

The data were collected on Station 9.1 at the Synchrotron Radiation Source at Daresbury Laboratory, UK. The instrument was set up to collect data in theta-two theta geometry with a 12×1 mm beam of monochromatic ($\lambda = 0.509 \text{ \AA}$, $E = 24.350$

keV) X-rays incident on the sample. The sample holders were aluminium disks of thickness 0.5 mm. The glass was ground into a fine powder and was packed into a 15 × 5 mm rectangular cut-out in the sample holder. The sample was held in place by a thin layer of Kapton on the front and back faces of the holder.

Neutron Diffraction

The data presented here were collected on the GEM diffractometer at the ISIS Pulsed Neutron Facility at the Rutherford Appleton Laboratory, UK [2]. The solid glass rods were mounted on a sample holder and placed directly in the neutron beam. The jaws were set to define a beam size of 40 × 15 mm at the sample. Time-of-flight data were collected over a large Q -range (up to 50 Å⁻¹). The program *Gudrun* [3] was used to perform corrections and data reduction.

7.3 Results

An RMC model was constructed to simulate the structure of $(P_2O_5)_{50}(CaO)_{30}(Na_2O)_{20-x}(Ag_2O)_x$ for $x = 10$ and 20 mol% for comparison with the calcium sodium metaphosphate glass (equivalent to $x = 0$ mol%) in Chapter 5. The model consisted of 1128 atoms labelled according to the glass compositions (*i.e.* 240 P, 240 BO, 480 NBO, 72 Ca and, for $x = 10$ mol%, 48 Na with 48 Ag or, for $x = 20$ mol %, 96 Ag). The ¹⁰⁷Ag NDIS data was used for the $x = 10$ mol% simulation. Time limitations meant that it was not possible to build models for samples with $x = 5$ and 15 mol%.

The same coordination and triplet constraints were applied to the PO₄, CaO_x and NaO_x polyhedra as outlined in Chapter 5. The AgO_x polyhedra were defined by the same coordination constraints as NaO_x. The simulation was run for a short period until all the constraints were satisfied to a reasonable degree (*i.e.* > 98% of atoms obeyed relevant constraints). The model was further refined by comparing it to the experimental data.

The final RMC models for samples with $x = 10$ and 20 mol% Ag₂O are shown in Figure 7.1 along with the diffraction data for each sample in Q space.

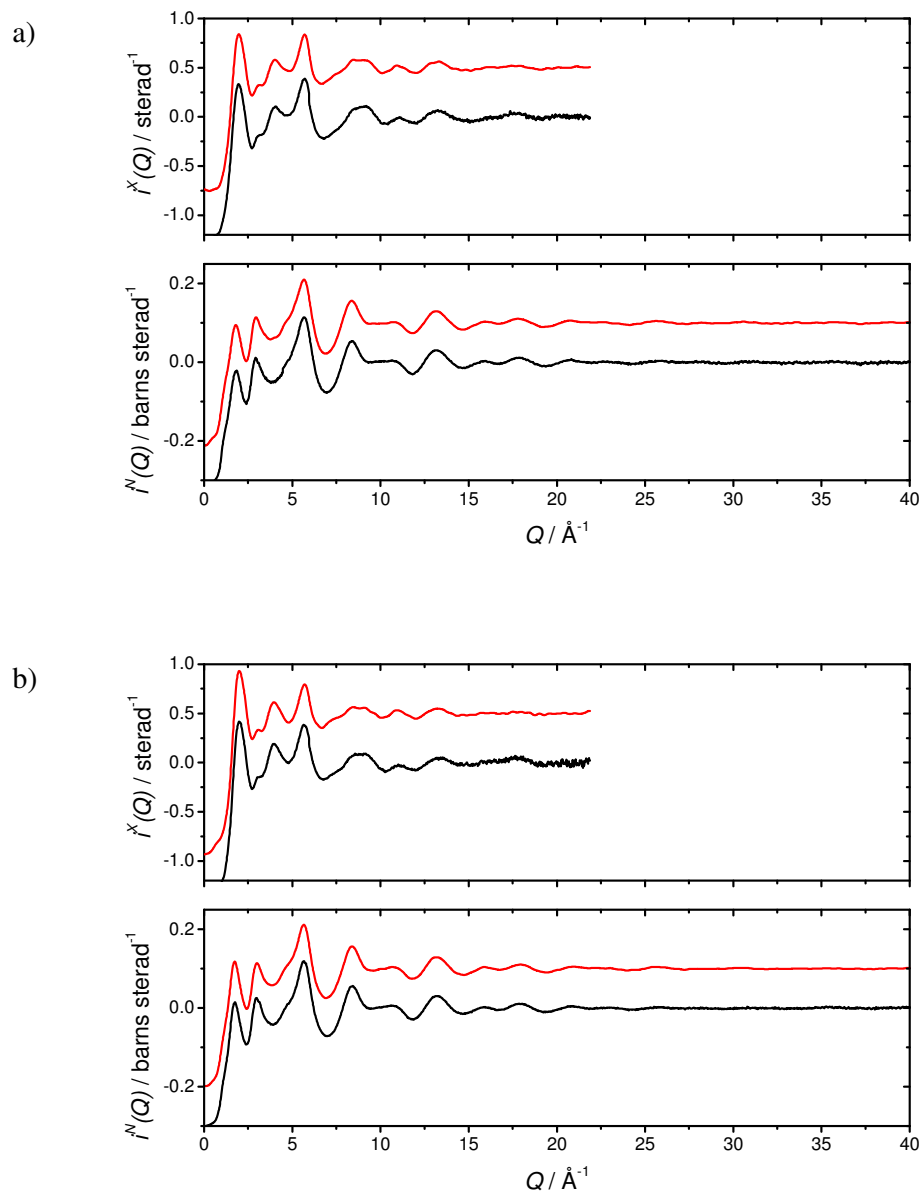


Figure 7.1: a) X-ray (top) and neutron (bottom) $i(Q)$ (black) with RMC model (red) for sample with $x = 10$ mol% and b) likewise for sample with $x = 20$ mol% Ag_2O .

The structural parameters from the RMC model are outlined in Table 7.2. R_{ij} was calculated as per Equation 5.2 and N_{ij} was determined using the RMC utility program *Neighbours* with r_1 and r_2 defining the shell boundaries. The lower bound, r_1 , was set equal to the cut-offs and the upper bound, r_2 , was determined by looking for plateaus in $C_{ij}(r)$ (see Equation 5.1 and related text).

Sample	Correlation	$R_{ij} / \text{\AA}$	N_{ij}	Shell boundaries / \AA	
				r_1	r_2
x = 10 mol%	P··P	2.96	2.0	2.75	3.24
	P-BO	1.59	2.0	1.48	1.80
	P-NBO	1.53	2.0	1.36	1.66
	P··Ca	3.62	1.5	3.00	4.24
	P··Na	3.70	1.1	3.00	4.42
	P··Ag	3.56	0.9	3.00	4.24
	BO··BO	2.57	2.0	2.20	3.00
	BO··NBO	2.52	3.8	2.20	2.86
	BO··Ca	4.10	2.5	3.00	5.00
	BO··Na	4.01	1.6	3.00	5.00
	BO··Ag	4.09	1.7	3.00	5.00
	NBO··NBO	2.49	1.5	2.20	2.80
	NBO-Ca	2.56	0.7 (4.9)	2.05	3.10
	NBO-Na	2.57	0.4 (4.2)	2.00	3.10
	NBO-Ag	2.48	0.5 (4.7)	2.00	3.10
	Ca··Ca	3.33	0.9	3.00	3.78
	Ca··Na	3.38	0.8	3.00	4.00
	Ca··Ag	3.60	0.8	3.00	4.08
	Na··Na	3.63	1.5	3.00	5.00
	Na··Ag	3.78	1.4	3.00	5.00
Ag··Ag	4.04	1.4	3.00	5.00	
x = 20 mol%	P··P	3.03	2.0	2.75	3.30
	P-BO	1.59	2.0	1.48	1.90
	P-NBO	1.52	2.0	1.36	1.64
	P··Ca	3.56	1.4	3.00	4.10
	P··Ag	3.52	1.7	3.00	4.06
	BO··BO	2.52	1.8	2.20	2.80
	BO··NBO	2.50	3.5	2.20	2.80
	BO··Ca	4.06	3.2	3.00	5.38
	BO··Ag	4.08	3.5	3.00	5.12
	NBO··NBO	2.48	1.4	2.20	2.80
	NBO-Ca	2.64	0.8 (5.3)	2.05	3.10
	NBO-Ag	2.54	1.0 (4.9)	2.00	3.10
	Ca··Ca	3.84	1.7	3.00	5.00
	Ca··Ag	3.92	2.6	3.00	5.00
	Ag··Ag	3.94	2.7	3.00	5.00

Table 7.2: Structural parameters derived from the RMC models. N_{ij} values shown in parentheses are the coordination numbers given in the opposite sense (*i.e.* N_{ji}).

In terms of the RMC model it was the parameters relating the MO_x polyhedra that were of particular interest. The parameters for other correlations compare well with those shown in Table 5.2 and are consistent with metaphosphate structures. Closer inspection of the M-O correlations produced by the RMC simulation show that the CaO_x polyhedra tends to be more highly distorted compared to the calcium sodium metaphosphate glass studied in Chapter 5. Figure 7.2 shows $g_{\text{NBOCa}}(r)$ for samples with $x = 0, 10$ and 20 mol% Ag_2O . The Ca-NBO bond length distribution shifts from a fairly sharp, well defined distribution (in $x = 0$ mol%) to a distribution that becomes progressively more spread out as the silver concentration is increased; indicative of a higher level of distortion in the CaO_x polyhedra, similar to that described by Wetherall *et al.* [4].

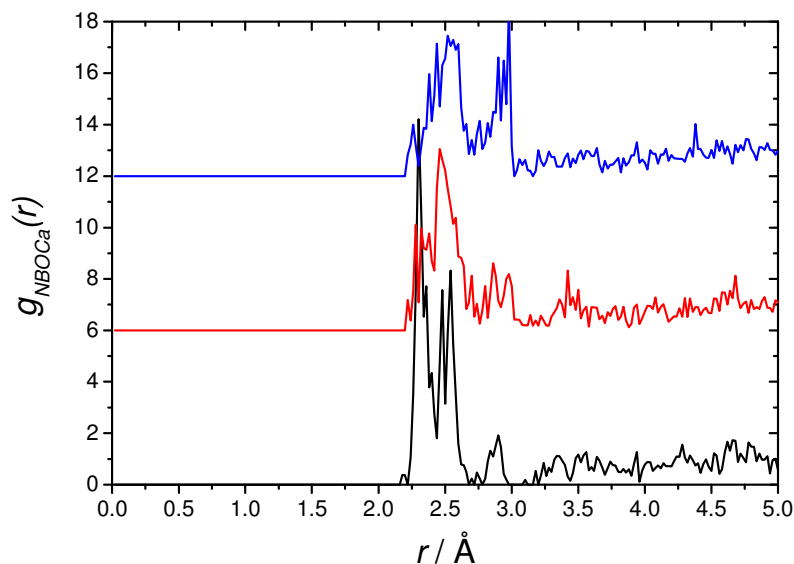


Figure 7.2: $g_{\text{NBOCa}}(r)$ for samples with $x = 0$ (bottom), 10 (middle) and 20 (top) mol% Ag_2O . An off-set has been applied for clarity.

Figure 7.3 shows the $g_{ij}(r)$ and $C_{ij}(r)$ for the NBO-Ag correlations. It can be seen that the $C_{\text{AgNBO}}(r)$ exhibits two plateaus, one at ~ 2.75 Å and the other at ~ 3.00 Å, suggesting that there are two distinct distances in the AgO_x polyhedra. The NDIS results suggested that there are three Ag-O distances in these materials and the positions of these distance are marked in Figure 7.3. It can be seen that the NDIS

distances all lie within the distribution of Ag-O distances given by the RMC, showing consistency between the two techniques and emphasising the high degree of disorder in the AgO_x polyhedra.

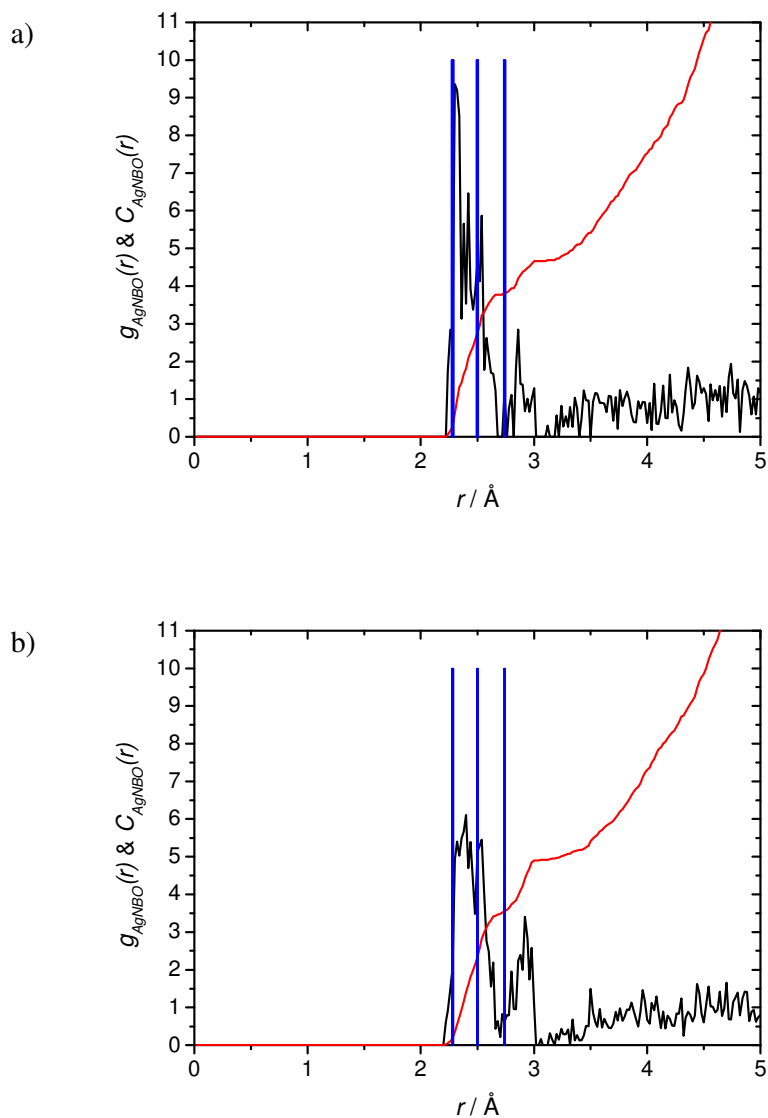


Figure 7.3: $g_{\text{AgNBO}}(r)$ (black) and $C_{\text{AgNBO}}(r)$ (red) for a) $x = 10$ mol% and b) $x = 20$ mol% Ag_2O . The positions of the three NDIS derived Ag-O correlations are also shown (blue).

The RMC results were used to estimate starting parameters for fitting the experimental diffraction data and two Ca-O and Ag-O correlations have been fitted to account for the broad distribution of distances, as shown by Figure 7.3. Again, two peaks have been used to act as “background fillers” and the parameters yielded by fitting these

peaks can be ignored. The starting parameters were optimised using *NXFit*. The broad distribution of Ca-O and Ag-O distances means that the values of R_{ij} quoted in Table 7.2 for these correlations are relatively inaccurate. Instead, the peak positions were estimated from the RMC $g_{ij}(r)$ for these atom pairs. Table 7.3 shows the optimised output structural parameters from *NXFit* for samples $x = 5, 15$ and 20 mol%. The background-filling peaks are identified by the light grey characters.

Sample	Correlation	$R / \text{\AA}$ (± 0.02)	N (± 0.2)	$\sigma / \text{\AA}$ (± 0.02)
x = 5 mol%	P-O	1.54	3.8	0.08
	Na-O	2.35	4.1	0.10
	Ca-O	2.38	4.1	0.14
	Ag-O	2.45	4.0	0.14
	O...O	2.51	4.1	0.09
	Ca-O	2.86	2.0	0.07
	Ag-O	2.90	1.8	0.09
	P...P	2.98	2.0	0.09
	O...O	3.18	4.7	0.21
	P...Ag	3.54	2.7	0.27
x = 15 mol%	P-O	1.54	3.8	0.08
	Na-O	2.37	4.1	0.08
	Ca-O	2.42	3.8	0.14
	Ag-O	2.42	3.8	0.16
	O...O	2.51	4.0	0.09
	Ca-O	2.88	2.1	0.06
	Ag-O	2.92	1.8	0.06
	P...P	3.01	1.8	0.09
	O...O	3.23	4.5	0.19
	P...Ag	3.47	2.8	0.22
x = 20 mol%	P-O	1.54	3.8	0.08
	Ca-O	2.42	3.9	0.10
	Ag-O	2.43	3.8	0.15
	O...O	2.51	3.9	0.10
	Ca-O	2.89	2.2	0.06
	Ag-O	2.92	1.9	0.10
	P...P	3.00	2.2	0.05
	O...O	3.28	4.5	0.17
	P...Ag	3.52	4.3	0.22

Table 7.3: Optimised structural parameters output by *NXFit* upon co-fitting X-ray and neutron diffraction data of $(\text{P}_2\text{O}_5)_{50}(\text{CaO})_{30}(\text{Na}_2\text{O})_{20-x}(\text{Ag}_2\text{O})_x$.

The fits to the experimental data produced by the parameters in Table 7.3 are shown in Figure 7.4.

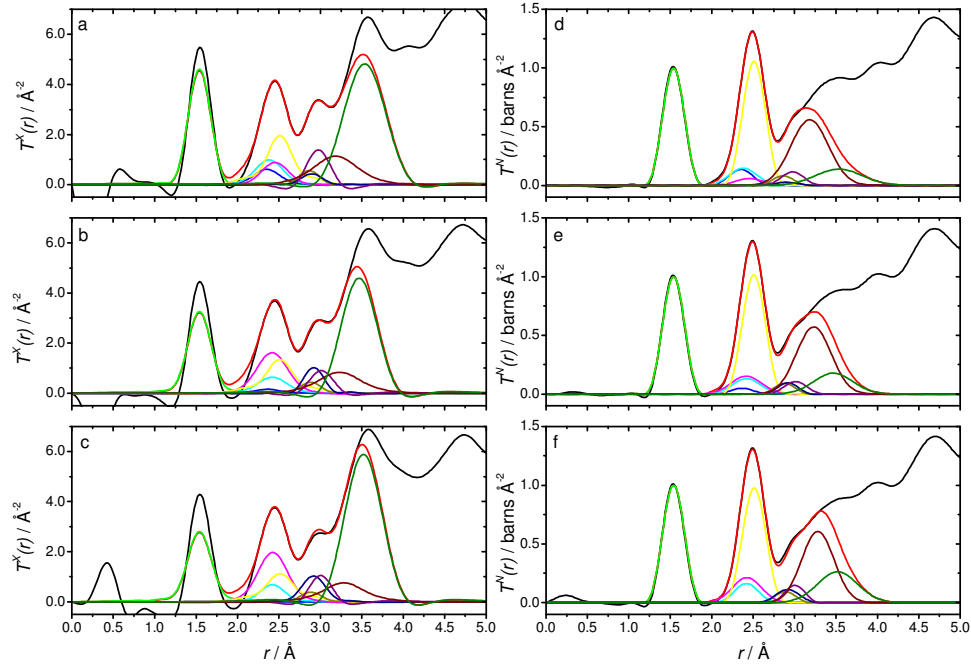


Figure 7.4: Fits to the experimental data for X-ray (left) and neutron (right) diffraction for samples with $x = 5$ (a,d), 15 (b,e) and 20 (c,f) mol% Ag_2O .

7.4 Discussion

The first set of parameters in Table 7.3 for each sample refers to the P-O bonding. It is evident from Figure 7.4 that the first peak in $T(r)$ cannot be fitted in both the X-ray and neutron data. Furthermore, it is noted that the disparity between the two techniques becomes more pronounced as the silver concentration is increased. Soper [5] defines a ratio, $B(Q)$, as:

$$B(Q) = \frac{I_{\text{Self}}(Q)}{f_e^2(Q)} \quad 7.1$$

using the nomenclature defined in Chapter 3. Soper argues that since $B(Q)$ is not flat with Q , normalising the X-ray diffraction data to $f_e^2(Q)$ (as is the case here, see

Equation 3.12) could introduce spurious features in $T^X(r)$. Figure 7.4 compares $B(Q)$ for samples with $x = 0$ and 20 mol% Ag_2O .

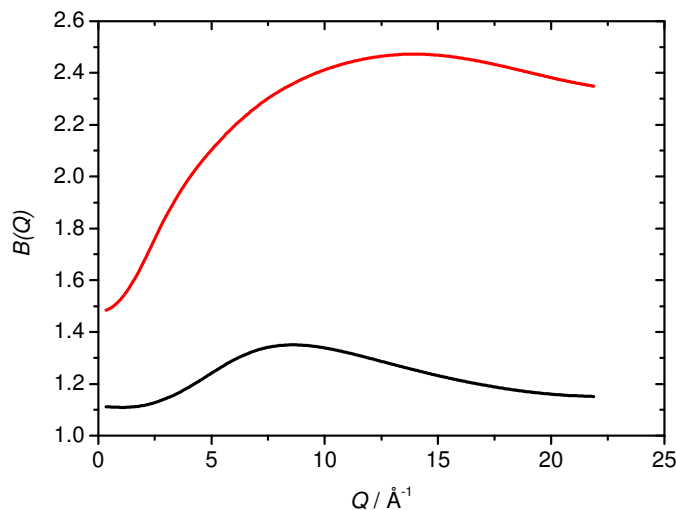


Figure 7.5: $B(Q)$ for sample with $x = 0$ (bottom) and 20 (top) mol% Ag_2O .

It can be seen in Figure 7.5 that not only does $B(Q)$ become larger when atoms with higher Z are introduced, but also the variation of $B(Q)$ becomes more severe; which may account for the observed increase in P-O disagreement with silver content. In the context of the results presented here, the effect of $B(Q)$ seems to be limited to the low r region of $T^X(r)$ since there is good agreement with the other correlations between the X-ray and neutron data. However, the interpretation of the co-fitted parameters should be treated with more caution until the origin of the disparity is more fully understood. Soper [5] goes on to recommend that X-ray data be normalised to $I_{\text{self}}(Q)$ to remove the Q -dependence as shown by $B(Q)$ and that this normalisation comes closest to forming a nuclear-like structure factor from X-ray diffraction data.

It is also possible that the P-O disparity is related to inaccuracies in the atomic form factors themselves. The form factors being used here are those found in the *International Tables of Crystallography* and those tabulated by Cromer and Mann [6], which are fairly old and in the case of Cromer and Mann are quoted as being accurate up to $Q \approx 18 \text{ \AA}^{-1}$. More modern tables exist which parameterise the atomic form factors to a higher degree of accuracy. For example, the parameters tabulated by

Waasmaier and Kirfel [7] are quoted as being accurate up to $Q \approx 75 \text{ \AA}^{-1}$. It is suggested that using these tables may improve the results of analysing and fitting X-ray diffraction data. However, owing to time constraints, these suggestions could not be tested here but should be investigated in the future.

Despite being unable to co-fit the first peak in $T(r)$, the neutron diffraction data can be used alone to determine the contributions of the P-NBO and P-BO correlations to the P-O bonding. Figure 7.6 show $T^N(r)$ over the range 1.0-2.0 \AA . In this case $i^N(Q)$ has been Fourier transformed using a maximum Q value of 50 \AA^{-1} and no modification has been applied in order to maximise the real space resolution. Also shown in Figure 7.6 are the fitted P-NBO and P-BO contributions.

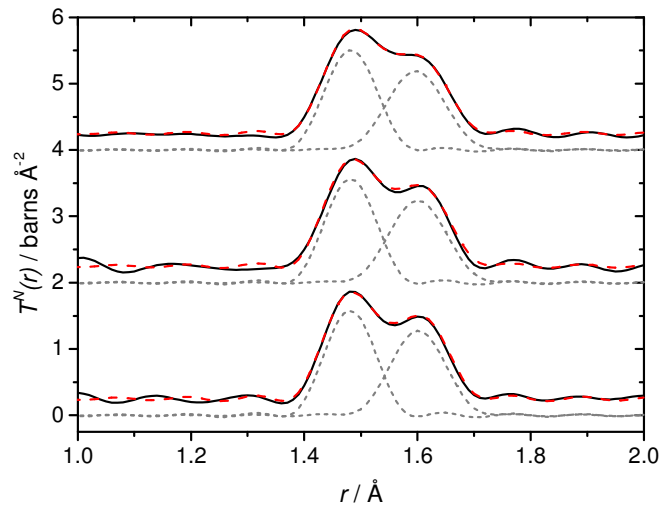


Figure 7.6: $T^N(r)$ for samples $x = 5$ (bottom), 15 (middle) and 20 (top) mol% Ag_2O highlighting the split in the P-O peak. The contributions are from P-NBO (left) and P-BO (right).

The structural parameters obtained by fitting the P-O contributions are shown in Table 7.4. According to these results there is no appreciable variation in the P-O bonding compared to the $(\text{P}_2\text{O}_5)\text{-(CaO)\text{-(Na}_2\text{O)}$ glass studied in Chapter 5. On this basis it is concluded that the structure is composed predominantly of Q^2 units. However the disproportionation mechanism suggested in Chapter 6 is not discounted since the related ^{31}P NMR by Valappil *et al.* [1] shows the presence of Q^1 and Q^3 groups. They do not, however, quantify the proportions of each Q^n species and it is therefore

difficult to predict how much variation in the P-O bonding should be observed by this method.

Sample	Correlation	$R / \text{Å}$ (± 0.01)	N (± 0.1)	$\sigma / \text{Å}$ (± 0.01)
x = 5 mol%	P-NBO	1.48	2.0	0.04
	P-BO	1.60	1.9	0.05
x = 15 mol%	P-NBO	1.48	2.0	0.04
	P-BO	1.60	1.9	0.05
x = 20 mol%	P-NBO	1.48	1.9	0.04
	P-BO	1.60	1.9	0.05

Table 7.4: P-NBO and P-BO structural parameters derived from fitting $T^N(r)$.

The Ca-O and Ag-O coordination numbers given by the RMC simulation are lower than anticipated. A breakdown of the silver environment in the RMC model reveals that the majority (~91%) are in 4- and 5-coordinated geometries (within the coordination shell defined by r_1 and r_2 , see Table 7.2) where 6-fold coordination is expected based on the NDIS and XANES results. This could suggest that the model was too highly constrained, but RMC can only be used to produce a fit to the experimental data based on its constraints. If the constraints are not sufficient or too relaxed then the RMC process will undoubtedly produce a non-physical solution. This is an intrinsic limitation of RMC. The structure of these glasses could be further investigated with other computation simulation methods, such as molecular dynamics, where the only constraint (other than composition and density) is the interatomic potentials assigned by the user.

The structural parameters in Table 7.3 that define the MO_x polyhedra nevertheless demonstrate good agreement with the structural parameters determined by the NDIS. The fit to the experimental data shows both the calcium and the silver in 6-fold environments, with four short and two long bond lengths, consistent with a high degree of disorder in these moieties. It should be noted that the $T^N(r)$ in the NDIS experiment is fitted with a second O...O distance at $\sim 2.81 \text{ Å}$ (see Table 6.3) consistent with the work of Pickup *et al.* [8]. In hindsight this correlation should have been assigned to Ag-O and/or Ca-O (as it has been in Table 7.3) in accordance with the work of

Wetherall *et al.* [4]. Sodium is coordinated by four NBOs, which is the same in all samples studied.

The P-O, O \cdots O and P \cdots P correlations can be used to calculate the average O-P-O and P-O-P bond angles as 109.2° and 153.8° respectively. The O-P-O angle is typical of the phosphate tetrahedra units while the P-O-P angle is significantly wider than its counterpart found in Chapter 5 for the calcium sodium metaphosphate. There may be some structural change in the P-O-P bonding resulting from the addition of silver, but as previously mentioned, the existence of overlapping correlations in the region of $r > \sim 2.8$ Å in multi-component glasses necessarily leaves this as a tentative suggestion.

7.5 Conclusions

The MO_x polyhedra identified here appear to be consistent with our current understanding of phosphate glasses. Sodium is coordinated by four NBOs across all compositions studied. Calcium appears to occupy a distorted octahedral environment with four short and two longer NBO distances. This is in contrast to the silver-free glass where the CaO₆ polyhedra have fairly uniform Ca-O distances. This result correlates with the Ca²⁺ release rate measured by Valappil *et al.* [1], which is observed to decrease with increasing silver content. The situation is similar for silver, where each Ag⁺ cation is coordinated by six NBOs over a range of distances. The bond length distribution of these moieties is nominally supported by RMC, but predominantly by the NDIS study in Chapter 6. The average calcium and silver coordination numbers given by the RMC were less than expected. It is suggested that the RMC model was too highly constrained to allow sufficient flexibility.

A problem occurs relating to the agreement of the P-O peak between the X-ray and neutron data and becomes progressively worse as the silver content is increased. The origin of the disparity is not fully understood but the most likely explanation is in terms of the silver X-ray form factor introducing spurious feature in $T^X(r)$.

7.6 References

- [1] S. P. Valappil, D. M. Pickup, D. L. Carroll, C. K. Hope, J. Pratten, R. J. Newport, M. E. Smith, M. Wilson and J. C. Knowles, *Antimicrob. Agents Chemother.* **51** (2007), p. 4453.
- [2] A. C. Hannon, *Nucl. Instrum. Methods Phys. Res., Sect. A* **551** (2005), p. 88.
- [3] S. E. McLain, D. T. Bowron, A. C. Hannon and A. K. Soper, GUDRUN, A computer program developed for analysis of neutron diffraction data., (2006).
- [4] K. M. Wetherall, D. M. Pickup, R. J. Newport and G. Mountjoy, *J. Phys.: Condens. Matter* **21** (2009), 035109.
- [5] A. K. Soper, *J. Phys.: Condens. Matter* **19** (2007), 335206.
- [6] D. T. Cromer and J. B. Mann, *Acta Crystallogr.* **A24** (1968), p. 321.
- [7] D. Waasmaier and A. Kirfel, *Acta Crystallogr.* **A51** (1995), p. 416.
- [8] D. M. Pickup, I. Ahmed, P. Guerry, J. C. Knowles, M. E. Smith and R. J. Newport, *J. Phys.: Condens. Matter* **19** (2007), 415116.

Chapter 8 – Zinc Titanium Calcium Sodium Phosphate: Total Diffraction & XAS

8.1 Introduction

Glasses of the general composition $(\text{P}_2\text{O}_5)_{50}(\text{CaO})_{30}(\text{Na}_2\text{O})_{20-x}(\text{TiO}_2)_x$ demonstrate increased chemical durability compared to the ternary glass of composition $(\text{P}_2\text{O}_5)_{50}(\text{CaO})_{30}(\text{Na}_2\text{O})_{20}$, which Abou Neel *et al.* [1] attribute to the formation of hydrolysis resistant P-O-Ti bonds. Ti K-edge XANES has shown that the titanium site remains unchanged after the sample has been immersed in water for varying amounts of time [2]. The slower release of Ca^{2+} and Ti^{4+} ions from the network appears to have a positive effect on cell behaviour [3]. Another recent study reports on zinc doped glasses with general composition $(\text{P}_2\text{O}_5)_{50}(\text{CaO})_{40-x}(\text{Na}_2\text{O})_{10}(\text{ZnO})_x$. During dissolution, Zn^{2+} ions are released from the glass structure and have been shown to improve cell attachment and proliferation [4]. Furthermore the Zn^{2+} release rate is observed to increase as the zinc concentration increased in these glasses [5].

In this study, calcium-sodium phosphate glasses have been doped with zinc and titanium to produce a new material. ZnO was added at the expense of CaO, and since both are divalent cations there was no effect on the overall [O]/[P] fraction, which is a determining factor in the host network connectivity. Glasses were manufactured with the composition $(\text{P}_2\text{O}_5)_{50}(\text{CaO})_{30-x}(\text{Na}_2\text{O})_{15}(\text{TiO}_2)_5(\text{ZnO})_x$ for $x = 1, 3$ and 5 . An initial collaborative study by Abou Neel *et al.* [6] presents the findings of various biological tests on these glasses, including dissolution studies and ^{23}Na and ^{31}P NMR. The dissolution was measured in terms of ion release rate and it was found that the level of Zn^{2+} release was reduced by three orders of magnitude upon the addition of TiO_2 . The Zn^{2+} ion release rate was measured by ion chromatography (Dionex, UK). The ^{31}P NMR results showed the presence of Q^3 species and the Abou Neel *et al.* [6] suggest that the titanium acts as a network former in these samples, which also accounts for the heightened chemical durability. The ^{23}Na NMR did not exhibit any variation with composition, implying that the sodium environment remains constant.

The attempt to characterise in detail the atomic-scale structure of multi-component glasses such as these is often deferred in favour of glasses containing just two or three elements, because elucidation of the structure is relatively straightforward in these cases. The existence of convolved real-space correlations is an endemic problem when attempting to define the structure of glasses containing a large number of atom types. This work focuses on using a cogent combination of complementary techniques to reveal the structural configuration of these multicomponent glasses.

8.2 Experimental

Sample Preparation

The glass samples were prepared using NaH_2PO_4 , CaCO_3 , P_2O_5 , TiO_2 and ZnO (BDH, UK) as the starting materials. The glasses were formed by a conventional melt-quench method as outlined by Abou Neel *et al.* [6]. The samples were cast into 8 mm diameter rods in a preheated graphite mould and left to cool to room temperature.

Measurements of the glass density (using a Quantachrome micro pycnometer, operating with He gas) and composition (using ICP and OES by Medac Ltd., UK), given in Table 8.1, show that the samples have the expected abundance of the constituent atoms and densities that are consistent with other comparable phosphate-based glasses.

Sample Identifier	ZnO / mol% (Batch value)	Compositional Analysis / at% (± 0.1)						Density / gcm^{-3} (± 0.05)
		P	Ca	Na	Ti	Zn	O	
T5Z5	5	21.3	5.1	6.8	1.1	1.1	64.8	2.66
T5Z3	3	21.3	5.7	6.6	1.2	0.7	65.3	2.66
T5Z1	1	21.4	6.0	6.6	1.1	0.2	65.2	2.62

Table 8.1: Sample characterisation for glasses of general composition $(\text{P}_2\text{O}_5)_{50}(\text{CaO})_{30-x}(\text{Na}_2\text{O})_{20}(\text{TiO}_2)_5(\text{ZnO})_x$.

X-ray Absorption Spectroscopy (XAS)

The data were collected on Station 9.3 at the Synchrotron Radiation Source at the Daresbury Laboratory, UK. The samples were ground to a fine powder and mixed with polyvinylpyrrolidone (PVP) and pressed into 13 mm pellets. The instrument was set to record in transmission mode at the Zn K-edge. Three ionisation chambers were used to record the incident, transmitted, and calibrant beam intensities. The sample

pellet was placed in an aluminium holder between the first and second ion chambers. The beam dimensions were 5×1 mm at the sample. A $5 \mu\text{m}$ zinc foil was placed between the second and third ion chambers so that the absorption spectrum of the foil was recorded simultaneously. The edge position of the foil was used to calibrate each scan and was set to 9.66 keV [7]. In addition to data from the three zinc containing glasses, five zinc based references (ZnO , $\text{Zn}_3(\text{PO}_4)_2$, $\text{CaZn}_2(\text{PO}_4)_2$, $\text{Zn}(\text{SO}_4)_2 \cdot \text{H}_2\text{O}$ and $\text{Zn}(\text{NO}_3)_2 \cdot 6\text{H}_2\text{O}$) were run for comparison. The EXAFS oscillations were fitted using Equation 2.37 in *EXCURV98*. $A(k)$ was determined to be 0.66 by fitting the ZnO standard. The model ZnO structural parameters were taken from Grandjean *et al.* [7].

High Energy X-ray Diffraction

The data were collected on Station 9.1 at the Synchrotron Radiation Source at the Daresbury Laboratory, UK. The instrument was set up to collect data in theta-two theta geometry with a 12×1 mm beam of monochromatic ($\lambda = 0.458 \text{ \AA}$, $E = 25.514$ keV) X-rays incident on the sample. The sample holders were aluminium disks of thickness 0.5 mm. The glass was ground into a fine powder and was packed into a 15×5 mm rectangular cut-out in the sample holder. The sample was held in place by a thin layer of Kapton on the front and back faces of the holder.

Neutron Diffraction

The data presented here were collected on the GEM diffractometer at the ISIS Pulsed Neutron Facility at the Rutherford Appleton Laboratory, UK [8]. The solid glass rods were mounted on a sample holder and placed directly in the neutron beam, which was trimmed to 40×15 mm. Time-of-flight data were collected over a large Q -range (up to 50 \AA^{-1}). The program *Gudrun* [9] was used to perform corrections and data reduction.

8.3 Results

Zinc is typically found in 4- or 6-fold coordination environments. 5-fold is less common because zinc has a $d^{10}s^2$ electronic configuration which means that the chemical bonds are generally isotropic and ZnO_x polyhedra are spherically symmetric [10]. Figure 8.1 shows the XANES spectra for all samples along with the $\text{CaZn}_2(\text{PO}_4)_2$ standard, which is an example of a compound that exhibits a mixed zinc environment

[11]. Spectra are also shown for ZnO and Zn(NO₃)₂, which are examples of 4- and 6-fold zinc environments respectively. CaZn₂(PO₄)₂ bears the most similarity to the spectra from the glasses, which implies that these samples also have mixed zinc sites. It should be noted that the standards are crystalline in nature and the features tend to be better defined than for amorphous materials. No change in the zinc environment was observed with varying zinc concentration.

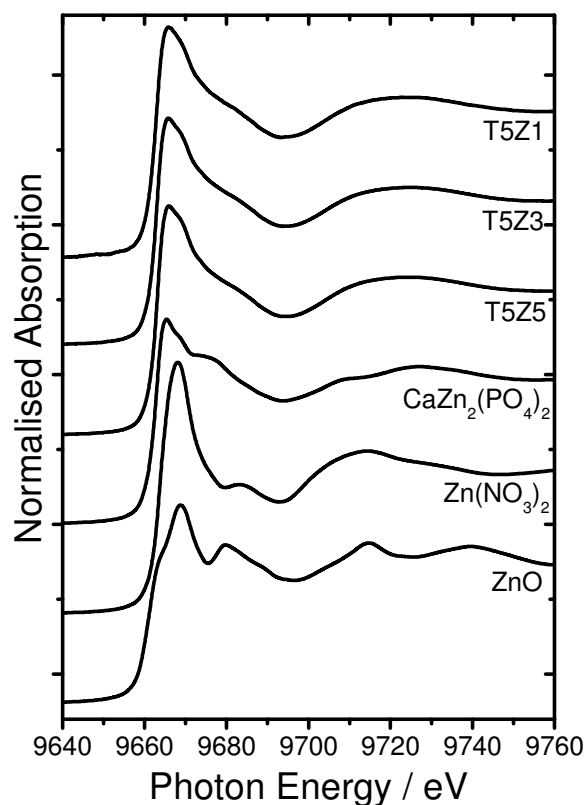


Figure 8.1: Zn K-edge XANES spectra. The spectra for ZnO (4-fold), Zn(NO₃)₂ (6-fold) and CaZn₂(PO₄)₂ (mixed) are also shown for comparison.

Figure 8.2 shows the EXAFS spectrum for sample T5Z5 with associated simulation produced from Equation 2.37. The real space representation shows two peaks at ~1.95 and ~3.1 Å. These correspond to the first and second nearest neighbours. Table 8.2 summarises the results for each sample. The radial distances obtained for the Zn-O shells are consistent with zinc occupying a tetrahedral environment [12, 13]. The large error allows the Zn-O coordination number to be as low as 4.9, which supports the possibility of site mixing, as inferred by XANES.

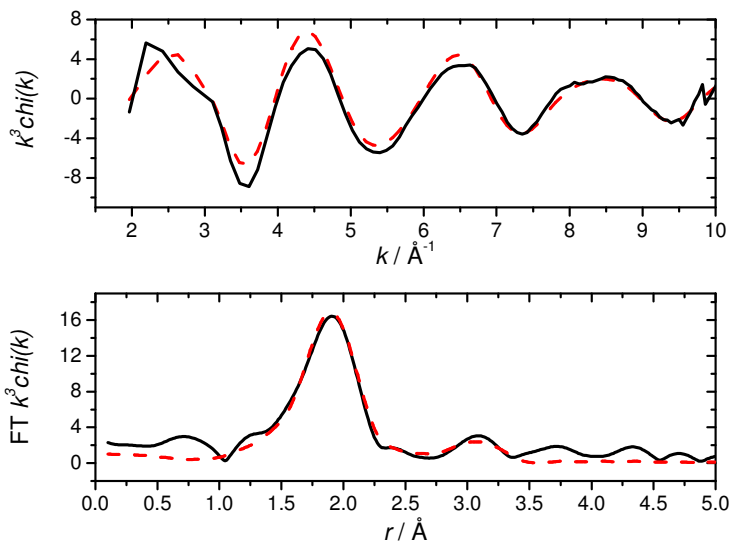


Figure 8.2: EXAFS spectrum for sample T5Z5 (solid) and simulation (dashed).

Sample Identifier	Neighbour	Radial Distance / Å	Coordination Number ($\pm 20\%$)	D/W Factor / Å ²
ZnO	O	1.96(1)	3.9	0.008(1)
	Zn	3.22(1)	12.0	0.018(2)
	O	3.75(3)	9.2	0.014(2)
	Zn	4.57(5)	7.1	0.018(4)
T5Z5	O	1.95(2)	6.2	0.016(2)
	P	3.11(4)	1.1	0.009(3)
T5Z3	O	1.94(2)	6.1	0.017(2)
	P	3.09(4)	1.0	0.009(3)
T5Z1	O	1.95(2)	6.3	0.016(2)

Table 8.2: Structural parameters obtained by fitting the Zn K-edge EXAFS spectra. The second nearest neighbour parameters could not be determined for sample T5Z1 owing to the exceptionally low concentration of zinc atoms. The numbers given in parentheses are the uncertainty in the final decimal place.

The X-ray and neutron $i(Q)$ are shown in Figure 8.3. The respective $T(r)$ were produced by Fourier inversion of $i(Q)$. In this case the Lorch function was applied to

both the X-ray and neutron $i(Q)$ data and a maximum Q value of 23 \AA^{-1} was used in the Fourier transform.

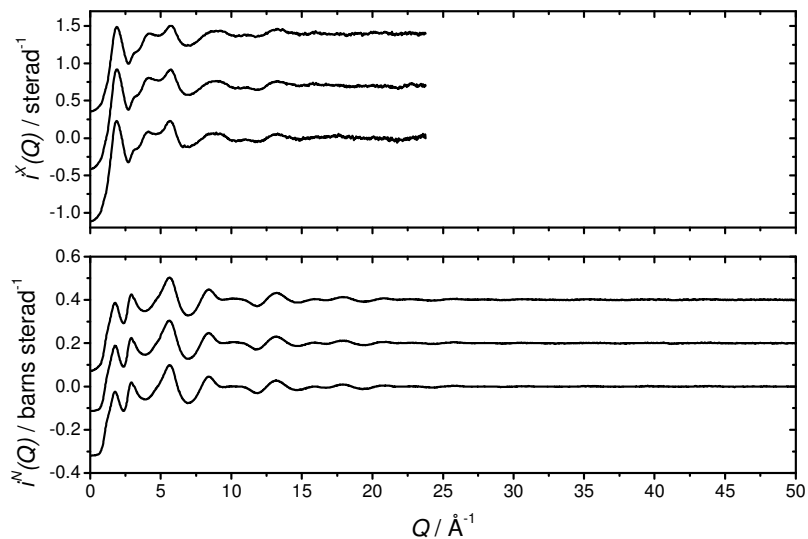


Figure 8.3: X-ray ($i^X(Q)$) and neutron ($i^N(Q)$) interference functions for samples T5Z1, T5Z3 and T5Z5 (bottom to top).

Figure 8.4 shows the results of co-fitting the X-ray and neutron diffraction data for sample T5Z5. Owing to the large number of overlapping correlations at $r > \sim 2.7 \text{ \AA}$, these data have only been fitted up to the first O...O distance and it would be difficult to justify any further correlations beyond this point. Computational modelling and/or other experimental techniques may help to elucidate the atomic arrangement at longer r values. It can be seen from Figure 8.4 that the fit to the first peak in the X-ray and neutron $T(r)$ do not agree particularly well. The origin of this disparity is believed to be in the normalisation of the X-ray data and is prominent where there is significant variation in the atomic number of the elements composing the sample as previously discussed in Chapter 6.

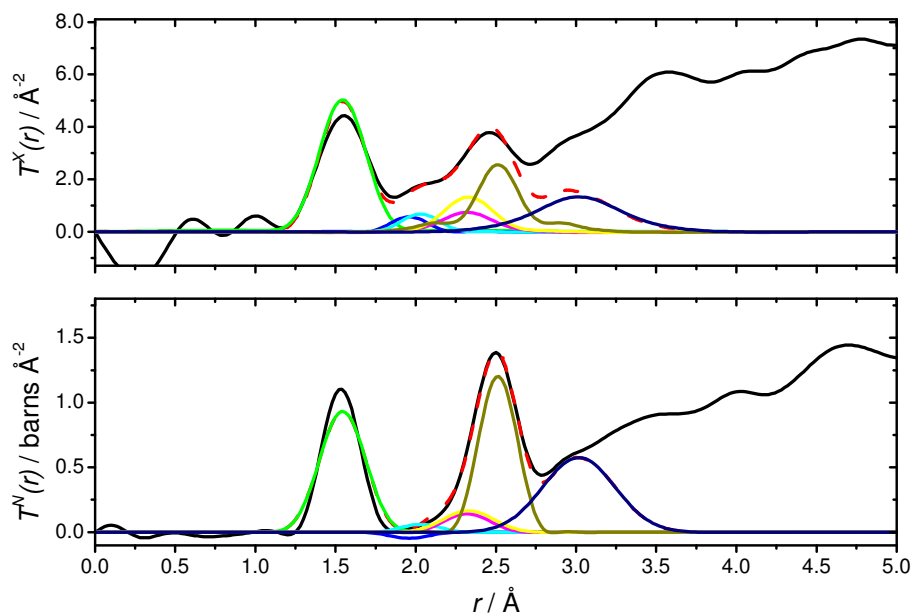


Figure 8.4: Fit (red dashed) to X-ray (top) and neutron (bottom) $T(r)$ (black) produced by refining the input parameters. Correlations from left to right: P-O (green), Ti-O (blue), Zn-O (cyan), Na-O (magenta), Ca-O (yellow), O...O (olive) and O...O (navy).

The structural parameters obtained by co-fitting the data are given in Table 8.3. It should be noted that the O...O correlation shown in light grey is performing the role of background filler as described in Chapter 5 and the structural parameters reported for this correlation should be ignored. Furthermore, the model presented here is just one possibility that is consistent with current theory and bond valence calculations (see later). Given the number of correlations involved with such a complex material, there are undoubtedly a number of other combinations of parameters that could be used to fit the data. The starting parameters used in the fitting process were derived from the results in Chapter 5 and various studies of similar materials in the literature.

Sample Identifier	Correlation	R / Å (± 0.02)	N (± 0.2)	σ / Å (± 0.02)
T5Z5	P-O	1.54	4.0	0.11
	Ti-O	1.96	6.0	0.07
	Zn-O	2.03	5.0	0.08
	Na-O	2.32	4.0	0.11
	Ca-O	2.33	5.4	0.13
	O··O	2.51	4.0	0.07
	O··O	3.02	4.5	0.21
T5Z3	P-O	1.54	4.0	0.11
	Ti-O	1.96	6.0	0.07
	Zn-O	2.03	5.0	0.08
	Na-O	2.33	4.0	0.11
	Ca-O	2.33	5.4	0.13
	O··O	2.52	4.0	0.07
	O··O	3.01	4.0	0.19
T5Z1	P-O	1.55	4.0	0.11
	Ti-O	1.96	6.0	0.08
	Zn-O	2.03	5.0	0.08
	Na-O	2.34	4.0	0.11
	Ca-O	2.35	5.4	0.13
	O··O	2.52	4.0	0.08
	O··O	2.99	4.1	0.19

Table 8.3: Optimised structural parameters output by *NXFit* upon co-fitting X-ray and neutron diffraction data. Parameters have been rounded to a suitable number of decimal places.

8.4 Discussion

Distinguishing the differences between the zinc/titanium containing samples was difficult because of the limited range of compositions studied here. The discussion is primarily about the variation between the structure of these samples and the ternary $(\text{P}_2\text{O}_5)_{50}(\text{CaO})_{30}(\text{Na}_2\text{O})_{20}$ glass investigated in Chapter 5.

The parameters in Table 8.3 describe the atomic arrangement derived from the diffraction experiments. The P-O correlation refers to the first prominent peak in $T(r)$. The average P-O distance, coordination number and disorder parameter do not vary as a function of composition and these parameters compare well with the results derived in Chapter 5 for the ternary calcium sodium metaphosphate glass, indicating that the addition of zinc and titanium does not cause any disruption of the P-O bonding. The

accuracy of these parameters is limited by the aforementioned problem with the normalisation of the X-ray data. Fortunately it has been possible to elucidate the contribution of P-NBO and P-BO to the P-O correlation using the neutron data alone. Figure 8.5 shows $T^N(r)$ over the range of 1.0-2.0 Å using a maximum Q value of 50 Å⁻¹ in the Fourier transform.

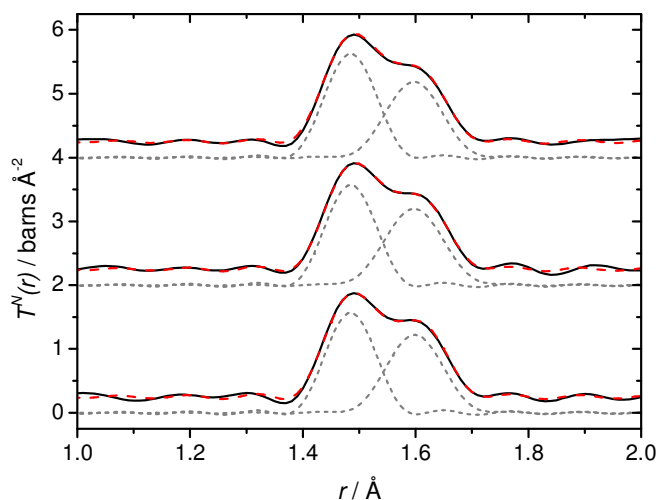


Figure 8.5: $T^N(r)$ for samples T5Z1, T5Z3 and T5Z5 (bottom to top) with corresponding fits relating to the P-NBO (left) and P-BO (right) contributions. The data, fits and partials have been off-set for clarity.

The results of fitting the P-NBO and P-BO correlations are shown in Table 8.4. In these samples some variation in the P-O bonding may be expected on the strength of the ³¹P NMR results [6] and on the basis of the mixture of modifying cations in the sample. However, no variation is seen in the P-NBO and P-BO distribution, which can be taken as being equal within the error of the experiment, indicating that the network is predominantly formed of Q² phosphate units, again in agreement with Chapter 5. It is suggested that the concentration of Q¹ and Q³ species is too low to have an observable effect and that the result of adding zinc and titanium to the ternary glass does not have a significant effect on the P-NBO/P-BO splitting (see Figure 1.4 and related text) and cannot be observed using this technique.

Sample Identifier	Correlation	R / Å (± 0.01)	N (± 0.1)	σ / Å (± 0.01)
T5Z5	P-NBO	1.48	2.1	0.04
	P-BO	1.60	1.8	0.05
T5Z3	P-NBO	1.48	2.0	0.04
	P-BO	1.60	1.9	0.05
T5Z1	P-NBO	1.48	1.9	0.04
	P-BO	1.60	1.9	0.05

Table 8.4: Optimised parameters determined by fitting the P-NBO and P-BO contributions to the first peak in $T^V(r)$.

The O··O correlation at 2.52 Å is due to oxygen atoms surrounding phosphorus. Using the interatomic distances, the O-P-O angle can be calculated as 109.8° and the P-O-P angles as 138.5°, in exact agreement with the ternary glass.

The second and third correlations in Table 8.3 refer to the TiO_x and ZnO_x polyhedra. The interatomic distances are consistent with zinc and titanium containing phosphates (*e.g.* TiP₂O₇ and NaZn(PO₃)₃) [12]. The results suggest that, on average, each titanium atom is surrounded by six NBOs; consistent with the work of Pickup *et al.* [14] where Ti K-edge XANES were recorded for a range of (P₂O₅)-(CaO)-(Na₂O)-(TiO₂) glasses. The Ti K-edge XANES can be used to directly determine the titanium coordination [15, 16] and the results of Pickup *et al.* showed that the titanium formed TiO₆ polyhedra; a configuration that did not demonstrate any compositional dependence.

The Zn-O parameters in Table 8.3 suggest that each zinc atom is coordinated by five NBOs in agreement with Musinu *et al.* [17, 18]. However, as previously mentioned, this is not a desirable configuration for zinc. In glasses such as these it is expected that the zinc occupies a 4-fold coordination environment; a structure supported by much experimental evidence [13, 19-22]. It is likely that the zinc coordination number given here represents the average over all ZnO_x polyhedra, implying the presence of mixed zinc sites as inferred by the XANES and EXAFS results. The apparent site mixing, and hence deviation away from the expected tetrahedral coordination, may be important in the context of the low Zn²⁺ release rate observed by Abou Neel *et al.* [6] but this would require further investigation.

No change is seen in the Na-O environment between the samples, or compared to the ternary glass. This is in good agreement with the ^{23}Na NMR results reported in Abou Neel *et al.* [6]. There is a small decrease in the calcium coordination compared to the ternary glass, which is accommodated by a reduction in the mean interatomic Ca-O distance. This reduction is probably due to the requirement for titanium to be coordinated by six NBOs.

The M-O parameters can be justified in terms of the bond valence calculation introduced in Chapter 5 (see Equation 5.3). Using the values from Brese and O'Keefe [23] for $r_{\text{Ca-O}} = 1.97 \text{ \AA}$, $r_{\text{Na-O}} = 1.80 \text{ \AA}$, $r_{\text{Ti-O}} = 1.82 \text{ \AA}$ and $r_{\text{Zn-O}} = 1.70 \text{ \AA}$ the total valence neutralised by the surrounding NBOs can be determined and are shown in Table 8.5. In all cases the M-NBO bond valence compares well with the nominal valence required by each metal cation.

Modifying ion	Valence neutralised by neighbouring NBOs		
	T5Z5	T5Z3	T5Z1
Ca^{2+}	2.02	2.02	1.92
Na^+	0.98	0.94	0.93
Ti^{4+}	4.05	4.05	4.05
Zn^{2+}	2.07	2.07	2.07

Table 8.5: Cation valence neutralised in each MO_x polyhedra.

The M-O relationship can be investigated in more detail by converting the M-O coordination number ($N_{\text{M-O}}$) into the O-M ($N_{\text{O-M}}$) via Equation 8.1:

$$c_M N_{\text{M-O}} = c_O N_{\text{O-M}} \quad 8.1$$

where c_M and c_O are the relative concentrations of metal and oxygen respectively. Equation 8.1 is derived directly from Equation 3.13. Table 8.6 shows $N_{\text{O-M}}$ based on the parameter in Table 8.3 for sample T5Z5.

M	c_M	c_O	N_{M-O}	N_{O-M}
Ti	0.011	0.649	6.0	0.102
Zn	0.011	0.649	5.0	0.085
Na	0.064	0.649	4.0	0.394
Ca	0.053	0.649	5.4	0.441

Table 8.6: Results for the conversion of N_{M-O} to N_{O-M} for each type of metal (M) in sample T5Z5.

The total $N_{O-M} = 1.022$ (given by the sum of the final column in Table 8.6) meaning that, on average, each oxygen is coordinated by one metal. It is assumed Ms are not coordinated by BOs, which is a reasonable assumption given that the repulsion due to the two P^{5+} bonded to each BO would make such a bond energetically unfavourable [24]. With this assumption in mind N_{O-M} should be converted to N_{NBO-M} using Equation 8.2.

$$N_{O-M} = \frac{c_{BO}N_{BO-M} + c_{NBO}N_{NBO-M}}{c_O} \quad 8.2$$

where c_{BO} and c_{NBO} are the relative concentrations of BOs and NBOs respectively. Using the assumption outlined above $N_{BO-M} = 0$. Given that the structure is predominantly constructed of Q^2 units, each phosphorus has one BO such that $c_{BO} = c_P$ and $c_{NBO} = c_O - c_{BO}$. By rearrangement of Equation 8.2, N_{NBO-M} is calculated as 1.5, meaning that 50% of NBOs are coordinated to two Ms and 50% are coordinated to just one. The sharing of NBOs by M atoms means that the MO_x polyhedra are not isolated and $M \cdots M$ correlations are expected in $T(r)$ beyond the $O \cdots O$ peak at 2.52 Å. By comparison, N_{NBO-M} for the ternary glass is 2.2, which implies that all NBOs neighbour at least two M atoms.

This result is, perhaps, the best justification for not fitting $T(r)$ beyond ~ 2.7 Å, where the total number of overlapping $M \cdots M$ correlations is expected to be large and could not be fitted with any confidence. This region of $T(r)$ is also complicated by the presence of $P \cdots M$ correlations at slightly longer distances ($r > \sim 3.4$ according to the RMC in Chapter 5). Calculations for samples T5Z3 and T5Z1 give the same result and lead to the same conclusions.

8.5 Conclusions

No variation was observed in the P-NBO and P-BO correlations and the existence of Q^1 and Q^3 units could not be verified. However, the proportion of Q^1 and Q^3 species reported by the ^{31}P NMR was $< 10\%$ [6] so the overall effect on the P-O bonding is possibly less than the smallest detectable variation.

The metal cations influence the network and adapt their local environment to satisfy their own valence. The cations with the highest valence have more influence on the network and pull NBOs into the required coordination geometry. This is observed in terms of titanium, where it always manipulates the NBOs into TiO_6 octahedra. The “greedy” nature of titanium probably explains the apparent decrease in the Ca-O coordination compared to the ternary glass. The next most influential cations are zinc and calcium, both being divalent. Interestingly, the zinc cations tend to form ZnO_x polyhedra, while the calcium forms CaO_5 and CaO_6 polyherda. The least influential cation is sodium, which is usually flexible in its coordination, ranging from four to six [20, 22, 25-28]. However, no variation in the sodium coordination was observed; a result consistent with ^{23}Na NMR [6]. On this basis it could be concluded that sodium does not coordinate with less than four NBOs in this type of material. If this is the case it would lend extra support for the suggestion that zinc is forced into mixed geometries. What is not clear is why the zinc cations do not give up some NBOs to the calcium and sodium so that it can occupy its preferential tetrahedral coordination environment. Abou Neel *et al.* [6] report that the zinc release rate decreases upon addition of titanium and concluded that the titanium is having a profound effect on the whole network forming P-O-Ti bonds. This could not be verified in this study but it is suggested that the titanium environment could be investigated more accurately by a Ti K- and L-edge XAS study of these materials, which would be sensitive to perturbations of the first and second coordination shells and therefore yield information about the coherence of the Ti-P correlations.

8.6 References

- [1] E. A. Abou Neel and J. C. Knowles, *J. Mater. Sci.: Mater. Med.* **19** (2008), p. 377.
- [2] D. M. Pickup, E. A. Abou Neel, R. M. Moss, K. M. Wetherall, P. Guerry, M. E. Smith, J. C. Knowles and R. J. Newport, *J. Mater. Sci.: Mater. Med.* **19** (2008), p. 1681.
- [3] E. A. Abou Neel, W. Chrzanowski and J. C. Knowles, *Acta Biomater.* **4** (2008), p. 523.
- [4] E. A. Abou Neel, L. A. O'Dell, M. E. Smith and J. C. Knowles, *J. Mater. Sci.: Mater. Med.* **19** (2008), p. 1669.
- [5] V. Salih, A. Patel and J. C. Knowles, *Biomed. Mater.* **2** (2007), p. 11.
- [6] E. A. Abou Neel, L. A. O'Dell, W. Chrzanowski, M. E. Smith and J. C. Knowles, *J. Biomed. Mater. Res., Part B* **89B** (2008), p. 392.
- [7] D. Grandjean, H. L. Castricum, J. C. van den Heuvel and B. M. Weckhuysen, *J. Phys. Chem. B* **110** (2006), p. 16892.
- [8] A. C. Hannon, *Nucl. Instrum. Methods Phys. Res., Sect. A* **551** (2005), p. 88.
- [9] S. E. McLain, D. T. Bowron, A. C. Hannon and A. K. Soper, GUDRUN, A computer program developed for analysis of neutron diffraction data., (2006).
- [10] G. Sarret, A. Manceau, L. Spadini, J. C. Roux, J. L. Hazemann, Y. Soldo, L. Eybert-Berard and J. J. Menthonnex, *Environ Sci Technol* **32** (1998), p. 1648.
- [11] R. J. B. Jakeman and A. K. Cheetham, *J Am Chem Soc* **110** (1988), p. 1140.
- [12] D. A. Fletcher, R. F. McMeeking and D. Parkin, *J. Chem. Inf. Comput. Sci.* **36** (1996), p. 746.
- [13] U. Hoppe, *J. Non-Cryst. Solids* **195** (1996), p. 138.
- [14] D. Pickup, E. Abou Neel, R. Moss, K. Wetherall, P. Guerry, M. Smith, J. Knowles and R. Newport, *J. Mater. Sci.: Mater. Med.* **19** (2008), p. 1681.
- [15] F. Farges, G. E. Brown and J. J. Rehr, *Phys. Rev. B* **56** (1997), p. 1809.
- [16] G. A. Waychunas, *Am. Mineral.* **72** (1987), p. 89.
- [17] A. Musinu, G. Paschina, G. Piccaluga and G. Pinna, *J. Non-Cryst. Solids* **177** (1994), p. 97.
- [18] A. Musinu, G. Piccaluga, G. Pinna, D. Narducci and S. Pizzini, *J. Non-Cryst. Solids* **111** (1989), p. 221.

- [19] M. Bionducci, G. Licheri, A. Musinu, G. Navarra, G. Piccaluga and G. Pinna, *Z. Naturforsch.* **51** (1996), p. 1209.
- [20] R. K. Brow, *J. Non-Cryst. Solids* **263** (2000), p. 1.
- [21] U. Hoppe, G. Walter and D. Stachel, *Phys. Chem. Glasses* **33** (1992), p. 216.
- [22] U. Hoppe, D. Stachel and D. Beyer, *Phys. Scr.* **T57** (1995), p. 122.
- [23] N. E. Brese and M. O'Keeffe, *Acta Crystallogr.* **B47** (1991), p. 192.
- [24] K. M. Wetherall, D. M. Pickup, R. J. Newport and G. Mountjoy, *J. Phys.: Condens. Matter* **21** (2009), 035109.
- [25] U. Hoppe, G. Walter, R. Kranold and D. Stachel, *J. Non-Cryst. Solids* **263** (2000), p. 29.
- [26] D. M. Pickup, I. Ahmed, P. Guerry, J. C. Knowles, M. E. Smith and R. J. Newport, *J. Phys.: Condens. Matter* **19** (2007), 415116.
- [27] A. Speghini, E. Sourial, T. Peres, G. Pinna, M. Bettinelli and J. A. Capobianco, *Phys. Chem. Chem. Phys.* **1** (1999), p. 173.
- [28] A. Hall, J. Swenson, C. Karlsson, S. Adams and D. T. Bowron, *J. Phys.: Condens. Matter* **19** (2007), 415115.

Chapter 9 – Summary

9.1 Further Work

The most interesting feature that requires further investigation is the apparent disagreement between the X-ray and neutron diffraction data when co-fitting the P-O peak. This disparity was observed in both the silver and the zinc/titanium doped phosphate glasses and was particularly noticeable in samples containing higher concentrations of heavier modifiers. It is suggested that this feature may result from the normalisation of the X-ray data, but this remains as a tentative hypothesis. This phenomenon should be investigated more fully in the future to determine its origin.

In terms of data analysis and fitting, future work should make use of a consistent definition of $T(r)$. It is recommended that the generic definition given in Equation 4.6 is used, thus giving $T^X(r)$ and $T^N(r)$ the same units and making them directly comparable.

This has implications for the fitting program *NXFit*, which should be modified to accommodate this definition. Future versions of *NXFit* should also output errors per parameter based on some statistical analysis of the fit. However, a method by which this could be achieved has not been investigated. Furthermore, it is suggested that the Fourier transform of the data be done internally to ensure that the process is wholly self-consistent, such that the program should accept $i(Q)$ (or $S(Q)-1$) as the input.

In terms of the materials studied, titanium XAS measurements should be done on the zinc/titanium phosphate glasses to elucidate the local environment of the TiO_x polyhedra. A further investigation should be conducted to determine if the zinc site mixing has any effect on the biomedical properties of these glasses. In the silver doped glasses the CaO_x polyhedra seems to move from being fairly regular to being slightly more distorted with the addition of silver, which correlates with a decrease in the Ca^{2+} release rate. It is proposed that this feature could also be investigated in more detail.

9.2 Conclusions

Computational code development – NXFit

A program has been created that allows an unlimited number of pair correlations to be fitted to experimental diffraction data – specifically to both neutron and X-ray diffraction simultaneously. The program utilises the Nelder-Mead simplex method to optimise a set of “best guess” parameters. The Nelder-Mead algorithm is a robust method to search N -dimensional parameter space for an optimal solution. Constraints are applied in the form of a wrapper function that performs a sinusoidal parameter transform; keeping the optimised parameters between user-defined upper and lower bounds.

The code is going to be packaged and made available to a wider user group through the ISIS Pulsed Neutron Facility, UK.

Calcium sodium phosphate glass

All the samples investigated in this study are adaptations of the base composition $(\text{P}_2\text{O}_5)_{50}(\text{CaO})_{30}(\text{Na}_2\text{O})_{20}$. A thorough investigation of this glass has revealed some interesting structural features, which were further elucidated by reverse Monte Carlo modelling and co-fitting of X-ray and neutron diffraction data.

An RMC model was built to simulate the glass structure and showed that calcium and sodium are coordinated by 6.1 and 4.3 NBOs respectively, which was also confirmed by the X-ray and neutron diffraction data. In the study of $(\text{P}_2\text{O}_5)_{50}(\text{CaO})_{50}$ by Wetherall *et al.* the calcium coordination was found to exhibit short and long Ca-O distances; a feature that was not reciprocated in the ternary glass system. The Ca- and Na-O environments were ratified by the results of a valence calculation based on the M-O distance and coordination number. The RMC results were also used to show that 60% of the NBOs are shared between adjacent MO_x polyhedra; giving rise to $\text{M}\cdots\text{M}$ correlations.

The P-O and $\text{O}\cdots\text{O}$ correlations provided information about the underlying host network, which is consistent with interconnected PO_4^{3-} units forming long chains and rings. Closer inspection of the P-O peak in the experimental data revealed that it was

composed of contributions from P-NBO and P-BO correlations, consistent with a structure composed wholly of Q^2 phosphate units. The average O-P-O and P-O-P angles were found to be 109.8° and 138.5° respectively, in agreement with many other studies of metaphosphate glasses.

Silver calcium sodium phosphate glass

An NDIS study has been conducted using the two silver isotopes ^{107}Ag and ^{109}Ag to elucidate the local environment of silver in $(\text{P}_2\text{O}_5)_{50}(\text{CaO})_{30}(\text{Na}_2\text{O})_{10}(\text{Ag}_2\text{O})_{10}$ glass. The Ag^+ ions occupy a highly distorted octrahedral environment; a conclusion supported by Ag K-edge XANES. A process of disproportionation of the Q^n species (*i.e.* $2Q^2 \rightarrow Q^1 + Q^3$) was proposed on the strength of the NDIS diffraction results to account for the observed variation in Ag^+ release rate with silver content.

Further investigation of the structure of these materials by total neutron and X-ray diffraction over a range of compositions confirms the existence of AgO_6 polyhedra with a large variation in the Ag-O interatomic distances. Calcium and sodium form coordination geometries consistent with other metaphosphate glasses. The calcium environment appears to move from a fairly regular arrangement to a significantly more distorted structure upon the addition of silver. This trend seems to correlate with an observed decrease in Ca^{2+} release rate with increasing silver concentration. Deeper analysis of the P-O bonding elucidates the contribution from P-NBO and P-BO correlations. No variation is observed with composition and the structure seems to be composed predominantly of Q^2 units. However, the possibility of some disproportionation is not wholly ruled out since a ^{31}P NMR study reveals the presence of Q^1 and Q^3 units.

RMC models of these glasses reveal calcium and silver coordination numbers that are lower than expected. It is suggested that the constraints (necessarily imposed on these models) were too strict and did not allow enough flexibility in the underlying phosphate network bonding and/or connectivity.

Zinc titanium calcium sodium phosphate glass

X-ray and neutron diffraction data have been co-fitted to elucidate the structure of these complex glasses. Correlations have been fitted to simulate the P-O bonding and

the M-O coordination geometry over the compositional range of $(\text{P}_2\text{O}_5)_{50}(\text{CaO})_{30-x}(\text{Na}_2\text{O})_{15}(\text{TiO}_2)_5(\text{ZnO})_x$ for $x = 1, 3$ and 5 mol%.

The parameters relating to the P-O bonding suggest that the structure is predominantly composed of Q^2 units. This is as expected for these near-metaphosphate glasses with $[\text{O}]/[\text{P}] = 3.05$. The first $\text{O}\cdots\text{O}$ correlation is used to confirm the tetrahedral arrangement of the phosphate units.

The M-O coordination environment is investigated and shows no variation across the small compositional range studied. The titanium ions form TiO_6 polyhedra and have a mean interatomic separation of ~ 1.96 Å. On average, the zinc ions reside in a 5-fold coordinated environment, but this is not typically arrangement for zinc polyhedra. Instead, it is proposed that the Zn^{2+} ions occupy mixed sites; a result that is supported by Zn K-edge XAS measurements. The calcium ions occupy 5- and 6-fold sites, which represents a small reduction in coordination compared to the ternary P_2O_5 -CaO- Na_2O metaphosphate glass. This is explained in terms of the ionic valences, where Ti^{4+} preferentially satisfies its own coordination requirement before the divalent Ca^{2+} and Zn^{2+} , which share the remaining NBOs. The sodium ions appear to occupy 4-fold coordination geometries across all compositions and it is proposed that this is the minimum number of NBOs that sodium coordinates with in these types of material. The unchanging sodium environment is supported by ^{23}Na NMR results. The M-O mean interatomic distances and coordination numbers have been shown to be consistent with bond valence calculations.

The O-M coordination has also been considered and analysis shows that each NBO is coordinated to 1.5 Ms, meaning that 50% of the NBOs are coordinated to two metal ions. This results shows that the MO_x polyherdra are not isolated; giving rise to $\text{M}\cdots\text{M}$ correlations.

Appendix A – MATLAB Code: NXFit_v4

Here follows the *MATLAB* code for *NXFit_v4*, which is the version of *NXFit* used to produce the fits shown in this thesis. However a newer version, *NXFit_RI* (release 1), is now available. The code for *RI* is thoroughly commented and is written in a more modular fashion so it is more accessible and can be modified by other programmers in the future. *RI* also includes some of the improvements discussed in Chapter 4 and it is this version that will be compiled and distributed through ISIS in the near future.

Code:

```
function NXFit_v4

% This program is used to fit ND and XRD data on their own or together.
% Correctly constructed files must be used to obtain the correct parameters
% for the optimisation process. It is also necessary to know some fit
% parameters that were used during the FT steps to ensure the correct
% resolution is obtained. There is no need to factor in a correction for
% peak broadening because the fit is constructed in Q-space and then FT to
% match the real-space correlation function.
%
% Version information
% v4 - writes the pair correlations to a workspace array and allows the
%     user to display in a separate window
%     - output fit files now have new columns
%       [x y yfit cor1 cor2 ... corN] for both X and N fits
% v3 - includes a box to change the number of iterations
%     - resize capability
%     - close request dialogue box
% v2 - preallocated matrix in fitting process
% v1 - first implementation of joint XRD and ND fitting with GUI

hMain=[]; MainRoot=matlabroot; DataPath=MainRoot(1:3);
figcolor=get(0,'defaultFigureColor');
global NCurveQ NCurveR Nr NTr NFitted_Tr XCurveQ XCurveR Xr XTr XFitted_Tr Dtype

hMain.fig = figure(...
    'Name','NXFit',...
    'NumberTitle','off', ...
    'Menubar','none',...
    'Toolbar','none',...
    'Resize','on',...
    'ResizeFcn',@FigResize,...
    'CloseRequestFcn',@CloseRequest,...
    'Position',[75,75,1300,750]);

%-----
%-----

% This defines the first panel that deals with X-ray diffraction data

hMain.Panel(1) = uipanel(...
    'Parent',hMain.fig,...
    'BackgroundColor',figcolor,...
    'Units','pixels',...
    'ResizeFcn',@FigResize,...
    'Position',[10,570,640,170],...
    'Title','X-ray Data');

hMain.X.Text(1) = uicontrol(...
    'Parent',hMain.Panel(1),...
    'BackgroundColor',figcolor,...
    'Units','pixels',...
```

```

'Position', [40, 130, 200, 20], ...
'HorizontalAlignment', 'left', ...
'Style', 'text', ...
'String', 'X-ray data file');

hMain.X.Tick = uicontrol(...
'Parent', hMain.Panel(1), ...
'BackgroundColor', figcolor, ...
'Units', 'pixels', ...
'Position', [12, 116, 20, 20], ...
'HorizontalAlignment', 'left', ...
'Style', 'checkbox', ...
'Value', 0, ...
'Callback', @DTypeChange);

hMain.X.FileName(1) = uicontrol(...
'Parent', hMain.Panel(1), ...
'BackgroundColor', figcolor, ...
'Units', 'pixels', ...
'Position', [40, 115, 500, 20], ...
'HorizontalAlignment', 'left', ...
'BackgroundColor', 'w', ...
'Style', 'edit', ...
'Enable', 'off');

hMain.X.Browse(1) = uicontrol(...
'Parent', hMain.Panel(1), ...
'BackgroundColor', figcolor, ...
'Units', 'pixels', ...
'Position', [555, 115, 70, 20], ...
'HorizontalAlignment', 'left', ...
'String', 'Browse', ...
'Style', 'pushbutton', ...
'Enable', 'off', ...
'Callback', @Browse);

hMain.X.SubPanel(1) = uibuttongroup(...
'Parent', hMain.Panel(1), ...
'BackgroundColor', figcolor, ...
'Units', 'pixels', ...
'ResizeFcn', @FigResize, ...
'Position', [40, 53, 220, 50], ...
'Title', 'X-ray Window Function', ...
'Tag', 'H', ...
'SelectionChangeFcn', @MtypeChange);

hMain.X.Radio(1) = uicontrol(...
'Parent', hMain.X.SubPanel(1), ...
'BackgroundColor', figcolor, ...
'Units', 'pixels', ...
'Position', [11, 4, 66, 30], ...
'HorizontalAlignment', 'left', ...
'String', 'Lorch', ...
'Style', 'radiobutton', ...
'Value', 0, ...
'Enable', 'off', ...
'Tag', 'L');

hMain.X.Radio(2) = uicontrol(...
'Parent', hMain.X.SubPanel(1), ...
'BackgroundColor', figcolor, ...
'Units', 'pixels', ...
'Position', [81, 4, 66, 30], ...
'HorizontalAlignment', 'left', ...
'String', 'Hanning', ...
'Style', 'radiobutton', ...
'Value', 1, ...
'Enable', 'off', ...
'Tag', 'H');

hMain.X.Radio(3) = uicontrol(...
'Parent', hMain.X.SubPanel(1), ...
'BackgroundColor', figcolor, ...
'Units', 'pixels', ...
'Position', [165, 4, 50, 30], ...
'HorizontalAlignment', 'left', ...

```

```

'String', 'Step', ...
'Style', 'radiobutton', ...
'Value', 0, ...
'Enable', 'off', ...
'Tag', 'S');

hMain.X.SubPanel(2) = uipanel(...
'Parent', hMain.Panel(1), ...
'BackgroundColor', figcolor, ...
'Units', 'pixels', ...
'ResizeFcn', @FigResize, ...
'Position', [280, 53, 260, 50], ...
'Title', 'Data Specs');

hMain.X.SubText(1) = uicontrol(...
'Parent', hMain.X.SubPanel(2), ...
'BackgroundColor', figcolor, ...
'Units', 'pixels', ...
'Position', [10, 8, 70, 20], ...
'HorizontalAlignment', 'left', ...
'String', 'Q max', ...
'Style', 'text');

hMain.X.Qmax = uicontrol(...
'Parent', hMain.X.SubPanel(2), ...
'BackgroundColor', figcolor, ...
'Units', 'pixels', ...
'Position', [50, 10, 60, 20], ...
'HorizontalAlignment', 'center', ...
'BackgroundColor', 'w', ...
'String', '22.0', ...
'Style', 'edit', ...
'Enable', 'off');

hMain.X.SubText(2) = uicontrol(...
'Parent', hMain.X.SubPanel(2), ...
'BackgroundColor', figcolor, ...
'Units', 'pixels', ...
'Position', [130, 8, 70, 20], ...
'HorizontalAlignment', 'left', ...
'String', 'Weighting', ...
'Style', 'text');

hMain.X.Weight = uicontrol(...
'Parent', hMain.X.SubPanel(2), ...
'BackgroundColor', figcolor, ...
'Units', 'pixels', ...
'Position', [185, 10, 60, 20], ...
'HorizontalAlignment', 'center', ...
'BackgroundColor', 'w', ...
'String', '0.0', ...
'Style', 'edit', ...
'Enable', 'off', ...
'Callback', @DTypeChange);

hMain.X.Text(2) = uicontrol(...
'Parent', hMain.Panel(1), ...
'BackgroundColor', figcolor, ...
'Units', 'Pixels', ...
'Position', [40, 25, 200, 20], ...
'HorizontalAlignment', 'left', ...
'Style', 'text', ...
'String', 'X-ray scattering factor file');

hMain.X.FileName(2) = uicontrol(...
'Parent', hMain.Panel(1), ...
'BackgroundColor', figcolor, ...
'Units', 'pixels', ...
'Position', [40, 10, 500, 20], ...
'HorizontalAlignment', 'left', ...
'BackgroundColor', 'w', ...
'Style', 'edit', ...
'Enable', 'off');

hMain.X.Browse(2) = uicontrol(...
'Parent', hMain.Panel(1), ...

```

```

'BackgroundColor',figcolor,...
'Units','pixels',...
'Position',[555,10,70,20],...
'HorizontalAlignment','left',...
'String','Browse',...
'Style','pushbutton',...
'Enable','off',...
'Callback',@Browse);

% This defines the second panel that deals with the Neutron data

hMain.Panel(2) = uipanel(...
'Parent',hMain.fig,...
'BackgroundColor',figcolor,...
'Units','pixels',...
'Position',[10,395,640,170],...
'ResizeFcn',@FigResize,...
'Title','Neutron Data');

hMain.N.Text(1) = uicontrol(...
'Parent',hMain.Panel(2),...
'BackgroundColor',figcolor,...
'Units','Pixels',...
'Position',[40,130,200,20],...
'HorizontalAlignment','left',...
'Style','text',...
'String','Neutron data file');

hMain.N.Tick = uicontrol(...
'Parent',hMain.Panel(2),...
'BackgroundColor',figcolor,...
'Units','pixels',...
'Position',[12,116,20,20],...
'HorizontalAlignment','left',...
'Style','checkbox',...
'Value',0,...
'Callback',@DTypeChange);

hMain.N.FileName(1) = uicontrol(...
'Parent',hMain.Panel(2),...
'BackgroundColor',figcolor,...
'Units','pixels',...
'Position',[40,115,500,20],...
'HorizontalAlignment','left',...
'BackgroundColor','w',...
'Style','edit',...
'Enable','off');

hMain.N.Browse(1) = uicontrol(...
'Parent',hMain.Panel(2),...
'BackgroundColor',figcolor,...
'Units','pixels',...
'Position',[555,115,70,20],...
'HorizontalAlignment','left',...
'String','Browse',...
'Style','pushbutton',...
'Enable','off',...
'Callback',@Browse);

hMain.N.SubPanel(1) = uibuttongroup(...
'Parent',hMain.Panel(2),...
'BackgroundColor',figcolor,...
'Units','pixels',...
'ResizeFcn',@FigResize,...
'Position',[40,53,220,50],...
'Title','Neutron Window Function',...
'Tag','L',...
'SelectionChangeFcn',@MtypeChange);

hMain.N.Radio(1) = uicontrol(...
'Parent',hMain.N.SubPanel(1),...
'BackgroundColor',figcolor,...
'Units','pixels',...
'Position',[11,4,66,30],...
'HorizontalAlignment','left',...
'String','Lorch',...

```

```

'Style', 'radiobutton', ...
'Value', 1, ...
'Enable', 'off', ...
'Tag', 'L');

hMain.N.Radio(2) = uicontrol(...
'Parent', hMain.N.SubPanel(1), ...
'BackgroundColor', figcolor, ...
'Units', 'pixels', ...
'Position', [81, 4, 66, 30], ...
'HorizontalAlignment', 'left', ...
'String', 'Hanning', ...
'Style', 'radiobutton', ...
'Value', 0, ...
'Enable', 'off', ...
'Tag', 'H');

hMain.N.Radio(3) = uicontrol(...
'Parent', hMain.N.SubPanel(1), ...
'BackgroundColor', figcolor, ...
'Units', 'pixels', ...
'Position', [165, 4, 50, 30], ...
'HorizontalAlignment', 'left', ...
'String', 'Step', ...
'Style', 'radiobutton', ...
'Value', 0, ...
'Enable', 'off', ...
'Tag', 'S');

hMain.N.SubPanel(2) = uipanel(...
'Parent', hMain.Panel(2), ...
'BackgroundColor', figcolor, ...
'Units', 'pixels', ...
'ResizeFcn', @FigResize, ...
'Position', [280, 53, 260, 50], ...
'Title', 'Data Specs');

hMain.N.SubText(1) = uicontrol(...
'Parent', hMain.N.SubPanel(2), ...
'BackgroundColor', figcolor, ...
'Units', 'pixels', ...
'Position', [10, 8, 70, 20], ...
'HorizontalAlignment', 'left', ...
'String', 'Q max', ...
'Style', 'text');

hMain.N.Qmax = uicontrol(...
'Parent', hMain.N.SubPanel(2), ...
'BackgroundColor', figcolor, ...
'Units', 'pixels', ...
'Position', [50, 10, 60, 20], ...
'HorizontalAlignment', 'center', ...
'BackgroundColor', 'w', ...
'String', '50.0', ...
'Style', 'edit', ...
'Enable', 'off');

hMain.N.SubText(2) = uicontrol(...
'Parent', hMain.N.SubPanel(2), ...
'BackgroundColor', figcolor, ...
'Units', 'pixels', ...
'Position', [130, 8, 70, 20], ...
'HorizontalAlignment', 'left', ...
'String', 'Weighting', ...
'Style', 'text');

hMain.N.Weight = uicontrol(...
'Parent', hMain.N.SubPanel(2), ...
'BackgroundColor', figcolor, ...
'Units', 'pixels', ...
'Position', [185, 10, 60, 20], ...
'HorizontalAlignment', 'center', ...
'BackgroundColor', 'w', ...
'String', '0.0', ...
'Style', 'edit', ...
'Enable', 'off', ...

```

```

'Callback',@DTypeChange);

hMain.N.Text(2) = uicontrol(...
'Parent',hMain.Panel(2),...
'BackgroundColor',figcolor,...
'Units','Pixels',...
'Position',[40,25,200,20],...
'HorizontalAlignment','left',...
'Style','text',...
'String','Neutron scattering factor file');

hMain.N.FileName(2) = uicontrol(...
'Parent',hMain.Panel(2),...
'BackgroundColor',figcolor,...
'Units','pixels',...
'Position',[40,10,500,20],...
'HorizontalAlignment','left',...
'BackgroundColor','w',...
'Style','edit',...
'Enable','off');

hMain.N.Browse(2) = uicontrol(...
'Parent',hMain.Panel(2),...
'BackgroundColor',figcolor,...
'Units','pixels',...
'Position',[555,10,70,20],...
'HorizontalAlignment','left',...
'String','Browse',...
'Style','pushbutton',...
'Enable','off',...
'Callback',@Browse);

% This defines the third panel that deals with the fit specification

hMain.Panel(3) = uipanel(...
'Parent',hMain.fig,...
'BackgroundColor',figcolor,...
'Units','pixels',...
'ResizeFcn',@FigResize,...
'Position',[10,250,640,140],...
'Title','Fit Specification');

hMain.FS.Text(1) = uicontrol(...
'Parent',hMain.Panel(3),...
'BackgroundColor',figcolor,...
'Units','Pixels',...
'Position',[40,100,200,20],...
'HorizontalAlignment','left',...
'Style','text',...
'String','Initial parameter file');

hMain.FS.FileName(1) = uicontrol(...
'Parent',hMain.Panel(3),...
'BackgroundColor',figcolor,...
'Units','pixels',...
'Position',[40,85,500,20],...
'HorizontalAlignment','left',...
'BackgroundColor','w',...
'Style','edit',...
'Enable','off');

hMain.FS.Browse(1) = uicontrol(...
'Parent',hMain.Panel(3),...
'BackgroundColor',figcolor,...
'Units','pixels',...
'Position',[555,85,70,20],...
'HorizontalAlignment','left',...
'String','Browse',...
'Style','pushbutton',...
'Callback',@Browse,...
'Enable','off');

hMain.FS.Text(2) = uicontrol(...
'Parent',hMain.Panel(3),...
'BackgroundColor',figcolor,...
'Units','Pixels',...

```

```

'Position', [40, 55, 200, 20], ...
'HorizontalAlignment', 'left', ...
'Style', 'text', ...
'String', 'Fit constraints file');

hMain.FS.FileName(2) = uicontrol(...
'Parent', hMain.Panel(3), ...
'BackgroundColor', figcolor, ...
'Units', 'pixels', ...
'Position', [40, 40, 500, 20], ...
'HorizontalAlignment', 'left', ...
'BackgroundColor', 'w', ...
'Style', 'edit', ...
'Enable', 'off');

hMain.FS.Browse(2) = uicontrol(...
'Parent', hMain.Panel(3), ...
'BackgroundColor', figcolor, ...
'Units', 'pixels', ...
'Position', [555, 40, 70, 20], ...
'HorizontalAlignment', 'left', ...
'String', 'Browse', ...
'Style', 'pushbutton', ...
'Callback', @Browse, ...
'Enable', 'off');

hMain.FS.Text(3) = uicontrol(...
'Parent', hMain.Panel(3), ...
'BackgroundColor', figcolor, ...
'Units', 'pixels', ...
'Position', [40, 8, 70, 20], ...
'HorizontalAlignment', 'left', ...
'String', 'Q step', ...
'Style', 'text');

hMain.FS.Qstep = uicontrol(...
'Parent', hMain.Panel(3), ...
'BackgroundColor', figcolor, ...
'Units', 'pixels', ...
'Position', [80, 10, 60, 20], ...
'HorizontalAlignment', 'center', ...
'BackgroundColor', 'w', ...
'String', '0.02', ...
'Style', 'edit', ...
'Enable', 'off');

hMain.FS.Text(4) = uicontrol(...
'Parent', hMain.Panel(3), ...
'BackgroundColor', figcolor, ...
'Units', 'pixels', ...
'Position', [170, 8, 70, 20], ...
'HorizontalAlignment', 'left', ...
'String', 'R min', ...
'Style', 'text');

hMain.FS.Rmin = uicontrol(...
'Parent', hMain.Panel(3), ...
'BackgroundColor', figcolor, ...
'Units', 'pixels', ...
'Position', [210, 10, 60, 20], ...
'HorizontalAlignment', 'center', ...
'BackgroundColor', 'w', ...
'String', '1.5', ...
'Style', 'edit', ...
'Enable', 'off');

hMain.FS.Text(5) = uicontrol(...
'Parent', hMain.Panel(3), ...
'BackgroundColor', figcolor, ...
'Units', 'pixels', ...
'Position', [300, 8, 70, 20], ...
'HorizontalAlignment', 'left', ...
'String', 'R max', ...
'Style', 'text');

hMain.FS.Rmax = uicontrol(...

```



```

'Parent',hMain.Panel(3),...
'BackgroundColor',figcolor,...
'Units','pixels',...
'Position',[340,10,60,20],...
'HorizontalAlignment','center',...
'BackgroundColor','w',...
'String','3.0',...
'Style','edit',...
'Enable','off');

hMain.FS.Text(6) = uicontrol(...
'Parent',hMain.Panel(3),...
'BackgroundColor',figcolor,...
'Units','pixels',...
'Position',[420,8,70,20],...
'HorizontalAlignment','left',...
'String','Iterations',...
'Style','text');

hMain.FS.NumIter = uicontrol(...
'Parent',hMain.Panel(3),...
'BackgroundColor',figcolor,...
'Units','pixels',...
'Position',[470,10,60,20],...
'HorizontalAlignment','center',...
'BackgroundColor','w',...
'String','2000',...
'Style','edit',...
'Enable','off');

% This defines the fourth panel that drals with the output files

hMain.Panel(4) = uipanel(...
'Parent',hMain.fig,...
'BackgroundColor',figcolor,...
'Units','pixels',...
'ResizeFcn',@FigResize,...
'Position',[10,90,640,155],...
'Title','Output Files');

hMain.Out.Text(1) = uicontrol(...
'Parent',hMain.Panel(4),...
'BackgroundColor',figcolor,...
'Units','Pixels',...
'Position',[40,115,200,20],...
'HorizontalAlignment','left',...
'Style','text',...
'String','Optimised parameters file');

hMain.Out.FileName(1) = uicontrol(...
'Parent',hMain.Panel(4),...
'BackgroundColor',figcolor,...
'Units','pixels',...
'Position',[40,100,500,20],...
'HorizontalAlignment','left',...
'BackgroundColor','w',...
'Style','edit',...
'Enable','off');

hMain.Out.Browse(1) = uicontrol(...
'Parent',hMain.Panel(4),...
'BackgroundColor',figcolor,...
'Units','pixels',...
'Position',[555,100,70,20],...
'HorizontalAlignment','left',...
'String','Browse',...
'Style','pushbutton',...
'Enable','off',...
'Callback',@Browse);

hMain.Out.Text(2) = uicontrol(...
'Parent',hMain.Panel(4),...
'BackgroundColor',figcolor,...
'Units','Pixels',...

```

```

'Position', [40, 70, 200, 20], ...
'HorizontalAlignment', 'left', ...
'Style', 'text', ...
'String', 'X-ray fit file');

hMain.Out.FileName(2) = uicontrol(...
'Parent', hMain.Panel(4), ...
'BackgroundColor', figcolor, ...
'Units', 'pixels', ...
'Position', [40, 55, 500, 20], ...
'HorizontalAlignment', 'left', ...
'BackgroundColor', 'w', ...
'Style', 'edit', ...
'Enable', 'off');

hMain.Out.Browse(2) = uicontrol(...
'Parent', hMain.Panel(4), ...
'BackgroundColor', figcolor, ...
'Units', 'pixels', ...
'Position', [555, 55, 70, 20], ...
'HorizontalAlignment', 'left', ...
'String', 'Browse', ...
'Style', 'pushbutton', ...
'Enable', 'off', ...
'Callback', @Browse);

hMain.Out.Text(3) = uicontrol(...
'Parent', hMain.Panel(4), ...
'BackgroundColor', figcolor, ...
'Units', 'Pixels', ...
'Position', [40, 25, 200, 20], ...
'HorizontalAlignment', 'left', ...
'Style', 'text', ...
'String', 'Neutron fit file');

hMain.Out.FileName(3) = uicontrol(...
'Parent', hMain.Panel(4), ...
'BackgroundColor', figcolor, ...
'Units', 'pixels', ...
'Position', [40, 10, 500, 20], ...
'HorizontalAlignment', 'left', ...
'BackgroundColor', 'w', ...
'Style', 'edit', ...
'Enable', 'off');

hMain.Out.Browse(3) = uicontrol(...
'Parent', hMain.Panel(4), ...
'BackgroundColor', figcolor, ...
'Units', 'pixels', ...
'Position', [555, 10, 70, 20], ...
'HorizontalAlignment', 'left', ...
'String', 'Browse', ...
'Style', 'pushbutton', ...
'Enable', 'off', ...
'Callback', @Browse);

% Push buttons to start and stop the fitting process

hMain.Start = uicontrol(...
'Parent', hMain.fig, ...
'Units', 'pixels', ...
'Position', [100, 30, 140, 45], ...
'String', 'Start', ...
'FontWeight', 'bold', ...
'FontSize', 12, ...
'BackgroundColor', 'g', ...
'Style', 'pushbutton', ...
'Tag', ' ', ...
'Callback', @Initiate);

hMain.Stop = uicontrol(...
'Parent', hMain.fig, ...
'Units', 'pixels', ...
'Position', [260, 30, 140, 45], ...
'String', 'Stop', ...
'FontWeight', 'bold', ...

```

```

'FontSize',12,...
'BackgroundColor','r',...
'Style','pushbutton',...
'Tag','go',...
'Callback',@Stopper);

hMain.Show = uicontrol(...
'Parent',hMain.fig,...
'Units','pixels',...
'Position',[420,30,140,45],...
'String','Show Partial',...
'FontWeight','bold',...
'FontSize',12,...
'BackgroundColor',figcolor,...
'Style','pushbutton',...
'Enable','off',...
'Callback',@ShowCor);

% Graphs to display the data

hMain.Panel(5) = uipanel(...
'Parent',hMain.fig,...
'BackgroundColor',figcolor,...
'Units','pixels',...
'Position',[660,395,630,345],...
'Title','X-ray fit');

hMain.X.Graph = axes(...
'Parent',hMain.Panel(5),...
'Units','normalized',...
'Position',[0.05,0.08,0.92,0.90]);

hMain.Panel(6) = uipanel(...
'Parent',hMain.fig,...
'BackgroundColor',figcolor,...
'Units','pixels',...
'Position',[660,45,630,345],...
'Title','Neutron fit');

hMain.N.Graph = axes(...
'Parent',hMain.Panel(6),...
'Units','normalized',...
'Position',[0.05,0.08,0.92,0.90]);

% All GUI controls are implemented in code form. Although this method is
% time consuming and code hungry it does provide the most efficient way to
% move the code around and debug.

% -----

% The ratio of each object's dimensions relative to it's parent's
% dimensions are determined here to ensure that the objects maintain their
% relative sizes and positions upon figure resize execution.
hList=findall(hMain.fig); Ratio=[hList zeros(length(hList),4)];
for k=2:1:length(hList)
    ChdPos=get(hList(k),'Position');
    ParPos=get(get(hList(k),'Parent'),'Position');

Ratio(k,2:end)=[ChdPos(1)./ParPos(3),ChdPos(2)./ParPos(4),ChdPos(3)./ParPos(3),ChdPos(4)
)./ParPos(4)];
end

% Callbacks -----
function DTypeChange(hSource,eventdata)
% This function is somewhat bulky and there is probably a better
% way to write it. The only purpose here is to change the state of
% some uicontrols from active to inactive and vice versa.
XState=get(hMain.X.Tick,'Value');
NState=get(hMain.N.Tick,'Value');
XWeight=str2double(get(hMain.X.Weight,'String'));
NWeight=str2double(get(hMain.N.Weight,'String'));

if XState==1 && NState==1
    set(hMain.Start,'Tag','XN');
    set(hMain.X.FileName(1),'Enable','on');

```

```

set(hMain.X.Browse(1), 'Enable', 'on');
set(hMain.X.FileName(2), 'Enable', 'on');
set(hMain.X.Browse(2), 'Enable', 'on');
set(hMain.X.Radio(1), 'Enable', 'on');
set(hMain.X.Radio(2), 'Enable', 'on');
set(hMain.X.Radio(3), 'Enable', 'on');
set(hMain.X.Qmax, 'Enable', 'on');
set(hMain.X.Weight, 'Enable', 'on');

set(hMain.N.FileName(1), 'Enable', 'on');
set(hMain.N.Browse(1), 'Enable', 'on');
set(hMain.N.FileName(2), 'Enable', 'on');
set(hMain.N.Browse(2), 'Enable', 'on');
set(hMain.N.Radio(1), 'Enable', 'on');
set(hMain.N.Radio(2), 'Enable', 'on');
set(hMain.N.Radio(3), 'Enable', 'on');
set(hMain.N.Qmax, 'Enable', 'on');
set(hMain.N.Weight, 'Enable', 'on');

set(hMain.FS.FileName(1), 'Enable', 'on');
set(hMain.FS.Browse(1), 'Enable', 'on');
set(hMain.FS.FileName(2), 'Enable', 'on');
set(hMain.FS.Browse(2), 'Enable', 'on');
set(hMain.FS.Qstep, 'Enable', 'on');
set(hMain.FS.Rmin, 'Enable', 'on');
set(hMain.FS.Rmax, 'Enable', 'on');
set(hMain.FS.NumIter, 'Enable', 'on');

set(hMain.Out.FileName(1), 'Enable', 'on');
set(hMain.Out.FileName(2), 'Enable', 'on');
set(hMain.Out.FileName(3), 'Enable', 'on');
set(hMain.Out.Browse(1), 'Enable', 'on');
set(hMain.Out.Browse(2), 'Enable', 'on');
set(hMain.Out.Browse(3), 'Enable', 'on');

if hSource == hMain.X.Weight
    set(hMain.N.Weight, 'String', num2str(1.0-XWeight));
elseif hSource == hMain.N.Weight
    set(hMain.X.Weight, 'String', num2str(1.0-NWeight));
end

elseif XState==1 && NState==0
set(hMain.Start, 'Tag', 'X');
set(hMain.X.FileName(1), 'Enable', 'on');
set(hMain.X.Browse(1), 'Enable', 'on');
set(hMain.X.FileName(2), 'Enable', 'on');
set(hMain.X.Browse(2), 'Enable', 'on');
set(hMain.X.Radio(1), 'Enable', 'on');
set(hMain.X.Radio(2), 'Enable', 'on');
set(hMain.X.Radio(3), 'Enable', 'on');
set(hMain.X.Qmax, 'Enable', 'on');
set(hMain.X.Weight, 'Enable', 'off', 'String', '1.0');

set(hMain.N.FileName(1), 'Enable', 'off');
set(hMain.N.Browse(1), 'Enable', 'off');
set(hMain.N.FileName(2), 'Enable', 'off');
set(hMain.N.Browse(2), 'Enable', 'off');
set(hMain.N.Radio(1), 'Enable', 'off');
set(hMain.N.Radio(2), 'Enable', 'off');
set(hMain.N.Radio(3), 'Enable', 'off');
set(hMain.N.Qmax, 'Enable', 'off');
set(hMain.N.Weight, 'Enable', 'off', 'String', '0.0');

set(hMain.FS.FileName(1), 'Enable', 'on');
set(hMain.FS.Browse(1), 'Enable', 'on');
set(hMain.FS.FileName(2), 'Enable', 'on');
set(hMain.FS.Browse(2), 'Enable', 'on');
set(hMain.FS.Qstep, 'Enable', 'on');
set(hMain.FS.Rmin, 'Enable', 'on');
set(hMain.FS.Rmax, 'Enable', 'on');
set(hMain.FS.NumIter, 'Enable', 'on');

set(hMain.Out.FileName(1), 'Enable', 'on');
set(hMain.Out.FileName(2), 'Enable', 'on');
set(hMain.Out.FileName(3), 'Enable', 'off');
set(hMain.Out.Browse(1), 'Enable', 'on');

```

```

set(hMain.Out.Browse(2), 'Enable', 'on');
set(hMain.Out.Browse(3), 'Enable', 'off');

elseif XState==0 && NState==1
set(hMain.Start, 'Tag', 'N');
set(hMain.X.FileName(1), 'Enable', 'off');
set(hMain.X.Browse(1), 'Enable', 'off');
set(hMain.X.FileName(2), 'Enable', 'off');
set(hMain.X.Browse(2), 'Enable', 'off');
set(hMain.X.Radio(1), 'Enable', 'off');
set(hMain.X.Radio(2), 'Enable', 'off');
set(hMain.X.Radio(3), 'Enable', 'off');
set(hMain.X.Qmax, 'Enable', 'off');
set(hMain.X.Weight, 'Enable', 'off', 'String', '0.0');

set(hMain.N.FileName(1), 'Enable', 'on');
set(hMain.N.Browse(1), 'Enable', 'on');
set(hMain.N.FileName(2), 'Enable', 'on');
set(hMain.N.Browse(2), 'Enable', 'on');
set(hMain.N.Radio(1), 'Enable', 'on');
set(hMain.N.Radio(2), 'Enable', 'on');
set(hMain.N.Radio(3), 'Enable', 'on');
set(hMain.N.Qmax, 'Enable', 'on');
set(hMain.N.Weight, 'Enable', 'off', 'String', '1.0');

set(hMain.FS.FileName(1), 'Enable', 'on');
set(hMain.FS.Browse(1), 'Enable', 'on');
set(hMain.FS.FileName(2), 'Enable', 'on');
set(hMain.FS.Browse(2), 'Enable', 'on');
set(hMain.FS.Qstep, 'Enable', 'on');
set(hMain.FS.Rmin, 'Enable', 'on');
set(hMain.FS.Rmax, 'Enable', 'on');
set(hMain.FS.NumIter, 'Enable', 'on');

set(hMain.Out.FileName(1), 'Enable', 'on');
set(hMain.Out.FileName(2), 'Enable', 'off');
set(hMain.Out.FileName(3), 'Enable', 'on');
set(hMain.Out.Browse(1), 'Enable', 'on');
set(hMain.Out.Browse(2), 'Enable', 'off');
set(hMain.Out.Browse(3), 'Enable', 'on');

elseif XState==0 && NState==0
set(hMain.Start, 'Tag', ' ');
set(hMain.X.FileName(1), 'Enable', 'off');
set(hMain.X.Browse(1), 'Enable', 'off');
set(hMain.X.FileName(2), 'Enable', 'off');
set(hMain.X.Browse(2), 'Enable', 'off');
set(hMain.X.Radio(1), 'Enable', 'off');
set(hMain.X.Radio(2), 'Enable', 'off');
set(hMain.X.Radio(3), 'Enable', 'off');
set(hMain.X.Qmax, 'Enable', 'off');
set(hMain.X.Weight, 'Enable', 'off', 'String', '0.0');

set(hMain.N.FileName(1), 'Enable', 'off');
set(hMain.N.Browse(1), 'Enable', 'off');
set(hMain.N.FileName(2), 'Enable', 'off');
set(hMain.N.Browse(2), 'Enable', 'off');
set(hMain.N.Radio(1), 'Enable', 'off');
set(hMain.N.Radio(2), 'Enable', 'off');
set(hMain.N.Radio(3), 'Enable', 'off');
set(hMain.N.Qmax, 'Enable', 'off');
set(hMain.N.Weight, 'Enable', 'off', 'String', '0.0');

set(hMain.FS.FileName(1), 'Enable', 'off');
set(hMain.FS.Browse(1), 'Enable', 'off');
set(hMain.FS.FileName(2), 'Enable', 'off');
set(hMain.FS.Browse(2), 'Enable', 'off');
set(hMain.FS.Qstep, 'Enable', 'off');
set(hMain.FS.Rmin, 'Enable', 'off');
set(hMain.FS.Rmax, 'Enable', 'off');
set(hMain.FS.NumIter, 'Enable', 'off');

set(hMain.Out.FileName(1), 'Enable', 'off');
set(hMain.Out.FileName(2), 'Enable', 'off');
set(hMain.Out.FileName(3), 'Enable', 'off');
set(hMain.Out.Browse(1), 'Enable', 'off');

```

```

        set(hMain.Out.Browse(2), 'Enable', 'off');
        set(hMain.Out.Browse(3), 'Enable', 'off');

    end
end

function Browse(hSource,eventdata)
% The Browse function allows for the selection of files to be read
% into the program
set(hMain.Show, 'Enable', 'off');
[filename DataPath] = uigetfile('*.*', 'File Selector', DataPath);
if isequal(filename,0)
    DataPath=MainRoot(1:3);
    return
end
if hSource == hMain.X.Browse(1)
    set(hMain.X.FileName(1), 'String', [DataPath filename]);
    set(hMain.Out.FileName(1), 'String', DataPath);
    set(hMain.Out.FileName(2), 'String', DataPath);
    Data=dlmread([DataPath filename]); plot(hMain.X.Graph,Data(:,1),Data(:,2));
elseif hSource == hMain.N.Browse(1)
    set(hMain.N.FileName(1), 'String', [DataPath filename]);
    set(hMain.Out.FileName(1), 'String', DataPath);
    set(hMain.Out.FileName(3), 'String', DataPath);
    Data=dlmread([DataPath filename]); plot(hMain.N.Graph,Data(:,1),Data(:,2));
elseif hSource == hMain.X.Browse(2)
    set(hMain.X.FileName(2), 'String', [DataPath filename]);
elseif hSource == hMain.N.Browse(2)
    set(hMain.N.FileName(2), 'String', [DataPath filename]);
elseif hSource == hMain.FS.Browse(1)
    set(hMain.FS.FileName(1), 'String', [DataPath filename]);
elseif hSource == hMain.FS.Browse(2)
    set(hMain.FS.FileName(2), 'String', [DataPath filename]);
elseif hSource == hMain.Out.Browse(1)
    set(hMain.Out.FileName(1), 'String', [DataPath filename]);
elseif hSource == hMain.Out.Browse(2)
    set(hMain.Out.FileName(2), 'String', [DataPath filename]);
elseif hSource == hMain.Out.Browse(3)
    set(hMain.Out.FileName(3), 'String', [DataPath filename]);
end
end

function MtypeChange(hSource,eventdata)
Mtype=get(eventdata.NewValue, 'Tag');
set(hSource, 'Tag', Mtype);
end

function Initiate(hSource,eventdata)
set(hMain.Show, 'Enable', 'off');
set(hMain.Stop, 'Tag', 'go');
Dtype = get(hMain.Start, 'Tag');
Qstep = str2double(get(hMain.FS.Qstep, 'String'));
inpar=dlmread(get(hMain.FS.FileName(1), 'String'));
bounds=dlmread(get(hMain.FS.FileName(2), 'String'));
XWeight=str2double(get(hMain.X.Weight, 'String'));
NWeight=str2double(get(hMain.N.Weight, 'String'));
NumIter=str2double(get(hMain.FS.NumIter, 'String'));

StartPoint=inpar(:,1:3);
UB = StartPoint+bounds;
LB = StartPoint-bounds;

ai = inpar(:,4);
aj = inpar(:,5);

%-----
if strcmp(Dtype, 'X')==1
    XData=dlmread(get(hMain.X.FileName(1), 'String'));
    Xsf=dlmread(get(hMain.X.FileName(2), 'String'));
    XMtype=get(hMain.X.SubPanel(1), 'Tag');
    XQmax=str2double(get(hMain.X.Qmax, 'String'));

    Xr=XData(:,1); XTr=XData(:,2); XQ=(0.02:Qstep:XQmax)';

    f=zeros(length(XQ), length(Xsf(1, :)));
    for j = 1:length(Xsf(1, :))

```

```

        a1 = Xsf(3, j);
        a2 = Xsf(4, j);
        a3 = Xsf(5, j);
        a4 = Xsf(6, j);
        b1 = Xsf(7, j);
        b2 = Xsf(8, j);
        b3 = Xsf(9, j);
        b4 = Xsf(10, j);
        c = Xsf(11, j);
        f(:, j) = (a1.*exp(-b1.*(XQ./(4*pi)).^2))+(a2.*exp(-
b2.*(XQ./(4*pi)).^2))+(a3.*exp(-b3.*(XQ./(4*pi)).^2))+(a4.*exp(-
b4.*(XQ./(4*pi)).^2))+c;
    end
    comp = Xsf(2, :)/sum(Xsf(2, :));
    fbar = f*comp';

    ci=zeros(length(inpar(:,1)),1); cj=zeros(length(inpar(:,1)),1);
    fi=zeros(length(f(:,1)),length(inpar(:,1)));
    fj=zeros(length(f(:,1)),length(inpar(:,1)));
    Xw=zeros(length(f(:,1)),length(inpar(:,1)));
    for j = 1:length(inpar(:,1))
        ci(j) = comp(ai(j));
        cj(j) = comp(aj(j));
        fi(:, j) = f(:, ai(j));
        fj(:, j) = f(:, aj(j));
        if ai(j) == aj(j)
            Xw(:, j) = ci(j).*cj(j).*fi(:, j).*fj(:, j)./(fbar.^2);
        else
            Xw(:, j) = 2.*ci(j).*cj(j).*fi(:, j).*fj(:, j)./(fbar.^2);
        end
    end
end

%-----
elseif strcmp(Dtype, 'N')==1
    NData=dlmread(get(hMain.N.FileName(1), 'String'));
    Nsf=dlmread(get(hMain.N.FileName(2), 'String'));
    NMtype=get(hMain.N.SubPanel(1), 'Tag');
    NQmax=str2double(get(hMain.N.Qmax, 'String'));

    Nr=NData(:,1); NTr=NData(:,2); NQ=(0.02:Qstep:NQmax)';

    ci=zeros(length(inpar(:,1)),1); cj=zeros(length(inpar(:,1)),1);
    bi=zeros(length(inpar(:,1)),1); bj=zeros(length(inpar(:,1)),1);
    Nw=zeros(1,length(inpar(:,1)));
    for j = 1:length(inpar(:,1))
        ci(j) = Nsf(ai(j),3)/sum(Nsf(:,3));
        cj(j) = Nsf(aj(j),3)/sum(Nsf(:,3));
        bi(j) = Nsf(ai(j),2);
        bj(j) = Nsf(aj(j),2);
        if ai(j) == aj(j)
            Nw(j) = ci(j)*cj(j)*bi(j)*bj(j);
        else
            Nw(j) = 2*ci(j)*cj(j)*bi(j)*bj(j);
        end
    end
end

%-----
elseif strcmp(Dtype, 'XN')==1
    XData=dlmread(get(hMain.X.FileName(1), 'String'));
    Xsf=dlmread(get(hMain.X.FileName(2), 'String'));
    XMtype=get(hMain.X.SubPanel(1), 'Tag');
    XQmax=str2double(get(hMain.X.Qmax, 'String'));

    Xr=XData(:,1); XTr=XData(:,2); XQ=(0.02:Qstep:XQmax)';

    f=zeros(length(XQ),length(Xsf(1,:)));
    for j = 1:length(Xsf(1,:))
        a1 = Xsf(3, j);
        a2 = Xsf(4, j);
        a3 = Xsf(5, j);
        a4 = Xsf(6, j);
        b1 = Xsf(7, j);
        b2 = Xsf(8, j);
        b3 = Xsf(9, j);
        b4 = Xsf(10, j);
        c = Xsf(11, j);

```

```

        f(:,j) = (a1.*exp(-b1.*(XQ./(4*pi)).^2))+(a2.*exp(-
b2.*(XQ./(4*pi)).^2))+a3.*exp(-b3.*(XQ./(4*pi)).^2))+a4.*exp(-
b4.*(XQ./(4*pi)).^2)+c;
    end
    comp = Xsf(2,:)./sum(Xsf(2,:));
    fbar = f*comp';

    ci=zeros(length(inpar(:,1)),1); cj=zeros(length(inpar(:,1)),1);
    fi=zeros(length(f(:,1)),length(inpar(:,1)));
    fj=zeros(length(f(:,1)),length(inpar(:,1)));
    Xw=zeros(length(f(:,1)),length(inpar(:,1)));
    for j = 1:length(inpar(:,1))
        ci(j) = comp(ai(j));
        cj(j) = comp(aj(j));
        fi(:,j) = f(:,ai(j));
        fj(:,j) = f(:,aj(j));
        if ai(j) == aj(j)
            Xw(:,j) = ci(j).*cj(j).*fi(:,j).*fj(:,j)./(fbar.^2);
        else
            Xw(:,j) = 2.*ci(j).*cj(j).*fi(:,j).*fj(:,j)./(fbar.^2);
        end
    end

    NData=dlmread(get(hMain.N.FileName(1),'String'));
    Nsf=dlmread(get(hMain.N.FileName(2),'String'));
    NMtype=get(hMain.N.SubPanel(1),'Tag');
    NQmax=str2double(get(hMain.N.Qmax,'String'));

    Nr=NData(:,1); NTr=NData(:,2); NQ=(0.02:Qstep:NQmax)';

    ci=zeros(length(inpar(:,1)),1); cj=zeros(length(inpar(:,1)),1);
    bi=zeros(length(inpar(:,1)),1); bj=zeros(length(inpar(:,1)),1);
    Nw=zeros(1,length(inpar(:,1)));
    for j = 1:length(inpar(:,1))
        ci(j) = Nsf(ai(j),3)/sum(Nsf(:,3));
        cj(j) = Nsf(aj(j),3)/sum(Nsf(:,3));
        bi(j) = Nsf(ai(j),2);
        bj(j) = Nsf(aj(j),2);
        if ai(j) == aj(j)
            Nw(j) = ci(j)*cj(j)*bi(j)*bj(j);
        else
            Nw(j) = 2*ci(j)*cj(j)*bi(j)*bj(j);
        end
    end

    %-----
    options =
optimset('Display','iter','MaxIter',NumIter,'TolFun',0.1,'TolX',0.1,'OutputFcn',@Status
Checker);
    FitParams = fminsearchcon(@PairFunc, StartPoint, LB, UB, [], [], [], options);
    dlmwrite(get(hMain.Out.FileName(1),'String'),[FitParams ai
aj], 'delimiter', '\t', 'precision', 8);

    R = FitParams(:,1);
    N = FitParams(:,2);
    sig = FitParams(:,3);

    NUM_OF_CURVES = size(FitParams,1);

    if strcmp(Dtype, 'X')==1
        XCurveQ=zeros(length(XQ), NUM_OF_CURVES);
        XCurveR=zeros(length(Xr), NUM_OF_CURVES);

        for j = 1:NUM_OF_CURVES
            XCurveQ(:,j) =
(N(j).*Xw(:,j)./cj(j)).*(sin(XQ.*R(j))./(XQ.*R(j))).*exp(-XQ.^2.*sig(j).^2./2);
            XCurveR(:,j) = FTrans(XQ, XCurveQ(:,j), Xr, XMtype, 'X');
        end

        XFitted_Tr = sum(XCurveR,2);
        dlmwrite(get(hMain.Out.FileName(2),'String'),[Xr XTr XFitted_Tr
XCurveR], 'delimiter', '\t', 'precision', 8);
        dlmwrite([get(hMain.Out.FileName(2),'String') '.q'], [XQ
XCurveQ], 'delimiter', '\t', 'precision', 8);

```



```

%-----
elseif strcmp(Dtype, 'N')==1
    NCurveQ=zeros(length(NQ), NUM_OF_CURVES);
    NCurveR=zeros(length(Nr), NUM_OF_CURVES);

    for j = 1:1:NUM_OF_CURVES
        NCurveQ(:, j) =
(N(j).*Nw(:, j)./cj(j)).*(sin(NQ.*R(j))./(NQ.*R(j))).*exp(-NQ.^2.*sig(j).^2./2);
        NCurveR(:, j) = FTrans(NQ, NCurveQ(:, j)./100, Nr, NMtype, 'N');
    end

    NFitted_Tr = sum(NCurveR, 2);
    dlmwrite(get(hMain.Out.FileName(3), 'String'), [Nr NTr NFitted_Tr
NCurveR], 'delimiter', '\t', 'precision', 8);

%-----
elseif strcmp(Dtype, 'XN')==1
    NCurveQ=zeros(length(NQ), NUM_OF_CURVES);
    XCurveQ=zeros(length(XQ), NUM_OF_CURVES);
    NCurveR=zeros(length(Nr), NUM_OF_CURVES);
    XCurveR=zeros(length(Xr), NUM_OF_CURVES);

    for j = 1:1:NUM_OF_CURVES
        XCurveQ(:, j) =
(N(j).*Xw(:, j)./cj(j)).*(sin(XQ.*R(j))./(XQ.*R(j))).*exp(-XQ.^2.*sig(j).^2./2);
        XCurveR(:, j) = FTrans(XQ, XCurveQ(:, j), Xr, XMtype, 'X');
        NCurveQ(:, j) =
(N(j).*Nw(:, j)./cj(j)).*(sin(NQ.*R(j))./(NQ.*R(j))).*exp(-NQ.^2.*sig(j).^2./2);
        NCurveR(:, j) = FTrans(NQ, NCurveQ(:, j)./100, Nr, NMtype, 'N');
    end

    XFitted_Tr = sum(XCurveR, 2);
    dlmwrite(get(hMain.Out.FileName(2), 'String'), [Xr XTr XFitted_Tr
XCurveR], 'delimiter', '\t', 'precision', 8);
    NFitted_Tr = sum(NCurveR, 2);
    dlmwrite(get(hMain.Out.FileName(3), 'String'), [Nr NTr NFitted_Tr
NCurveR], 'delimiter', '\t', 'precision', 8);

end
set(hMain.Show, 'Enable', 'on');

% Nested functions to take care of the optimisations and Fourier transform
function sse = PairFunc(params)
    Rmin = str2double(get(hMain.FS.Rmin, 'String'));
    Rmax = str2double(get(hMain.FS.Rmax, 'String'));

    NUM_OF_CURVES = size(params, 1);
    R = params(:, 1);
    N = params(:, 2);
    sig = params(:, 3);

    XFittedCurve = 0; NFittedCurve = 0;
    if strcmp(Dtype, 'X')==1
        for i = 1:1:NUM_OF_CURVES
            XFittedCurve = XFittedCurve +
(N(i).*Xw(:, i)./cj(i)).*(sin(XQ.*R(i))./(XQ.*R(i))).*exp(-XQ.^2.*sig(i).^2./2);
        end
        XFitted_Tr = FTrans(XQ, XFittedCurve, Xr, XMtype, 'X');
        XErrorVector = XFitted_Tr(Rmin<=Xr & Xr<=Rmax) - XTr(Rmin<=Xr &
Xr<=Rmax);
        plot(hMain.X.Graph, Xr, XFitted_Tr, 'r', Xr, XTr, 'b');

    elseif strcmp(Dtype, 'N')==1
        for i = 1:1:NUM_OF_CURVES
            NFittedCurve = NFittedCurve +
(N(i).*Nw(:, i)./cj(i)).*(sin(NQ.*R(i))./(NQ.*R(i))).*exp(-NQ.^2.*sig(i).^2./2);
        end
        NFitted_Tr = FTrans(NQ, NFittedCurve./100, Nr, NMtype, 'N');
        NErrorVector = NFitted_Tr(Rmin<=Nr & Nr<=Rmax) - NTr(Rmin<=Nr &
Nr<=Rmax);
        plot(hMain.N.Graph, Nr, NFitted_Tr, 'r', Nr, NTr, 'b');

    elseif strcmp(Dtype, 'XN')==1
        for i = 1:1:NUM_OF_CURVES
            XFittedCurve = XFittedCurve +
(N(i).*Xw(:, i)./cj(i)).*(sin(XQ.*R(i))./(XQ.*R(i))).*exp(-XQ.^2.*sig(i).^2./2);

```

```

        NFittedCurve = NFittedCurve +
(N(i).*Nw(:,i)./cj(i)).*(sin(NQ.*R(i))./(NQ.*R(i))).*exp(-NQ.^2.*sig(i).^2./2);
    end
    XFitted_Tr = FTrans(XQ,XFittedCurve,Xr,XMtype,'X');
    XErrorVector = XFitted_Tr(Rmin<=Xr & Xr<=Rmax) - XTr(Rmin<=Xr &
Xr<=Rmax);
    plot(hMain.X.Graph,Xr,XFitted_Tr,'r',Xr,XTr,'b');
    NFitted_Tr = FTrans(NQ,NFittedCurve./100,Nr,NMtype,'N');
    NErrorVector = NFitted_Tr(Rmin<=Nr & Nr<=Rmax) - NTr(Rmin<=Nr &
Nr<=Rmax);
    plot(hMain.N.Graph,Nr,NFitted_Tr,'r',Nr,NTr,'b');
    end
    if NWeight==0
        TotalErrorVectorSquared = XErrorVector.^2;
    elseif XWeight==0
        TotalErrorVectorSquared = NErrorVector.^2;
    else
        TotalErrorVectorSquared = XWeight.*(XErrorVector.^2)./mean(XTr(Rmin<=Xr
& Xr<=Rmax).^2) + NWeight.*(NErrorVector.^2)./mean(NTr(Rmin<=Nr & Nr<=Rmax).^2);
    end
    sse = sum(TotalErrorVectorSquared);
    drawnow
end

function Tr = FTrans(Q,iQ,r,Mtype,Ttype)

    if strcmp(Mtype,'L')==1
        M = max(Q)./pi./Q.*sin(pi.*Q./max(Q));
    elseif strcmp(Mtype,'H')==1
        M = (1+cos(pi.*Q./max(Q)))./2;
    else
        M = 1;
    end

    f=zeros(length(Q),length(r));
    for i=1:length(r)
        f(:,i) = M.*Q.*iQ.*sin(Q.*r(i));
    end

    if strcmp(Ttype,'N')==1
        Tr = 2.*trapz(Q,f,1)'./pi;
    elseif strcmp(Ttype,'X')==1
        Tr = trapz(Q,f,1)';
    end
end

function stop=StatusChecker(x,optimvalues,state)
    stop=strcmp(get(hMain.Stop,'Tag'),'stop');
end

function Stopper(hSource,eventdata)
    set(hSource,'Tag','stop');
end

function FigResize(hSource,eventdata)
    Pos=get(hSource,'Position');
    hRel=allchild(hSource);
    for i=1:length(hRel)
        [I,J]=ind2sub(size(Ratio),find(Ratio==hRel(i)));
set(hRel(i),'Position',[Pos(3)*Ratio(I,2),Pos(4)*Ratio(I,3),Pos(3)*Ratio(I,4),Pos(4)*Ra
tio(I,5)]);
    end
end

function ShowCor(hSource,eventdata)
    hMain.Corfig = figure(...
        'Name','NXFit - Partial Pair Correlations',...
        'NumberTitle','off', ...
        'Menubar','none',...
        'ToolBar','none',...
        'Resize','on',...
        'Position',[150,90,900,650]);

```

```

        if strcmp(Dtype,'X')==1
            hMain.Axes =
axes('Parent',hMain.Corfig,'Position',[0.05,0.05,0.90,0.90],'Units','normalized');
plot(hMain.Axes,Xr,XTr,Xr,XFitted_Tr,'r',Xr,XCurveR,'g',Xr,XTr-
XFitted_Tr,'--k');
grid(hMain.Axes,'on'); title(hMain.Axes,'X-ray Pair Correlations');
        elseif strcmp(Dtype,'N')==1
            hMain.Axes =
axes('Parent',hMain.Corfig,'Position',[0.05,0.05,0.90,0.90],'Units','normalized');
plot(hMain.Axes,Nr,NTr,Nr,NFitted_Tr,'r',Nr,NCurveR,'g',Nr,NTr-
NFitted_Tr,'--k');
grid(hMain.Axes,'on'); title(hMain.Axes,'Neutron Pair Correlations');
        elseif strcmp(Dtype,'XN')==1
            hMain.SubAxes(1) = subplot('Position',[0.05,0.05,0.90,0.40]);
            hMain.SubAxes(2) = subplot('Position',[0.05,0.55,0.90,0.40]);
            plot(hMain.SubAxes(2),Xr,XTr,Xr,XFitted_Tr,'r',Xr,XCurveR,'g',Xr,XTr-
XFitted_Tr,'--k');
            grid(hMain.SubAxes(2),'on'); title(hMain.SubAxes(2),'X-ray Pair
Correlations');
            plot(hMain.SubAxes(1),Nr,NTr,Nr,NFitted_Tr,'r',Nr,NCurveR,'g',Nr,NTr-
NFitted_Tr,'--k');
            grid(hMain.SubAxes(1),'on'); title(hMain.SubAxes(1),'Neutron Pair
Correlations');
        end
    end
end

function CloseRequest(hSource,eventdata)
    selection = questdlg(...
        'Are you sure you want to quit NXFit?',...
        'NXFit',...
        'Yes','No','Yes');
    switch selection,
        case 'Yes',
            delete(gcf)
        case 'No'
            return
    end
end

% End statement for entire program
end

```